Distribution Agreement

In presenting this thesis or dissertation as a partial fulfillment of the requirements for an advanced degree from Emory University, I hereby grant to Emory University and its agents the non-exclusive license to archive, make accessible, and display my thesis or dissertation in whole or in part in all forms of media, now or hereafter known, including display on the world wide web. I understand that I may select some access restrictions as part of the online submission of this thesis or dissertation. I retain all ownership rights to the copyright of the thesis or dissertation. I also retain the right to use in future works (such as articles or books) all or part of this thesis or dissertation.

Signature:

_____ _____

Wentao Yu Date

Inferring force laws from many-body systems in dusty plasma by machine learning

By

Wentao Yu
Doctor of Philosophy

Physics

Justin C. Burton, Ph.D.
Advisor

Stefan Boettcher, Ph.D.
Committee Member

Ilya M. Nemenman, Ph.D.
Committee Member

Edward Jr. Thomas, Ph.D.
Committee Member

Eric R. Weeks, Ph.D.
Committee Member

Accepted:

Kimberly Jacob Arriola, Ph.D.
Dean of the James T. Laney School of Graduate Studies

Date

Inferring force laws from many-body systems in dusty plasma by machine learning

By

Wentao Yu
B.A., Zhejiang University, China, 2018

Advisor: Justin C. Burton, Ph.D.

An abstract of
A dissertation submitted to the Faculty of the
James T. Laney School of Graduate Studies of Emory University
in partial fulfillment of the requirements for the degree of
Doctor of Philosophy
in Physics
2024

Abstract

Inferring force laws from many-body systems in dusty plasma by machine learning
By Wentao Yu

In the era of big data, machine learning (ML) is a necessity. Numerous ML studies have been conducted to analyze data within physical systems. Most of these studies utilize data simulated by known, well-defined equations. Others attempt to predict the future states of real experiments, rather than unraveling the governing mechanisms (the physics) behind them. Predicting the governing mechanisms in real experiments poses significant challenges. During my Ph.D., I have applied ML methods to a complex many-body system, dusty plasma (DP), which is prevalent both in the cosmos and in industrial applications, and I validated these models' predictions using only experimental data. DP exhibits many intriguing collective behaviors, although the underlying mechanisms, including charging theories, are often modeled using theories with assumptions that are difficult to test, resulting in large errors. Throughout my six years of Ph.D. research, I initially constructed a tomography system to track the 3D trajectories of individual particles, achieving sub-pixel accuracy for tens of particles over several minutes. Subsequently, I analyzed the tracked 'Brownian' motion of one and two particles around their equilibrium positions and proposed a linearized model for these small-amplitude motions. Applying ML, I predicted the linear coefficients with 50% better accuracy than conventional methods, including Fourier analysis. This prediction was corroborated by physically perturbing the particles from their equilibrium positions. Finally, using the tracked 3D trajectories of multiple particles, I employed ML to infer their position-dependent interaction forces, environmental forces, and damping coefficients. Non-reciprocal interactions were observable in these inferred forces. The charges and masses of different particles could also be inferred. This inference was substantiated by the consistency between mass determined from interactions and from damping coefficients. My work demonstrates the feasibility of using ML to predict governing mechanisms, not just future dynamics, in real experiments, confirming predictions with real experimental data alone. My latest model holds great promise for inferring mechanisms in other many-body systems, such as cells, colloids, and flocking behaviors in macroscopic organisms.

Inferring force laws from many-body systems in dusty plasma by machine learning

By

Wentao Yu
B.A., Zhejiang University, China, 2018

Advisor: Justin C. Burton, Ph.D.

A dissertation submitted to the Faculty of the
James T. Laney School of Graduate Studies of Emory University
in partial fulfillment of the requirements for the degree of
Doctor of Philosophy
in Physics
2024

Acknowledgements

First I would like to express my deepest gratitude to my supervisor, Justin C. Burton, for his unwavering patience and dedication in teaching me. His tolerance during my moments of slackness and genuine concern for my well-being have been the cornerstones of my academic journey. I am also immensely thankful to Ph.D. student Guga Gogia, who was an invaluable guide during my initial two years in the lab.

My heartfelt thanks go to my parents, whose boundless care and support have been my constant source of strength and encouragement in all facets of my life. I extend my appreciation to my roommate, Jin Qian, whose unwavering support and philosophical insights have been a beacon of light during my challenging times.

I am grateful to my collaborators, student Eslam Abdelaleem and Professor Ilya Nemenman, for their expert guidance in machine learning which was crucial to the success of my many-particle project.

A special thanks to all my lab mates—Dana Harvey, Michelle Wang, Zhicheng Shu, Wei-chih Li, Alex Vargas, Derrick Rodriguez, Tabitha Watson, Mingxuan Liu, Nia Smith—and to my former lab mates Brady Wu, Tianshu Huang, as well as our lab manager Schuyler Arn. Their tolerance of my unconscious singing in the lab and their shared quantum life wisdom have enriched my research experience.

I extend my gratitude to my undergraduate friends who generously shared their access to the school cafe, bringing moments of joy and camaraderie to my college life.

Lastly, I acknowledge the financial support from the National Science Foundation under Grant No. 2010524, the U.S. Department of Energy, Office of Science, Office of Fusion Energy Sciences program under Award No. DESC0021290, and the Simons Foundation Investigators Program, which have been instrumental to my research.

Contents

1 Introduction **1**

1.1 Predicting future vs. predicting physics: challenges in real experiments 1

1.2 Our real experiments: dusty plasma (DP) 4

1.2.1 DP Basic theories and their limitations 4

1.2.2 Particles as a tool to refine plasma basics 10

1.3 Previous work in our lab: an intermittent collective phenomenon observed in DP 12

1.4 Overview of thesis topics 15

2 3D tracking of particles in a dusty plasma by laser sheet tomography 17

2.1 Introduction 17

2.1.1 Existing DP video-processing approaches 17

2.1.2 A summary of this work 19

2.2 Experimental design 19

2.3 Laser divergence and parallax correction after tracking 23

2.4 Results: tracking individual 3D trajectories for tens of particles over minutes 27

2.5 Conclusions: benefits of simultaneous kinetic information 31

3 Extracting forces from noisy 1-2 particle dynamics in DP **34**

3.1 Introduction 34

3.2 Experimental methods and particle tracking 36
3.3 single particle motion 39
3.3.1 The linearized model 39
3.3.2 Handling random noise, parameter drift, and measurement error in simulation 42
3.3.3 Features for ML 46
3.3.4 ML methods and performance 51
3.3.5 Labeling experimental data 54
3.3.6 Predicting experimental data - Results 55
3.4 Two particle potion 58
3.4.1 The linearized model 58
3.4.2 Simulation details 59
3.4.3 Features of two particle motion 62
3.4.4 Predicting experimental data - results 63
3.5 Limitations of this approach 67

4 Learning generalized force laws in many-particle DP 70

4.1 Introduction 70
4.2 Experiments and model 72
4.3 Model prediction results 76
4.4 Inference of plasma and particle properties 79
4.5 Conclusion 84
4.6 Appendix for Chap. 4 87
4.6.1 Model details 87
4.6.2 Data processing 91
4.6.3 Fitting of charge and mass for each particle from the model . 92
4.6.4 Dusty plasma simulations 93

5 Conclusion and future directions **100**

Bibliography **106**

List of Figures

1.1 A particle in a plasma 6
1.2 Illustration of the effectively non-reciprocal interaction 11
1.3 The intermittent switching behavior 14

2.1 Setup and calibration of 3D tomographic tracking 22
2.2 illustration and the effect of parallax coupling 24
2.3 Example snapshots of movies by 3D tracking 27
2.4 Example motion of 2 particles in the tracked 15-particle system . . . 28
2.5 Individual particle properties obtained from the tracking 32

3.1 Experiment overview 38
3.2 The model and pixel locking 41
3.3 Velocity distribution 43
3.4 Performance on simulated data 52
3.5 Prediction on experimental data 53
3.6 The two-particle model 57
3.7 Performance on simulated two-particle motion 60
3.8 Prediction on two-particle experiments 62

4.1 Overview of data workflow. 73
4.2 Model's high R^2 76
4.3 Model prediction 80

4.4 Inferring charge and mass 82
4.5 Inferring charge and electrical field as a function of z 85
4.6 Debye length fit 95
4.7 Inference result from simulations 96

List of Tables

3.1 The parameters for 1-particle simulation. 45

3.2 The parameters for 2-particle simulation. 59

4.1 Parameters and model performance from 5 experiments. 77

Chapter 1

Introduction

1.1 Predicting future vs. predicting physics: challenges in real experiments

2000 years ago, people looked into the shining stars in the night sky, wondering what was guiding the motion of these stars. Scientists at that time invented the epicycle, first proposed by Apollonius of Perga at the end of the 3rd century BC (Wikipedia)[1]. The epicycle can fit and predict the future motion of the planets with astonishing accuracy. The epicycle is so beautiful, except that it assumes that the Earth is the center of the universe: a model might be able to perfectly predict a system's future, without knowing any physics behind it. This perfect prediction might lead people to falsely believe that they know the physics. It took people another 1600 years, until about 400 years ago, to discover the correct physics (Newton's Law of Universal Gravitation). The physics in modern scientific frontier systems are much more complicated than the simple inverse-distance-squared formula in Newton's gravity law, especially in glassy systems and biological systems which are typically hydrodynamic many-body systems with fluid-mediated interactions [1–6].

[1] `https://en.wikipedia.org/wiki/Deferent_and_epicycle`, date May 24 2024

Numerous attempts have been made to apply machine learning (ML) to predict the future dynamics of physical systems, or equivalently, to predict 'velocity' or 'acceleration', which can be integrated to forecast future states [1, 2, 7–14]. Apart from predicting the future, some of these works do try to predict specific physical parameters. For example, Smith *et al*. [12] describes an ML model that encodes snapshots from a video of a campfire into a low-dimensional representation to fit an equation for the evolution of these low-dimensional variables. This model is validated by its success in predicting future frames of the campfire, closely matching the actual subsequent frames in the video. Similarly, [9] uses an autoencoder to compress movies of an active nematic system into a low-dimensional representation, with a recurrent neural network modeling the evolution of this embedded data. The effectiveness of their model is demonstrated through accurate predictions of future defect dynamics, aligning with observed data. While this model identified certain qualitative parameter dependencies on the environment in real experiments, such as cells' activity increasing with ATP density, a quantitative measurement of these models' performance remains elusive. This is primarily because it is not possible to plot predicted activity against the exact activity (which is unknown) in experiments. Therefore, the quantitative validation of these ML models inevitably relies on their ability to predict future states accurately, given the lack of precise physics, or formulas, for the complex systems under study. This situation is reminiscent of the period 2000 years ago when the laws of gravity were unknown to scientists.

Other attempts have introduced a functional form to describe the system within a constrained, yet often extensive, library of possibilities [13, 15, 16]. A notable example is the Sparse Identification of Nonlinear Dynamical systems (SINDy) algorithm [16], which has attracted extensive research regarding its convergence theory [17, 18], and has been supported by numerous tutorials [19, 20] and a wide range of applications [21–24]. In SINDy, the goal is to discover the governing equations of a system. Here,

$\dot{X} = \Theta(X)\Xi$ describes the model, where X represents the observed n-dimensional variable. $\Theta(X)$ is an m-dimensional library of candidate nonlinear functions of X (typically a polynomial expansion), and Ξ is an $m \times n$ matrix of coefficients. These coefficients are determined using LASSO, a method that seeks to minimize the number of non-zero coefficients (promoting sparsity) while balancing the accuracy of the model fit.

The core idea is to construct the polynomial expansion library as a high-dimensional linear space where the functions, such as x^2 and x^3, serve as bases. A linear fit (like LASSO) is conducted within this space. These pre-proposed bases can be correlated, and to remove this correlation, further studies [8, 25] analyze training data to obtain a distribution of all these function values. From this distribution, an inner product between two bases can be defined as the correlation between their distributions. With the definition of the inner product in the linear space, a set of orthogonal bases is constructed before proceeding with the model fitting. This approach ensures that the bases used in the SINDy algorithm are mutually independent, enhancing the stability of the model.

This feature-expansion idea has been notably successful in fitting the chaotic Lorentz attractor, where the true governing equations are:

$$\dot{x} = \sigma(y - x) \tag{1.1}$$

$$\dot{y} = x(\rho - z) - y \tag{1.2}$$

$$\dot{z} = xy - \beta z \tag{1.3}$$

with parameters $\sigma = 10$, $\beta = 8/3$, and $\rho = 28$. The Lorentz attractor serves as a comprehensive simulation testbed for numerous ML models [26–28], primarily due to its chaotic behavior and the simplicity of its governing formulas. SINDy's exceptional

ability to predict these equations is anticipated because these equations all fall within the polynomial expansion library that SINDy employs. That's why such algorithms' performance is so fantastic in *simulated* data. In contrast, the governing equations in *real experiments* may be arbitrary and not well-defined. This discrepancy between the experimental data and the simulations used for model training is known as data mismatch, potentially leading to inaccuracies in the model [29, 30]. Furthermore, quantitatively assessing this inaccuracy in real experiments is challenging, as validating the model's performance against an *unknown* ground truth of the physics, rather than the *known* ground truth of the future state, is not feasible.

In summary, the challenges of predicting physics in real experiments are twofold: firstly, the absence of known ground truths, except for future states, in complex modern systems for model validation, and secondly, the often arbitrary and ill-defined nature of the governing equations.

1.2 Our real experiments: dusty plasma (DP)

In my Ph.D. research, I tackle these challenges by deploying physics-constrained machine learning (ML) approaches that utilize neural networks as universal approximators. Unlike traditional methods, my approaches can be validated solely through experimental data, without relying on comparisons to the 'future' states of the system. I have applied these methods to a many-body experimental system known as dusty plasma.

1.2.1 DP Basic theories and their limitations

Dusty plasma is prevalent throughout the universe, from Saturn's rings to interstellar space [31–34], and plays a crucial role in planet formation [35–37], technological processes [38–41], and potentially in the emergence of life [42].

Inside a plasma, neutral atoms are partially ionized into positively-charged ions and negatively-charged electrons. Given a set of physical surfaces (boundaries) that confine a plasma, a conventional model for calculating the ion density field, $n_i(\boldsymbol{r})$, and the electron density field, $n_e(\boldsymbol{r})$, is the Debye sheath model [43]. This model assumes that electrons follow a Boltzmann distribution due to their dynamics being dominated by Coulomb scattering, while maintaining the continuity of ion flux, disregarding ion drift in the sheath region. According to this model, there is an electron-depleted sheath at the plasma's boundary (sheaths form near physical surfaces) where the electric field decreases sharply, and a quasi-neutral pre-sheath layer where ions accelerate towards the boundary. With given boundary conditions, the distributions $n_i(\boldsymbol{r})$ and $n_e(\boldsymbol{r})$ within the sheath and pre-sheath layer can be numerically solved. In the presence of dust particles (Fig. 1.1), the particles become negatively charged as electrons collide with them more frequently, until the repulsion from electrons and attraction from ions due to the negative potential on the particles equilibrate the electron and ion flow towards the particle [44]. A prevalent theory for determining a particle's equilibrium charge, Q, is the orbital-motion-limited (OML) theory [45]. The OML theory first assumes a spherical capacitor approximation, where the particle's floating potential $\phi_f(\boldsymbol{r})$, or the potential at the particle's surface relative to the potential ϕ at that location if the particle were absent, is directly proportional to its inversed diameter d^{-1} and to Q:

$$\phi_f = \frac{Q}{2\pi\epsilon_o d} \tag{1.4}$$

Note that the spherical capacitor theory applies to *vacuum*, while this approximation is a pre-assumption for this charging theory inside a *plasma*. Furthermore, OML theory posits that around a particle whose diameter is significantly smaller than the gas environment's mean free path, both electrons and ions may collide onto the particle within a calculated cross-section. The effect that a collision may remove

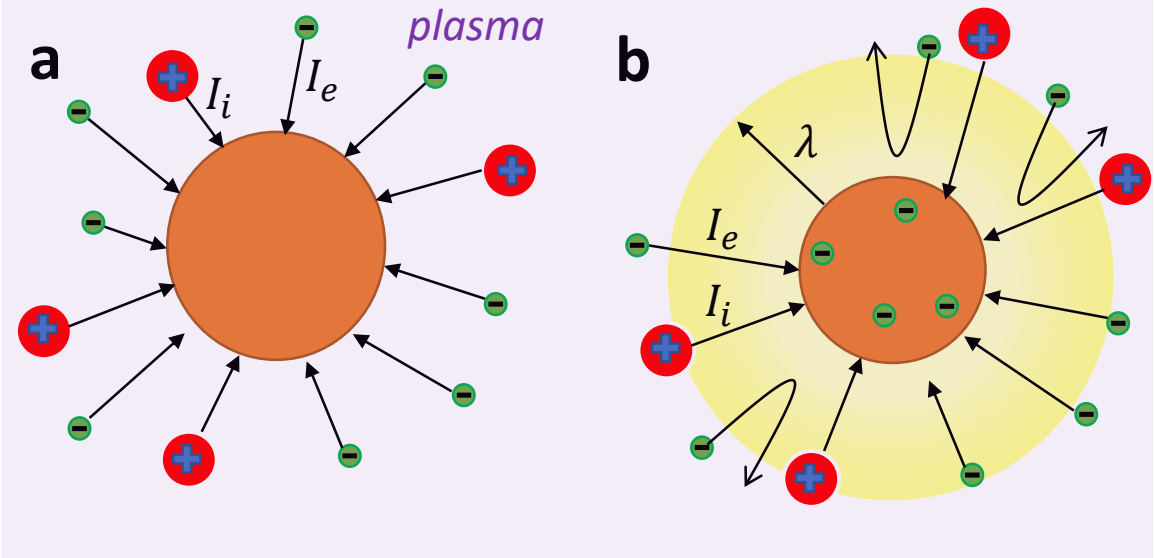

Figure 1.1: (a) Initially when the particle is neutral, more electrons (green) than ions (red) will collide onto the particle, thus $|I_e| > |I_i|$, where I_e is the electron current (negative) and I_i is the ion current (positive), giving the particle negative charge. (b) After some time, the particle accumulates enough negative charge Q. This charge affects local plasma with a characteristic length of λ, and thus fewer electrons and more ions collide onto the particle, and eventually $|I_e| = |I_i|$

the ions' kinetic energy, causing it to fall onto the particle, is neglected. Under this framework, OML theory proposes the following equations:

$$\begin{aligned} \Phi &= \frac{e\phi_f}{k_B T_e} \\ I_e &= -e\sqrt{8\pi} r_d^2 v_{Te} n_e e^{\Phi} \\ I_i &= -e\sqrt{8\pi} r_d^2 v_{Ti} n_i (1 - \frac{T_e}{T_i}\Phi) \\ 0 &= I_e + I_i \end{aligned} \tag{1.5}$$

Here, Φ represents the reduced potential indicating the potential energy of an elemental charge relative to thermal energy. k_B denotes the Boltzmann constant, T_k the temperature of species k, v_{Tk} the thermal velocity of species k, and I_k the electrical current of species k, which must balance at equilibrium. Given known values for T_i, T_e, $n_i(\boldsymbol{r})$, and $n_e(\boldsymbol{r})$, OML theory can compute $Q(\boldsymbol{r})$. With the equilibrium charge Q modeled, the interaction force F^{int} between particles at a scalar separation r is

commonly understood to be a screened-Coulomb repulsion [31]:

$$F^{\text{int}} = -Q\frac{\partial U^{\text{p}}}{\partial r} \tag{1.6}$$

$$U^{\text{p}} = \frac{Q}{4\pi\epsilon_0 r}e^{-r/\lambda} \tag{1.7}$$

Here, U^{p} represents the potential difference induced by the presence of one particle at a distance r, and λ denotes the Debye length, a characteristic plasma property that should not depend on the particles according to this theory. In deriving this formula, it is assumed that the plasma is quasi-neutral, meaning that in the absence of this particle, the background electron and ion densities, $n_{e,0}$ and $n_{i,0}$, as well as the plasma potential ϕ, would be constants, independent of the position $\boldsymbol{r}$:

$$n_{e,0} = n_{i,0} = n_0 \tag{1.8}$$

Under this approximation, according to the Maxwell equation:

$$\nabla^2 U^{\text{p}} = -\sigma/\epsilon_0 \tag{1.9}$$

The net charge density, $\sigma = e(n_i - n_e)$, and the electron and ion density should adhere to a Boltzmann distribution with k being the Boltzmann constant:

$$n_e = n_0 \exp\left(eU^{\text{p}}/kT_e\right) \tag{1.10}$$

$$n_i = n_0 \exp\left(-eU^{\text{p}}/kT_i\right) \tag{1.11}$$

An additional approximation is made, which assumes $|eU^{\text{p}}|/kT_e \ll 1$ and $|eU^{\text{p}}|/kT_i \ll 1$ [46]. Note that this approximation typically does not hold: as a very rough estimation, in a typical experiment [47], particle charge is estimated $Q = -15000e$, $\lambda = 1$ mm, and particle separation $r = 0.5$mm, $U^p(r) = \frac{Q}{4\pi\epsilon_0 r}\exp\left(-r/\lambda\right) = -0.026$ V, and

T_i is approximated to be room temperature 300 K, thus $kT_i = 0.026$ eV. Nevertheless, asserting this approximation holds, the expressions for n_e and n_i simplify to:

$$n_e = n_0 \left(1 + \frac{eU^{\mathrm{p}}}{kT_e}\right) \tag{1.12}$$

$$n_i = n_0 \left(1 - \frac{eU^{\mathrm{p}}}{kT_i}\right) \tag{1.13}$$

Hence,

$$\sigma = e\left[n_0 \left(1 - \frac{eU^{\mathrm{p}}}{kT_i}\right) - n_0 \left(1 + \frac{eU^{\mathrm{p}}}{kT_e}\right)\right] \tag{1.14}$$

$$= -en_0 \left(\frac{eU^{\mathrm{p}}}{kT_i} + \frac{eU^{\mathrm{p}}}{kT_e}\right) \tag{1.15}$$

$$= -\frac{\epsilon_0}{\lambda^2} U^{\mathrm{p}} \tag{1.16}$$

where $\frac{\epsilon_0}{\lambda^2} = e^2 n_0 (\frac{1}{kT_i} + \frac{1}{kT_e})$. In this formula, λ only depends on plasma properties (T_i, T_e, n_0), rather than particle properties (particle charge, radius, etc.) Incorporating this into the Maxwell equation yields:

$$\nabla^2 U^{\mathrm{p}} = \frac{1}{\lambda^2} U^{\mathrm{p}} \tag{1.17}$$

with the boundary conditions being:

$$\sigma(r \to 0) = Q\delta^3(\boldsymbol{r}) \tag{1.18}$$

$$U^{\mathrm{p}}(r \to \infty) = 0 \tag{1.19}$$

This leads to the solution being the screened Coulomb potential Eq. 1.7, with δ being the Dirac delta function. Eq. 1.18 treats the particle as a point charge in the limit that particle diameter d is smaller than any other length scale in the system. More

precisely, this equation can be written by Gauss's law:

$$-\nabla U^P(r = d/2) = \frac{Q}{\pi\epsilon_0 d^2}\hat{r} \tag{1.20}$$

Note that the linearity in Eq. 1.17 is also the ground of other linear relations in the plasma theory, including the sphere capacitor assumption where $q \propto \phi_f$. Under this linearity, suppose U^p is the solution with boundary Q in Eq. 1.18, then CU^p would be the solution with particle's charge CQ where C is an arbitrary constant. In other words, the solution of the field U^p, and the floating potential which is U^p at the surface of the particle, $\phi_f = U^p(d/2)$, would be proportional to Q.

Besides non-linearity, other factors also cause the particle's interaction to deviate from Eq. 1.7. For example, a drift of ion flow (see next chapter) caused by electric field. This drift may shift the distribution of electrons and ions from a Boltzman distribution (eq. 1.11). The breaking of neutrality ($n_e < n_i$) near the physical boundary, and the presence of a magnet field also affects the particle's interaction [31, 48].

Apart from the complicated interactions, which would be the major focus of our study, particles also experience other forces, for example, gravity, confining forces from the environment, neutral drag, and iron drag [44].

Despite the broad acceptance of these charging theories, it's crucial to acknowledge that the approximations I've emphasized in their derivation are typically accurate only to an order of magnitude, especially within the plasma sheath region adjacent to the plasma's boundary. A frequently examined plasma boundary is a semi-infinite plasma space above a horizontal electrode (Fig. 1.21). The direction of the electrode below would be noted as the $-z$ direction throughout this thesis, and due to this symmetry-breaking in z, all parameters including n_e, n_i and Q should be a function of z. With such experimental setups, recent studies have observed significant deviations from these theoretical models [49–53]. Contrary to expectations

that $|Q|$ would monotonically decrease with an increase in z, it is discovered that $|Q|$ peaks at $z \approx 70$ mm. Additionally, [52] utilized particle acceleration measurements in plasma to infer the electrostatic force $F_E = EQ$. The force measured corroborates their revised model, which modifies the electron-depletion assumption in the Debye sheath model based on the OML theory.

Although numerical simulations are frequently used in modeling DP [31, 46, 54], accurately measuring properties like Q and λ experimentally remains challenging due to the intrusive nature of direct probe measurements, which can alter the ambient plasma properties due to the probe's finite size [52, 55–57]. Consequently, up-to-date direct measurements of particle charges are no more accurate than an order of magnitude. For instance, the experiment described in [58] measured dust particle charge to be the order of $10^4 e$. Meanwhile, in a different experiment [59], different particle's charge is estimated to be $(273 - 2519)e$.

1.2.2 Particles as a tool to refine plasma basics

Fortunately, in contrast to finite-sized probes, tiny particles exert minimal influence on plasma. While particles cannot serve as probes in a conventional sense, they inherently have the potential to illuminate plasma properties by their motion, offering insights into their charges and interaction forces. Several fascinating collective behaviors of these particles have been extensively studied, including entropy fluctuations [33, 60], internal resonance [61, 62], and phonons in the vibration of the 2D dust particle 'lattice' [63–68]. In this context, I will delve into two specific phenomena in more detail:

1. Non-reciprocal interaction, modeled in [69]. Non-reciprocal interaction represents a distinctive hydrodynamic effect in dusty plasma (DP). In scenarios where a negatively-charged electrode is positioned below, positively-charged ions drift downwards. This drift is altered by the presence of negatively-charged parti-

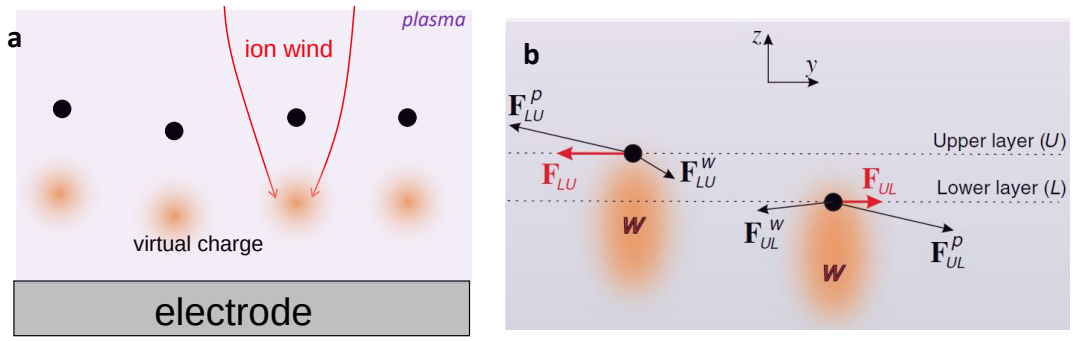

Figure 1.2: (a) A scheme of the origin of plasma wake caused by a semi-finite plasma boundary (an electrode below). (b) Figure 3 in reference [69]. The total force exerted on the upper-layer (U) particle from the lower-layer (L) particle is the sum of the repulsive force F_p^{LU} of direct inter-particle interaction and the attractive force F_w^{LU} from the wake of the lower particle (and similar for the total force on the lower particle). While the direct forces are reciprocal, $F_p^{LU} = -F_p^{UL}$, the wake forces are not, $F_w^{LU} \neq -F_w^{UL}$.

cles, thereby forming a virtual positive charge beneath each particle, known as a plasma wake (Fig. 1.2a). When two particles are located at different vertical positions (z), despite their direct interaction theoretically being reciprocal, the attraction to each other's plasma wake is not (Fig. 1.2b). This phenomenon of non-reciprocity has been experimentally observed and modeled in recent simulations [70–75]. However, a quantitative and accurate inference of this non-reciprocal force from an experimental setup has yet to be achieved.

2. Self-driven motion with 10,000 times thermal energy. A primary theory for energy input, delayed charging, is studied in [76]. To grasp this concept, consider a harmonic oscillator described by $\ddot{z}(t) = -\omega^2 z(t)$, with a solution $z = z_0 \cos \omega t$, $\dot{z} = z_0 \sin \omega t$. No net energy is introduced to the particle by the restoring force within an oscillation cycle, as the net work $W = -\int \omega^2 z \dot{z} dt$, while z and $\dot{z}$ are $\pi/2$ phase separated. However, introducing a delay mechanism in the harmonic oscillator, $\ddot{z}(t) = -\omega^2 z(t - \tau)$, alters the phase separation between z and $\dot{z}$ to exceed $\pi/2$, allowing the restoring force to impart net energy to the particle. In the context of a semi-infinite plasma boundary above a horizontal

electrode, both the vertical electric field $E_z(z)$ and $Q(z)$ vary with z. The vertical electrostatic force counteracts gravity, and as the particle oscillates vertically, its charge requires some time, τ_{ch}, to equilibrate [76], akin to the delayed harmonic oscillator scenario. This concept, along with other theories of energy input into the system such as the vorticity of the ion drag force field [77] and charge fluctuations [78], will be further elaborated on.

1.3 Previous work in our lab: an intermittent collective phenomenon observed in DP

Prior to my arrival at the lab, my colleague Guram Gogia and supervisor Justin C. Burton discovered a bistable switching phenomenon [79]. In our lab, inside an RF-powered Argon plasma, we levitate melamine formaldehyde (MF) particles above an electrode. The particles usually form a quasi-horizontal monolayer. A 532 nm laser beam is focused by a converging lens and then expanded horizontally by a cylindrical lens, to form a horizontal laser sheet, with a vertical thickness of around 130 μm. Particles within this vertical height will be illuminated by the laser sheet, and recorded by a camera above (see Fig. 1.3a). Under a certain plasma pressure P and bias voltage V_{bias} of the electrode, the particles constantly switch between a crystalline state (Fig. 1.3b) and a gas-like state (Fig. 1.3c). The horizontal kinetic energy, whose definition I will elaborate on next, fluctuates with a much longer timescale than any other timescale in the system (Fig. 1.3d). To study this phenomenon, the first question is the source of the energy. We proposed that the self-driven motion of a single particle in the z direction gains energy. Shown in (Fig. 1.3e), we discovered that under certain plasma conditions P and V_{bias}, a single particle experiences a finite-amplitude vertical oscillation, at more than 10,000 times thermal energy. This self-driving behavior is widely studied, as explained in Sec. 1.2.2. Our lab further set a

vertical laser sheet and tracked the vertical motion of a single particle combined with Langmuir probes [47]. Upon numerical simulation, we discovered that, apart from a suitable plasma condition, a certain difference between particles is also critical for this intermittent switching behavior. We further invented a coarse-grained predator-prey model to capture this intermittent-switching behavior [80]. Let A denote horizontal mechanical energy (predator) and B denote vertical mechanical energy (prey), the model reads

$$\frac{dA}{dt} = -\gamma A + cAB(1 - \sqrt{A/B}), \tag{1.21}$$

$$\frac{dB}{dt} = -\gamma B - cAB(1 - \sqrt{A/B}) + w(t)\sqrt{B}\phi\Delta t. \tag{1.22}$$

The first terms on the right-hand side in (1.21) and (1.22) correspond to the power dissipated through hydrodynamic damping. The second term characterizes predation and obeys energy conservation. The functional form cAB is the lowest-order nonlinear term that captures mutual interactions in common predator-prey models. However, in our minimal model, this coupling term arises from energy transfer rates between vertical and horizontal energies and I derived it from classical scattering theory. Note that the asymmetry $\sqrt{A/B}$ comes from the fact that the particles form a quasi-horizontal monolayer, so their scattering frequency should depend on horizontal velocity. $w(t)$ is a Wiener process. The constant c controls the coupling strength, and parametrizes the polydispersity in the many-body system.

While the experimental tracking and the model can capture a *qualitative* intermittent switching behavior, the *quantitative* information can be biased, majorly because the horizontal laser sheet can only capture the 2D motion of particles within this plane. As mentioned before, Horizontal kinetic energy KE_{xy} is defined as $< mv_{\rho,i}^2/2 >_i$, where each particle's mass, albeit with manufactured poly-dispersity which is necessary for the model, is approximated to be the same $m = 0.66$ ng,

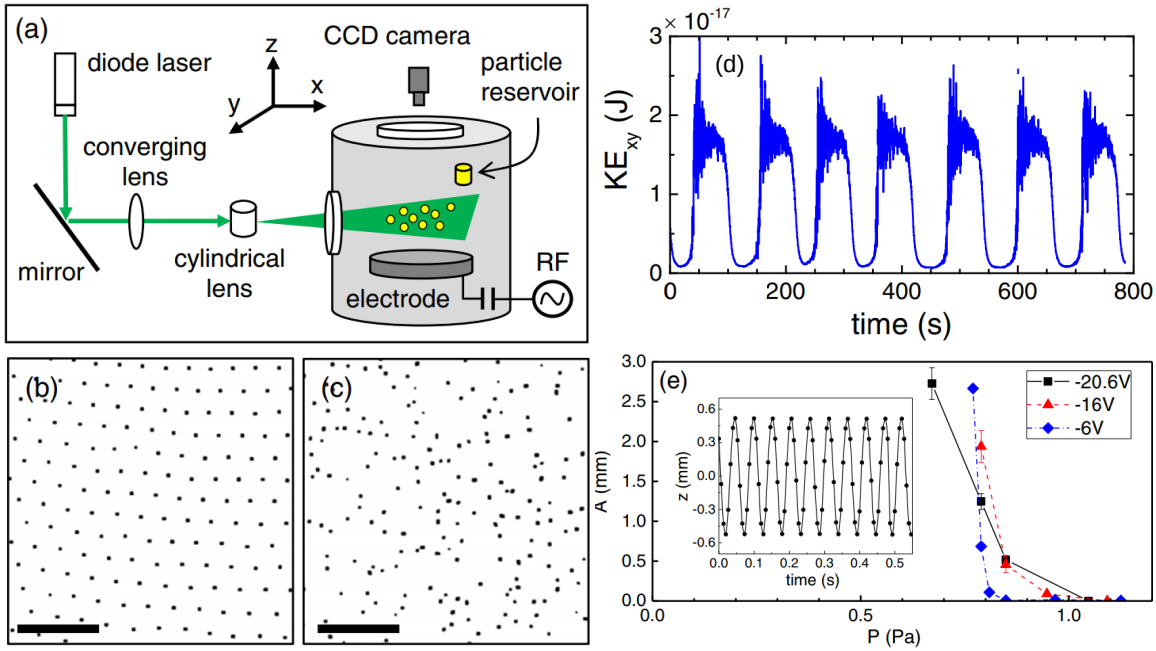

Figure 1.3: Adopted from ref. [79]. (a) Diagram of the experimental setup. The particles were introduced into the vacuum chamber by mechanically shaking the particle reservoir. The particles were illuminated using a horizontal laser sheet. Central regions of crystalline (b) and gaslike (c) samples. (d) Average horizontal kinetic energy per particle at plasma pressure $P = 0.71$ Pa, and bias voltage on the electrode $V_{bias} = -6$ V. (e) Amplitude of a vertical oscillation for a single particle as a function of P for different V_{bias}. Inset: Evolution of the z position of a *single* particle.

and $v_{\rho,i}$ is the horizontal velocity of particle i, and the average $< \cdots >_i$ is conducted on all *tracked* particles. Particles with higher velocity, thus higher kinetic energy, are more difficult to track. The KE_{xy}, calculated from *tracked* particles will thus have a sample bias to be lower than the true horizontal kinetic energy. Furthermore, no information regarding vertical kinetic energy is obtained in this experimental tracking, although it is important in modeling this intermittent behavior. At that time, models regarding vertical kinetic energy purely rely on simulations, with parameters like Q, F^{int} calculated as explained in Sec. 1.2.1, which may not be more accurate than an order of magnitude.

1.4 Overview of thesis topics

As a summary for previous sections, predicting physics in complex, real-world experimental systems presents significant challenges. An illustrative example of such a system is dusty plasma (DP), which has been the subject of extensive study. Theories addressing charging and particle interactions within DP often make approximations accurate only to an order of magnitude, despite the discovery of many intriguing phenomena. Our group has previously investigated the phenomenon of intermittent switching, but our ability to model this behavior heavily relies on simulations that require refinement for increased accuracy. Additionally, at that time, capturing the 3D motion of particles was beyond our experimental capabilities due to the limitations imposed by a 2D tracking setup.

In my Ph.D. research, I have tackled several key challenges in the study of dusty plasma (DP), as detailed across different chapters of my dissertation.

Firstly, as elaborated in Chapter 2, I developed a novel 3D tracking algorithm based on tomography. This innovative approach enables the tracking of individual trajectories of tens of particles simultaneously over several minutes. This breakthrough significantly enhances our ability to observe and analyze the complex dynamics within DP systems [81].

Secondly, Chapter 3 focuses on the study of vibrations of 1-2 particles around their equilibrium positions. I constructed a linear model to describe these small amplitude vibrations and employed machine learning (ML) techniques to determine the linear coefficients. Remarkably, this approach yielded predictions over 50% more accurate than those derived from conventional methods, such as the Fourier spectrum analysis. The validity of this prediction was confirmed through an independent perturbation experiment, offering a robust alternative to relying on the ground truth of future states [82].

Thirdly, in Chapter 4, I utilized the 3D trajectories of tens of particles to infer

pairwise interaction forces, environmental forces, and damping coefficients for different particles through ML. Unlike the linear model that focuses on small oscillations around particles' equilibrium positions, this model is capable of inferring forces at arbitrary particle positions, providing a comprehensive understanding of the forces at play within the DP system. The accuracy and reliability of this model were affirmed by independently inferring the masses of different particles in two distinct ways, with the results showing remarkable consistency. Notably, the exceptional precision of our model enables the observation of plasma and particle parameters that substantially diverge from the conventional theories of plasma previously discussed.

Overall, my research introduces new methods and insights into predicting physics in real experiments, specifically within the context of dusty plasma. These innovations achieve an accuracy far beyond traditional theories and pave the way for new avenues of ML-aided exploration in understanding complex systems.

Chapter 2

3D tracking of particles in a dusty plasma by laser sheet tomography

2.1 Introduction

This work has been published [81].

2.1.1 Existing DP video-processing approaches

A well-developed technology, particle image velocimetry (PIV), can be used to obtain a velocity field from multi-camera movies [83–85]. Calculating the velocity field can reveal spatial and temporal variations in the dynamics, but ultimately averages the individual particle dynamics over some multi-particle length scale. Yet many problems of scientific interest, for example, the mechanism of particle charging and interaction forces, are challenging to investigate without tracking individual particles over long times. Advanced particle tracking velocimetry (PTV) techniques that track individual particles have been mostly applied to the 2D motion of particles using a single camera [86–88]. Some phenomena, for example, stochastic oscillations [89] and spontaneous oscillations [47] can be observed by analyzing individual particle motions

from 2D PTV, but dynamical information perpendicular to the viewing plane is lost. 3D PTV by stereoscopic imaging is plagued by the challenge of delicate calibration of multiple cameras, identifying the same particle appearing in different cameras, and linking those particles over frames. Recent studies have approached this task by using statistical tools [90–92] or machine learning [93–95]. Using statistical inference, the likelihood of a particle at a certain voxel is calculated from the brightness of its calibrated 2D projection in all the cameras, and also the likelihood of a particle existing at this pixel in the previous frame. With machine learning, light spots of particles are simulated by a pre-determined distribution and the model is trained on mapping the videos of multiple cameras to the simulated particle positions. Using these techniques, individual particles in dense dusty plasmas can be tracked for up to 30-50 frames in a volume of 10-100 cubic millimeters [90–92, 94, 96]. In contrast to stereoscopic imaging, 3D tomography relies on a laser sheet that moves relative to the particles. If the position of the laser sheet is known in time, then a sequential series of images can be used to track the particles in three dimensions. In dusty plasmas, 3D tomography has mostly been used to examine static properties at a scan rate of $\approx$ 1 Hz or less [97–101]. Tomography methods have been extended to faster scanning rates, up to 15 Hz [102, 103], yet some experimental problems arise at these speeds. Most noticeably, the inertia of the oscillating mirrors used to deflect the laser limits the size and scanning speed of the imaging volume. Consequently, examining rapidly-moving dust particles for long periods of time remains a challenge. This is important for applications involving dynamical inference of the underlying forces driving the particles, or other dusty plasma phenomena outside of the well-studied Coulomb crystal state.

2.1.2 A summary of this work

Here we report a 3D tomographic imaging and tracking method that is conceptually simple and easy to implement. The method is suitable for tracking multiple particles in large volumes over long times. We use a scanning laser sheet with a single camera to obtain 3D trajectories of particles, saving the difficulties of calibration and identification with multiple mirrors or cameras. Since the particles in a dusty plasma are moving rapidly in time, we oscillate the height (z) of the illuminating 2D laser sheet with a shorter period than the characteristic time of the particle motion, up to a scanning rate of 500 Hz. As a result, particles at a certain z only appear in specific frames of the camera. The images are then processed and particles are identified and tracked by Trackpy [104] using a customized class. Subsequently, the trajectories are calibrated and adjusted for their sub-pixel accuracy. With this technique, we are able to track the 3D trajectories of 1-30 particles for 10,000 or more sequential frames in 1-10 cubic centimeters. We demonstrate this method on two distinct dusty plasma systems driven by vertical oscillations or magnetic field-induced ion flow. The mean particle positions, oscillation amplitudes, and characteristic frequencies of oscillation are reported for each individual particle.

2.2 Experimental design

Our experiments used melamine-formaldehyde (MF) particles with diameters ranging from 8.0 to 12.8 μm (microParticles GmbH). The particles were electrostatically levitated in a low-pressure, 13.56 MHz RF argon plasma above an aluminum electrode with a diameter = 150 mm (Fig. 2.1a, similar to previous experiments [79]). An aluminum ring is placed on the edge of the electrode with a height of 3.7 mm to provide horizontal confinement. The rf plasma was driven with 0.3-5 W of power, and the gas pressure varied from 0.1-1 Pa. In this regime, the typical charge on a single

particle ranged from 10,000-50,000 electrons. The particles were suspended at the edge of the plasma sheath approximately 1-2 cm above the aluminum electrode. The electrostatic confinement provided by the plasma sheath led to a near harmonic 3D trap. Upon displacement from its equilibrium position, a single particle experienced both vertical and horizontal oscillations, with a much higher frequency in z, as will be discussed in Sec. 2.3. Multiple particles in the same system experienced complex interactions often characterized by nonreciprocal forces [69].

To image and accurately track the particles' motion in 3D, a 2.5 W diode laser (Laserglow Technologies) was reflected by a mirror placed $y_0 = 500$ mm away from the center of the particles' motion and then expanded into a 2D sheet using a cylindrical lens (Fig. 2.1a). The sheet was also focused in the z-direction by a plano-convex lens. The intensity profile of the laser sheet at the position of the particles was measured and well-fit by a Gaussian distribution with a standard deviation of 0.13 mm. The scattered light from the particles was captured by a high-speed v711 Phantom camera (Vision Research) located at $z_0 = 525$ mm above the center of the particles. A galvo motor (Thor Labs), driven by a function generator (Agilent 33120A), was used to oscillate the mirror in a sawtooth wave pattern with a tunable amplitude and frequency. The input sawtooth wave frequency (100-500 Hz) determined the scanning frequency of the laser, and ultimately the 3D sampling rate of the particle motion. We note that despite the high-intensity of the diode laser (2.5 W), when the laser is expanded into a sheet and oscillated vertically, the net force provided by the laser on individual particles was negligible.

To calibrate the height of the laser sheet at the center of the electrode during a single cycle of the input sawtooth wave, we built an isosceles right triangle out of stiff paper and placed it directly at the center of the imaging plane ($y = 0$). We then placed a paper rectangle 4 mm behind the triangle (Fig. 2.1b). Impinging light from the laser sheet was partially blocked by the triangle, leaving a bright line on the

triangle whose length varied with height (Fig. 2.1c, the upper line). The remaining unblocked laser sheet projected another line on the rectangle. The apparent length of the bright line on the rectangle varied by a small amount since it moved closer to and farther from the camera lens during a cycle (the lower line of Fig. 2.1c). However, the actual length does not change with laser height, thus the bright line on the rectangle functioned as a fixed length scale at different z-positions so that we may calculate the length of the bright line on the triangle in millimeters. The corresponding height of the bright line on the triangle is then found using the geometry of the triangle since the angles are known.

During the calibration, the camera frame rate was set to 19.95 times the input sawtooth wave frequency on the galvo motor, so 399 frames were captured over 20 cycles. The non-integer ratio of the frequencies led to a small drift so that different z-positions were sampled over many cycles, and those frames could be effectively shifted into one cycle. The calibrated z position of the laser sheet in a cycle, as shown in Fig. 2.1d-e, were near-sawtooth waves with a large area in the center of the cycle where z increased linearly with time. The slope for the linear fit, s, did not sensitively depend on the frequency of the input sawtooth wave. However, the slope scaled linearly with the amplitude of the voltage driving the galvo, as shown in the inset of Fig. 2.1e. With $y_0 = 500$ mm, $s = 3.2$ mm$\cdot$cycle$^{-1}\cdot$ per 100 mV.

In our experiments, we typically set the camera's recording frame rate to 20$\times$ the laser scanning frequency. This provides 20 vertical image slices per cycle. The exposure time was always set at the maximum possible value with the given recording rate in order to capture as much of the scattered light as possible from the particles. We focused the camera sharply on the particles so that corresponding width of the scattered light spots on the image sensor is ≈ 2 pixels. We note that the depth of field of our camera lens was larger than the typical z displacement of particles, so particles appeared in sharp focus despite their vertical motion. Each recorded movie was

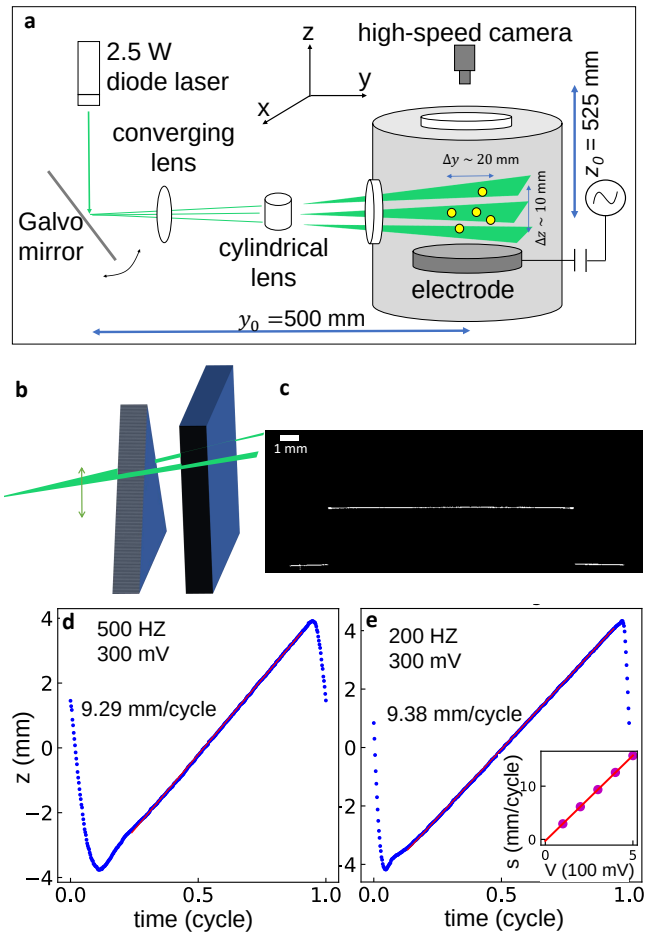

Figure 2.1: (a) Experimental setup for the 3D tomographic imaging and particle tracking. The particles' scattered light from the oscillating laser sheet is imaged from above. (b) Sketch of a triangular screen placed in front of a rectangular screen used for calibrating the dynamics of the laser sheet height. (c) Example image showing the scattered light from the triangular screen (top white line). The two bottom lines are scattered from the rectangular screen. The calibrated height of the laser sheet with input sawtooth wave voltage = 300 mV and frequency = 500 Hz (d) and 200 Hz (e). Linear fits to the central region are shown with red lines. The slope s of the linear fit versus input voltage with fixed frequency = 200 Hz is plotted in the inset of (e).

processed by Trackpy [104]. A customized 3D-frame class, included in the supporting information, was used to group every 20 frames into a bundle, automatically detect from which frame a bundle began, and discard the first and last 2 frames in each bundle (they exist outside of the linear region in Fig. 2.1d). The code, as provided in the supplemental information, produces a rudimentary database which contains the positions x', y', and z' for each particle in each frame. After the initial tracking, the code also applies a SPIFF correction to alleviate small statistical errors in tracking due to pixel-locking [105]; a known and significant tracking issue that arises when the width of a particle light spot is comparable to the pixel size.

2.3 Laser divergence and parallax correction after tracking

In our experiments, gravity and electrostatic forces within the plasma sheath near the aluminum electrode are the largest forces exerted on the particles (both in the z-direction). These forces are approximately 10-100$\times$ larger than the horizontal confinement forces since the diameter of the electrode (15 cm) is much larger than the levitation height (1 cm). Additionally, the vertical confinement forces are much larger than typical particle interaction and drag forces, which is common for dust particles levitated in RF plasma sheaths [79]. As a result, particles experienced natural oscillations with frequencies $f_z = 4-25$ Hz in z and $f_{xy} = 0.5-3$ Hz in the xy plane. The wide range of frequencies comes from two distinct experiments with different environmental conditions, as discussed in Sec. 2.4. Since particles move above and below the focal plane (Fig. 2.2a), there is a small amount of imaging parallax, or coupling between the vertical and horizontal positions. The tracked, rudimentary trajectories with coordinates x', y', and z' are different from the desired Cartesian coordinates x, y, and z. In one experiment, the natural frequency of oscillation in the xy plane was

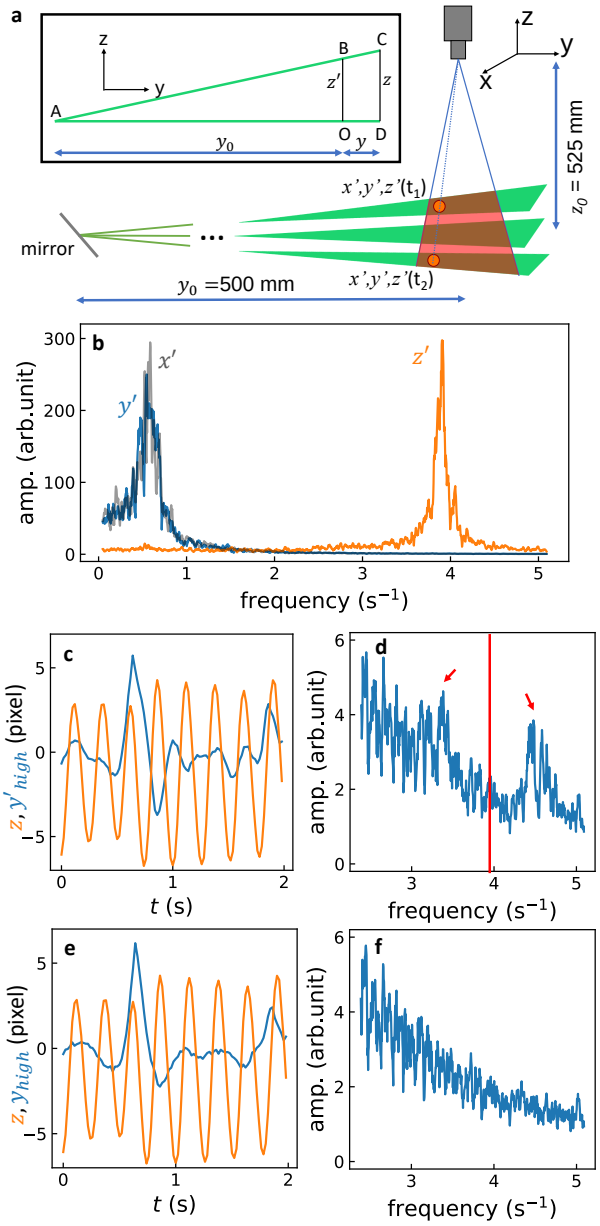

Figure 2.2: (a) Diagram showing the intersection of the solid angle of view from the camera and the laser sheet (red shaded area). Two particles at different x and y may have the same x' and y' when viewed from the camera (the blue dotted line). Inset: the $y-z$ plane of view for the geometry of the imaging system. The mirror is at A. A particle located at C will appear at the same height z' as B. (b) The Fourier spectrum of x' (gray), y' (blue), and z' (orange). The amplitude of z' is magnified by 10x for clarity. (c) The high-frequency band, y'_{high}, of the y' component from the rudimentary trajectory of a tracked particle shows a correlation with its z position. (d) The Fourier spectrum of y' has peaks at ≈ 3.3 Hz and 4.5 Hz, indicated by the red arrows, which is related to the vertical oscillation frequency, 3.9 Hz, indicated by the red line. (e) After the micro-correction procedure, the high-frequency band, y_{high}, of the y component from the same particle shows no correlation with z. (f) After the micro-correction, the Fourier spectrum of y no longer displays a peak.

≈ 0.6 Hz, and the frequency in the z direction was ≈ 3.9 Hz (Fig. 2.2b). As a result of the imaging parallax, the high-frequency band (> 2.5 Hz) in the Fourier transform of either x' or y' from single particles is highly correlated with oscillations in the z position, as shown in Fig. 2.2c. Two sideband peaks near 3.3 Hz and 4.5 Hz appear in the Fourier spectrum of y'_{high}, which stems from an amplitude modulation of the y position due to z oscillations, essentially mixing the signals (Fig. 2.2d).

To understand the origin of these sideband peaks, we first introduce a geometric, first-order linear correction used to handle the conversion between imaged, primed coordinates and the real Cartesian coordinates, denoted as a "micro-correction" in the tracking code. The micro-correction is applied with the following transformation:

$$z = z' \frac{y_0 + y'}{y_0}, \tag{2.1}$$

$$y = y' \frac{z_0 - z}{z_0}, \tag{2.2}$$

$$x = x' \frac{z_0 - z}{z_0}. \tag{2.3}$$

The first line corrects for the divergence of the laser sheet; particles imaged in the same frame may have slightly different actual z positions (Fig. 2.2a). As $y'/y_0 \to 0$, this correction becomes negligible. Note that Eqs. 2.1-2.3 are derived purely from geometry. As shown in the inset of Fig. 2.2a, point A is the mirror, O is the center of the particle system, and line OB is the axis where the calibration of z is conducted. A particle at position C will appear in the same frame as a particle at point B. The measured z' is BO, while its actual z is CD. By trigonometry:

$$\frac{z}{z'} = \frac{y + y_0}{y_0}, \tag{2.4}$$

which is equivalent to Eq. 2.1. Note that y' is used instead of y in the numerator of Eq. 2.1. However, this is a second-order effect $\mathcal{O}((y/y_0)^2)$, where $y/y_0 \approx 0.02$.

Equations 2.2 and 2.3 represent a first order correction for imaging parallax, which is negligible as $z/z_0 \to 0$. The derivation is identical to Eq. 2.1, except that the y axis is replaced by $-z$ and z is replaced by y.

To demonstrate why the sideband peaks are observed at 3.3 HZ and 4.5 HZ, respectively, we will assume a simplified model where a single particle's true trajectory is sinusoidal, given by:

$$y = A\cos(\omega_y t + \phi), \tag{2.5}$$

$$z = B\cos(\omega_z t). \tag{2.6}$$

Due to parallax, as shown in the inset of Fig. 2.2a, the measured y-position, y' is

$$\begin{aligned} y' &= y + \frac{yz}{z_0}, \\ &= y + \frac{AB}{z_0}\cos(\omega_y t + \phi)\cos(\omega_z t), \\ &= y + \frac{AB}{2z_0}\left(\cos(\omega_z t - \omega_y t - \phi) + \cos(\omega_z t + \omega_y t + \phi)\right). \end{aligned} \tag{2.7}$$

Therefore, imaging parallax causes peaks in the Fourier spectrum of y' at $\omega_z - \omega_y$ and $\omega_z + \omega_y$, which correspond to 3.3 Hz and 4.5 Hz.

This linear correction is sufficient to remove the coupling between positions in the xy plane and z, as shown in Fig. 2.2e. The correlation between z and y_{high} (the high-frequency band of the corrected y coordinate) has been removed. Also, the peaks at 3.3 Hz and 4.5 Hz no longer exist in the Fourier spectrum of y after the correction (Fig. 2.2f). Finally, we note that since particles at different z positions are recorded at slightly different times, the final time series of positions for a given particle may have non-uniform intervals. To obtain uniform time intervals between bundles, we use interpolation to the central time of each z bundle.

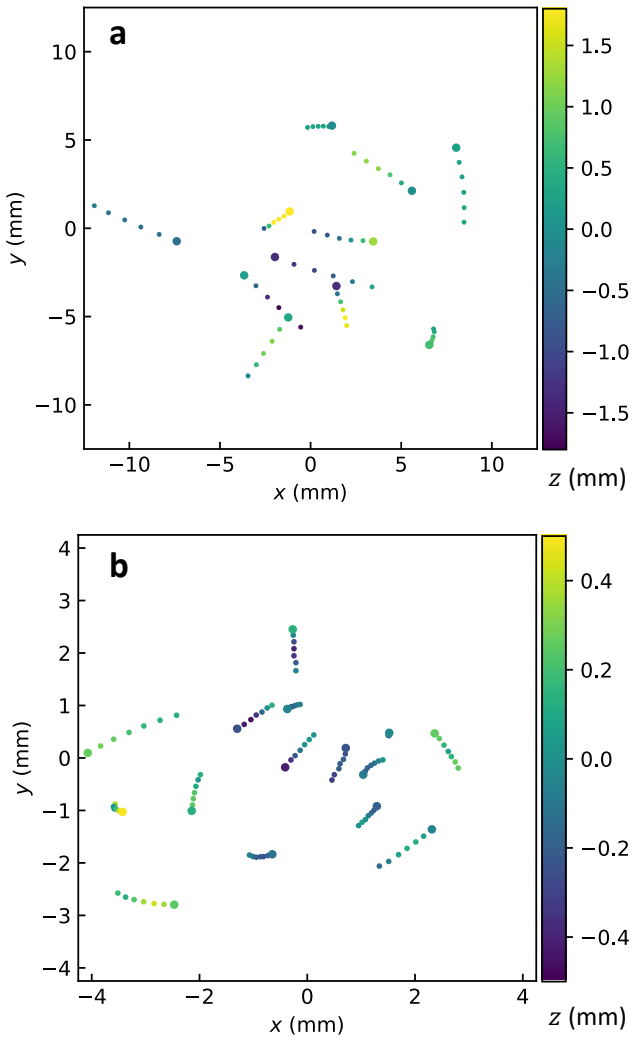

Figure 2.3: (a) Snapshot of particle positions from a tracked, 11-particle system at 0.1 Pa. The z position is indicated by the colorbar. The colored tails represent the positions in the previous 5 bundles. (b) Snapshot of particle positions from a tracked, 15-particle system at 1.0 Pa. Here, the presence of the magnetic field leads to a much stronger confinement.

2.4 Results: tracking individual 3D trajectories for tens of particles over minutes

To demonstrate our imaging and tracking method, we used two collections of MF particles in distinct environmental conditions. At very low plasma pressure (0.1 Pa), we tracked an 11-particle system that was highly underdamped due to the low gas

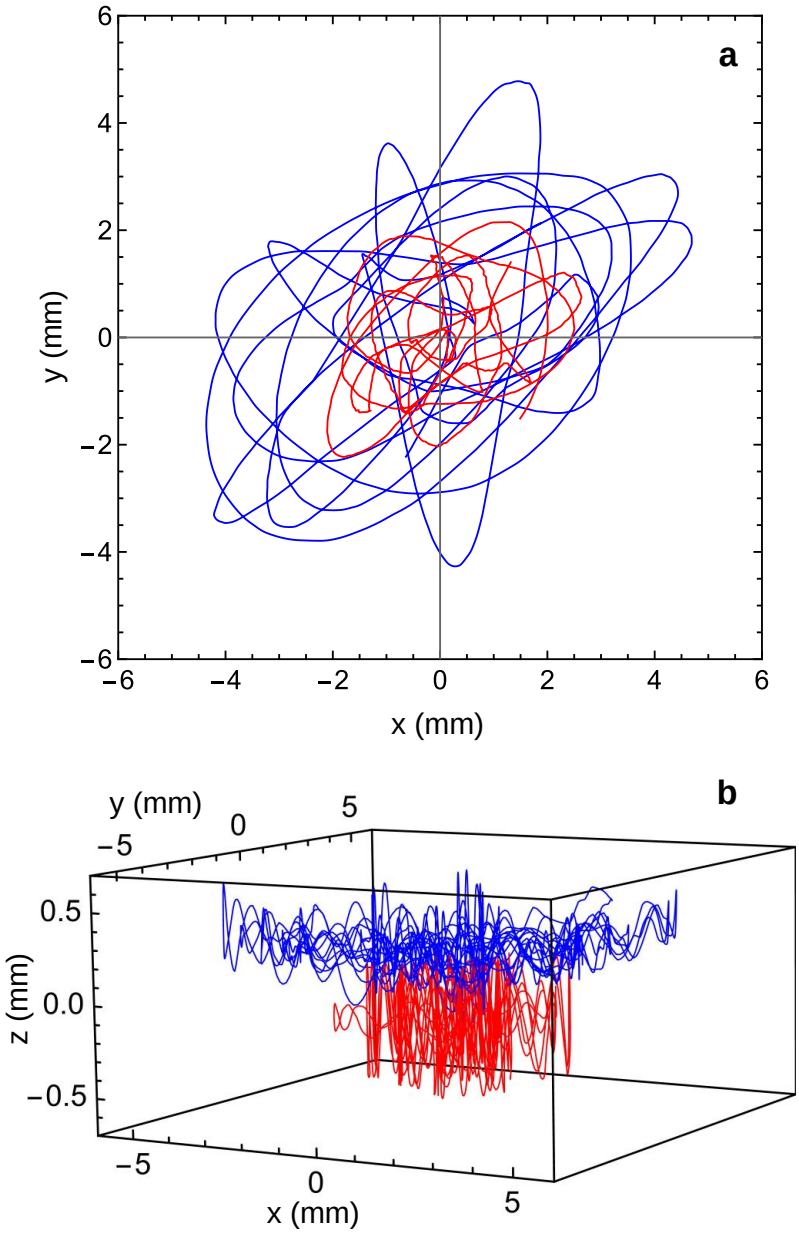

Figure 2.4: (a) Projection in the xy plane of the motion of 2 particles within a system of 15 particles. The system was driven by ion flow from a permanent magnet, as described in the text. The length of each trajectory is 5 s, and the sampling period is 0.005 s. (b) The motion of the same 2 particles plotted in 3D. One particle (red) sits considerably lower in z due to its larger mass. Both particles oscillate rapidly in the z-direction. In both panels, trajectories are connected by quadratic interpolation.

pressure. The particles experienced spontaneous vertical oscillations with amplitudes ≈ 1 mm, which acted as a source of constant energy input into the system [47, 106]. In the xy plane, the particles moved with much larger amplitudes (≈ 10 mm). To track the system, the laser scanning frequency was set to 50 Hz and the camera frame rate was set to 1,000 Hz. The tracked particle positions at a single point in time are illustrated in Fig. 2.3a. In a second experiment, we placed a large, 7.5 cm diameter rare-earth magnet within a cavity machined into the electrode. The vertical component of the magnetic field was measured to be ≈ 0.05 T at the levitation height of the particles. The gas pressure was set to 1.0 Pa. Under these conditions, the particles experienced rapid vortical motion in the xy plane with a rotation period of ≈ 0.5 s. This voticity stems from an ion drag force since ions streaming towards the aluminum electrode have a finite velocity component in x and y, and thus are deflected by the magnetic field [107, 108]. The amplitudes of particle oscillations were ≈ 3 mm in the xy plane and ≈ 0.2 mm in z. To track the system, the laser scanning frequency was set to 200 Hz and the camera frame rate was set to 4,000 Hz. The tracked particle positions at a single point in time are illustrated in Fig. 2.3b. For both systems, we successfully and continuously tracked more than 10,000 frames without confusing particle positions or losing particles. Sample movies from these systems can be found in the supplementary information (Movie S1 and Movie S2).

With the advantage of high-speed, 3D tracking, we can follow the motion of individual particles in a many body system over long times. In Fig. 2.4 we show the trajectories for 2 particles over 5 s (1000 frames) from the second system, where particles experience vortical motion due to the external magnetic field. Figure 2.4a depicts just the motion within the xy plane, which could be captured with traditional 2D particle tracking methods. One particle experiences a much larger range of motion (blue), whereas the other particle is more tightly confined to the center (red). In 3D, we see that this is because of their difference in mass, and thus their

corresponding vertical positions (Fig. 2.4b). The particles are separated by ≈ 0.5 mm in z. Both particles experience rapid vertical oscillations that are not observable in the 2D projection.

Despite attempts to use identical particles when conducting experiments, the manufacturing process always leads to a degree of heterogeneity. By tracking particles in 3D, we can harness the particles' heterogeneity to investigate their local plasma environment. Figure 2.5a shows that particles that resided higher in the sheath (blue) always moved horizontally with a larger amplitude than average (magenta), and the particles that resided lower in the sheath (red) always moved with smaller amplitude. Here the amplitude is defined as the standard deviation (std) of the particle position over some time window. However, the amplitude of vertical oscillations was more intermittent with longer timescales, but generally showed the the same behavior (Fig. 2.5b). For example, although the bottom (red) particle moved less in z than average, during the last 5 s of the experiment, it experienced a larger amplitude of oscillation in z (trajectories for these particles are shown in Fig. 2.4b).

When averaged over the entire time series, the standard deviation of motion in z increased with the mean z position, meaning that lighter particles residing higher in the sheath experienced larger oscillations (Fig. 2.5c). However, the vertical oscillation frequency (f_z) of each particle was most strongly correlated with the mean z position, as shown in Fig. 2.5d. Smaller particles sat higher in the sheath, and had a higher oscillation frequency. In principle, one can obtain the variation in the vertical electric field from the variation in f_z. Yet in practice, both the electric field and particle charge vary with z, which complicates this inference [47]. By considering particle interactions, one may use the 3D trajectories to infer pairwise forces between particles (including estimates of the charge and mass) or predict their future motion, which may be further used to infer forces from the plasma environment. Finding low-dimensional representations of dynamics or new physical laws from many-body trajectories using

machine learning is a rapidly expanding field of research [15, 16, 24, 109, 110]. Our tracking method, combined with a machine learning-based algorithm, provides an opportunity to better understand the complex dynamics of dusty plasmas. For the next sections, I will describe how to analyze the 3D trajectories made possible by this tracking algorithm.

2.5 Conclusions: benefits of simultaneous kinetic information

3D tomographic imaging and tracking of dusty plasmas provides new ways of studying dust dynamics over large, ergodic time scales. In particular, detailed information about the position and acceleration of each particle can reveal information about the spatial dependence of environmental and interaction forces between particles. The method is complementary to more well-developed, stereoscopic imaging methods, where smaller imaging volumes are examined over very short periods of times ($\approx$ 100 frames). Stereoscopic methods are appropriate for much denser dust systems, and do not require a very high-speed camera capable of thousands of frames per second. Although we have only focused on systems with 10-20 particles here, our tomography method can be scaled up to many more particles, however, not without some challenges. The main restrictions to tracking larger numbers of particles involve temporal and spatial resolution. The camera and corresponding laser sheet frequency must be fast enough to capture oscillations in z and close encounters between particles, where forces and accelerations can be large. Additionally, during a close encounter, where two or more particles come within 2 voxels, Trackpy may confuse the identity of those particles. Trackpy first identifies particles in each frame separately before linking all the located records. Thus during particle identification, information from the previous and next frame is not used. This problem could be improved with

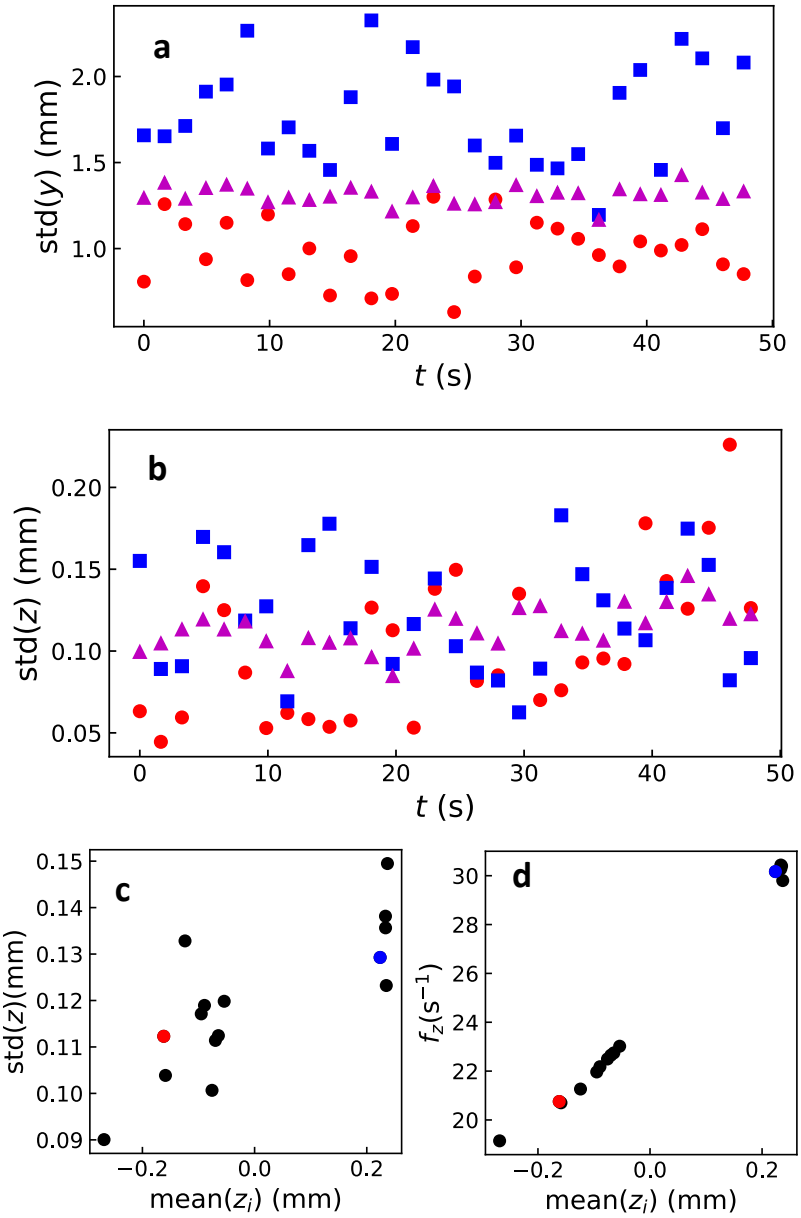

Figure 2.5: The oscillation amplitude in y (a) and z (b) for two particles (red circles, blue squares); the same as shown in Fig. 4. The amplitude is computed using the standard deviation of positions in binned time windows of width 1.65 s (330 frames), which is 3x the horizontal period. The magenta triangles are the average amplitude for all 15 particles. The oscillation amplitude (c) and peak frequency (d) in z are calculated for each of the 15 particles over the whole time series. The two particles shown in Fig. 4 are colored blue and red, respectively.

more advanced tracking algorithms, for example, the shake-the-box algorithm [92]. Furthermore, statistical information such as the average brightness, average kinetic energy, and average z position can potentially be used to better identify individual particles and link them before and after a close encounter.

Chapter 3

Extracting forces from noisy 1-2 particle dynamics in DP

3.1 Introduction

This work has been published [82].

ML has already been applied to a few distinct areas of dusty plasma research. Examples include the interpretation of Langumir probe and electron density measurements [111–113], and the prediction of particle generation and annihilation in fusion devices [114]. Additionally, ML has been used to identify phase boundaries in dense dust systems [115], and to assist with stereoscopic tracking of many particles in three dimensions [116]. Bayesian analysis and ML have also been applied to investigate the nonlinear dynamics of single dust particles [117]. Importantly, these dynamics provide information about the dust charge, interaction potential, and external fields, essentially acting as a non-contact probe of the system. Both the dust charge (Q) and Debye screening length (λ) between interacting dust particles can by estimated by an analysis of the noisy dynamics [118], two parameters which are often difficult to accurately measure. Here we show how the undisturbed, random motion

of one and two particles in a dusty plasma can be interpreted using ML to provide accurate information about their inter-particle and environmental forces. Crucially, our ML methods are trained with simulations that consider real experimental artifacts such as anisotropic confinement, nonconservative forces, stochastic Lévy noise, non-Gaussian tracking error (pixel-locking), and experimental drift. These artifacts can be observed in a statistical analysis of the data, yet they rarely included in dynamical inference procedures, leading to data mismatch. In our procedure, features are extracted from the simulated trajectories to train supervised ML models. The models simultaneously predict system-wide parameters with 50% better accuracy than traditional methods such as Fourier spectrum and maximum likelihood estimation in simulated trajectories.

In the experiments, one key feature is that many of the parameters are independently inferred by analyzing the particles' recovery to equilibrium after a perturbation, thus labeling the data and verifying the model's performance on experimental time series. Based on labeling with this alternative method, our prediction on experimental data is evaluated to have the same accuracy as simulated data, alleviating data mismatch. Furthermore, in experiments with two particles, we provide an accurate estimation of Q and λ solely from the particles' pixel-scale Brownian motion without knowledge of other system-wide parameters, such as Epstein damping. These results will help guide other studies that use ML to quantitatively infer system parameters in real-world, noisy experimental data.

In this chapter, some approximations mentioned in chap. 1 are assumed, including Eq. 1.7. The rest of this chapter will be organized as follows: in Sec. 3.2, we adopted the experimental setup as introduced in the previous chapter, and more details regarding the tracking errors are discussed. In Sec. 3.3.1, we introduce the linearized single particle model used for our simulations. Section 3.3.2 explains the dominant source of errors in our experiments. Their mismatch from non-correlated Gaussian

noise that is commonly used in simulations is observed by statistical analysis. We then explain how we handle these errors in our simulations. In Sec. 3.3.3, we describe the features extracted from simulated and experimental data. These features are used by our ML models. Section 3.3.4 explains the different ML models and their corresponding performance on simulated test data compared with conventional methods. Section 3.3.5 describes the alternative way that we label our experimental data. Finally, Sec. 3.3.6 demonstrates the performance of our ML models on experimental, single particle data. Section 3.4 expands our methods to systems of 2 particles. In Sec. 3.4.1, we introduce the changes to the linearized model for 2 particles. Section 3.4.2 and 3.4.3 explain the simulation details and the features used for the ML models. Lastly, 3.4.4 shows our predictions on experimental two-particle data, including an inference of the particle charge and Debye length. Finally, Sec. 3.5 discusses the limitations of this approach, and the directions for further study as detailed in Chap. 4.

3.2 Experimental methods and particle tracking

Our experiments used melamine-formaldehyde (MF) particles with diameters 9.46 $\pm$ 0.10 μm and 12.8 $\pm$ 0.3 μm (microParticles GmbH). The particles were electrostatically levitated in a low-pressure argon plasma above an Aluminium electrode with a diameter of 150 mm (Fig. 3.1a), similar to previous experiments [47, 79]. The argon plasma was generated by a 13.56 MHz radio-frequency voltage applied to the electrode, resulting in 2.9 $\pm$ 0.1 W of input power and a fixed dc bias voltage of -36.3 $\pm$ 1.2 V. An Aluminium ring was placed on the edge of the electrode to provide horizontal confinement. The plasma pressure, P, was varied between 0.6 Pa and 1.3 Pa. Under these conditions, the typical electron temperature in the plasma was 1.3-1.5 eV [47].

As explained in Chap. 2, to visualize the particles levitated in the plasma environment, a horizontal laser sheet was generated by focusing with a cylindrical lens, similar to previous experiments [47, 79, 80]. The scattered light from the particles is captured from above by a Phantom V7.11 high-speed camera equipped with a macro lens. This allowed tracking the particle positions in the horizontal, xy-plane. Additionally, we used a mirror attached to a galvo motor to oscillate the laser sheet with a 50 Hz sawtooth wave at an amplitude of a few millimeters. The timebase of the camera was synchronized to the function generator driving the galvo, and the camera recorded at 1000 Hz (Fig. 3.1a), resulting in 20 images at different vertical positions per oscillation of the laser sheet. With this tomographic 3D tracking, we simultaneously obtained information about the vertical and horizontal motion of the particles.

The spatial resolution of our imaging system was 51 μm per pixel in the xy-plane, and 200 μm between image slices in the z-direction. However, by tracking the 3D particle motion using an open source software (TrackPy [104]), the position of the particles can be located with much better accuracy. The image representing the scattered light from a single particle is shown in Fig. 3.1b. The centroid of the particle "blob" is found by calculating the center-of-mass of the pixels, where the pixel brightness represents the mass contribution of a single pixel [104]. The same centroid procedure is done with image slices in the z-direction. A probability density function of the decimal part of the tracked positions (x_d) is shown in Fig. 3.1c, showing a strong bias towards integer values. This bias is known as pixel-locking [119]. Using the single-pixel interior filling function (SPIFF) algorithm [105, 120], these errors can be statistically corrected from the tracked data. Ultimately, our estimated sub-voxel resolution in tracking the particles was ≈ 4 μm in the xy-plane, and ≈ 16 μm in z.

This sub-pixel error was confirmed using an independent procedure. We created digital movies of bright "particles" moving unidirectionally across a projection screen.

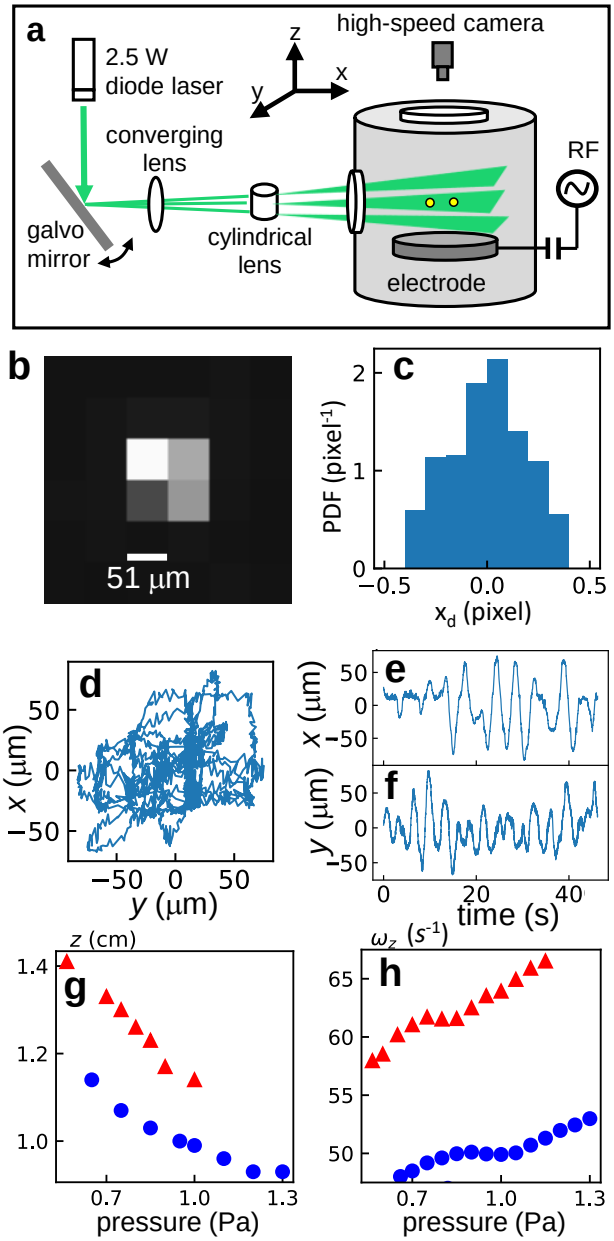

Figure 3.1: (a) Experimental setup for the 3D tomographic imaging and particle tracking. The oscillating mirror varies the angle of the incoming laser (wavelength 532 nm). The converging lens focuses the beam in z, and the cylindrical lens expands the beam in the xy plane. Particles are imaged and tracked from above as described in the text. (b) Image of the scattered light from a single particle with diameter 12.8 μm. (c) Probability distribution of the decimal part of tracked positions, prior to SPIFF correction. (d) A 45 s trajectory for a single 12.8 μm particle undergoing stochastic motion. (e-f) Time series of the x and y position corresponding to the same trajectory. (g) z-position as a function of pressure for 12.8 μm (blue circles) and 9.46 μm (red triangles) particles. (h) Dominant frequency of motion in the z-direction for both sizes of particles, obtained by Fourier transform.

The screen was imaged with our camera so that the particles appeared similar in size on the camera sensor when compared to the experiments (i.e. Fig. 3.1b). Since the trajectory of the particles was pre-determined in the movie, we compared the tracked positions to the known values. Despite these procedures, the horizontal resolution was still a significant fraction of the amplitude of the Brownian motion in the experiments. This was evidenced by systematic statistical effects in the analysis of the dynamics, and will be discussed in Sec. 3.3.2.

3.3 single particle motion

3.3.1 The linearized model

A typical xy trajectory for a single, isolated particle is shown in Fig. 3.1d. The x and y time series corresponding to this trajectory is shown in Fig. 3.1e-f. Without any external perturbations, the particle experienced thermally-excited motion in three dimensions. The amplitude of the motion was ≈ 50 μm in the xy plane. A dominant angular frequency of motion ($\omega \approx$ 1-2 Hz) is clearly visible in the time series. The amplitude of motion in z was much smaller; less than our spatial resolution. Nevertheless, we measured the z-position of the particle as a function of gas pressure (Fig. 3.1g), which increased at lower pressure as the electrode's sheath expanded. Also, by Fourier transforming the time series of the z-position, we estimated the vertical frequency of oscillation (ω_z, Fig. 3.1h), which was much larger than the horizontal frequency, indicating strong confinement in the z-direction.

Due to the small amplitude of motion, to the lowest order, the particles behaved as stochastic harmonic oscillators. Since the amplitude of motion in z was much smaller due to the strong confinement, we will ignore motion in the z-direction for our linearized model. Let $\vec{\mathbf{r}}(t) = x(t)\vec{\mathbf{e}}_x + y(t)\vec{\mathbf{e}}_y$ denote the two-dimensional (2D) position of a particle at time t, and dotted variables refer to time derivatives. The

linearized dynamics of one particle reads:

$$\ddot{\vec{\mathbf{r}}} = -\vec{\nabla}\phi + \vec{\nabla} \times \vec{\mathbf{A}} - \gamma\dot{\vec{\mathbf{r}}} + \vec{\mathbf{N}}(\alpha) \tag{3.1}$$

$$\begin{aligned}\phi =& \frac{\omega^2}{2}[(1-\delta)(x\cos\theta + y\sin\theta)^2 + \\ & (1+\delta)(-x\sin\theta + y\cos\theta)^2]\end{aligned} \tag{3.2}$$

$$\vec{\mathbf{A}} = \frac{k_c}{2}(x^2+y^2)\vec{\mathbf{e}}_z \tag{3.3}$$

This model contains 6 parameters, γ, ω, δ, θ, k_c, and α. The deterministic confinement force has two components. The conservative potential ϕ resembles a 2D spring characterized by 3 parameters: the average frequency ω, the asymmetry δ between two principal axes, and the angle θ from the x-axis to the weaker principle axis. Two eigenfrequencies, $\omega_- = \omega\sqrt{(1-\delta)}$ and $\omega_+ = \omega\sqrt{(1+\delta)}$, and θ are displayed in Fig. 3.2a. The nonconservative vector potential $\vec{\mathbf{A}}$, characterized by a parameter k_c, represents a rotational force possibly due to drag from the background ion flow [121], particle asymmetries [122], or magnetic fields [123].

Additionally, the particle experiences drag from the background neutral gas. According to Epstein's law assuming diffuse reflection from neutral gas collisions on the particle surface, the damping coefficient can be expressed as [44, 124]:

$$\gamma = 1.44\frac{P}{a_p\rho_p}\sqrt{\frac{2m_{\mathrm{Ar}}}{\pi k_B T}}. \tag{3.4}$$

Here, P is the gas pressure, a_p is the particle radius, $\rho_p = 1510$ kg/m^3 is the mass density of the particle, m_{Ar} is the mass of an argon atom, k_B is Boltzmann constant, and $T = 300$ K is room temperature. An important assumption here is that the particle size is smaller than the mean free path (≈ 5 mm at $P = 1$ Pa). For the particles with diameter $2a_p = 12.8$ μm, $\gamma/P = 0.95$ Pa^{-1} s^{-1}. For the particles with diameter $2a_p = 9.46$ μm, $\gamma/P = 1.29$ Pa^{-1} s^{-1}.

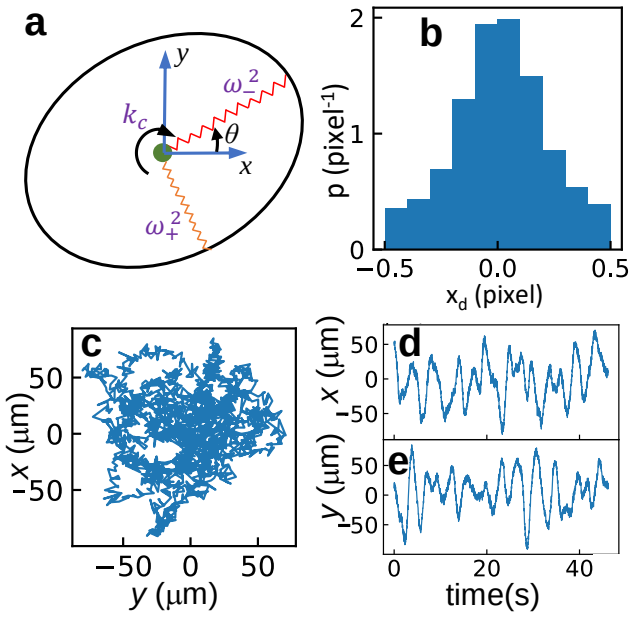

Figure 3.2: (a) Linearized external forces on the particle, as described in the text. The black circle represents an equipotential surface of the harmonic confinement. The eccentricity is exaggerated. (b) Probability distribution of the decimal part of positions after simulated pixel-locking. (c) A simulated trajectory of length 45 s for a single particle undergoing stochastic motion. (d-e) Time series of the x and y position corresponding to the trajectory shown in (b).

3.3.2 Handling random noise, parameter drift, and measurement error in simulation

The last term in Eq. 3.1 is a stochastic acceleration, $N(\alpha)$, which follows a stable Lévy distribution. The parameter α will be determined by inference. We do not assume a priori that the stochastic motion is purely Brownian ($\alpha = 2$), and $\alpha < 2$ indicates a more heavy-tailed distribution. The Brownian motion of particles in experiments is driven primarily by random impulses from the environment. Thus, in the simulations, temporally-independent random noise is added to the *acceleration* of the particles at each time step. The Lévy-stable noise was generated by the python function *scipy.stats.levy_stable* with parameter skewness $\beta = 0$ and center $\mu = 0$. The noise scale c and the parameter for heavy-tailness $\alpha \in (1.6, 2.0)$ was independently chosen for each simulation.

For all simulations, we used a time step $\Delta t = 0.02$ s to closely follow the experiments. The parameters ω, γ, δ, θ, k_c, and α are randomly chosen from a uniform distribution prior to each simulation. The range of values possible for each parameter are listed in Table 3.1. For the maximum values of k_c, we chose $k_{c,max} = \min(1\ \mathrm{s}^{-2}, 0.9 \times \sqrt{\omega^4\delta^2 + \omega^2\gamma^2})$, which guaranteed that the confinement force was able to provide the necessary centripetal acceleration to keep the particle in a bounded stable orbit. Since none of the parameters have a length scale in their units, the simulated Lévy noise scale was arbitrarily set to $c = \sqrt{\gamma\omega^2/\Delta t}$.

Drift was inevitably present in nearly all experiments. This was most noticeable in the drift of the equilibrium position of the particle. The drift was small, less than 1 pixel, but is still comparable to the amplitude of the Brownian motion. We modeled this in simulations as a temporally-correlated Gaussian noise added to the *equilibrium positions*. To simulate a time series of temporally-correlated noise, a_i, with standard deviation (STD) σ and characteristic correlation time τ much larger

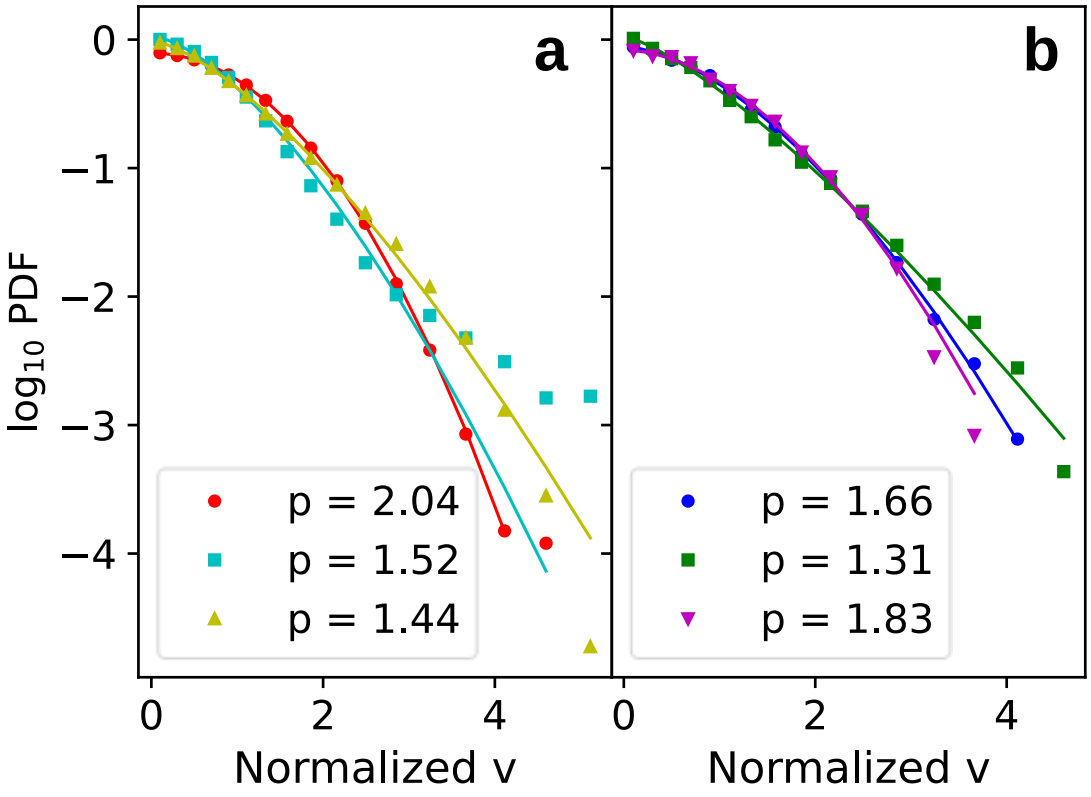

Figure 3.3: Probability density function (PDF) of the x-component of the velocity, $|v_x|$, normalized by $\sqrt{\langle v_x^2 \rangle}$, where the average is over time. (a) The velocity distribution of simulated data. Red circles represent $\alpha = 2$ (Gaussian noise). Green squares represent $\alpha = 1.8$ (Non-Gaussian noise). Yellow triangles represent $\alpha = 2$, but with simulated pixel-locking and SPIFF correction. The solid lines are fits to the form $y = Av^p$ with more weight attached to the left side of the curve (see Sec. 3.3.3, part 4). The fitted value of the exponent p is shown in the inset. (b) 3 different velocity distributions for experimental trajectories and the associated fits with exponent p. All 6 trajectories in the curve undergoes a same low-pass filter with a 4 Hz cutoff.

than simulation time step, $\tau >> \Delta t = 0.02$ s, we used the recursive relation:

$$\begin{aligned} a_0 &= N_0 \\ a_i &= \left(1 - \frac{\Delta t}{\tau}\right) a_{i-1} + \frac{\Delta t}{\tau} N_i. \end{aligned} \tag{3.5}$$

Here N_i is an array of independent and identically-distributed Gaussian random numbers with zero mean and unit variance. The final sequence is adjusted by subtracting the mean from each element in the series, and then normalizing the STD to be σ. During simulation, the equilibrium positions (x_0 and y_0) both drift with the same timescale $\tau \in (12, 800)$ s and potentially different amplitudes $\sigma \in (0, 0.5)$, randomly chosen for each simulation (Eq. 3.5).

As discussed in Sec. 3.2, pixel-locking was an important source of noise in experimental data. Thus, measurement errors were added to the simulated position time series after all the time steps were *completed*. This was intended to simulate errors associated with tracking the particles in the images. To simulate pixel-locking in the position time series, we converted the simulated position to pixels using a length scale l_{pixel} and a random offset $x_{pixel} \in (-0.5, 0.5)$. Then we applied a transformation to the decimal portion, $x_d \in (-0.5, 0.5)$, of the pixel:

$$x_d = \frac{x + x_{pixel}}{l_{pixel}} - \text{round}\left(\frac{x + x_{pixel}}{l_{pixel}}\right), \tag{3.6}$$

$$x_d^* = sgn(x_d) \times \frac{|2x_d|^{p_d}}{2} + N_t(\sigma_d). \tag{3.7}$$

Here x_d^* is the transformed pixel value, p_d is an exponent randomly chosen between $(1, 4)$ for each time series, and N_t is a Gaussian noise with zero mean and STD $\sigma_d \in (0, 0.1)$. The distribution of the decimal part of simulated 'pixels' x_d is plotted in Fig. 3.2b. Finally, as in the experiments, we used the single-pixel interior filling function (SPIFF) algorithm [105] on x_d^* to correct simulated data before training the

Table 3.1: The parameters for 1-particle simulation.

Name	Description	Range	Drift amp.	Drift time
ω	confinement freq.	(1.3,2.5) s^{-1}	None	None
γ	damping coef.	(0.4,1.7) s^{-1}	None	None
δ	asymmetry	(0,0.35)	None	None
θ	weak axis	$(-\pi/2, \pi/2)$	None	None
k_c	vortex force coef.	$(-k_{c,max}, k_{c,max})$ s^{-2}	None	None
α	noise distribution	(1.6,2.0)	None	None
x_0	equi. position	0	(0,0.5)	(12,800) s
y_0	equi. position	0	(0,0.5)	(12,800) s
l_{pixel}	simulated pixel width	(0.3,1)	None	None

model. An example of a simulated trajectory and its x and y components are shown in Fig. 3.2c and 3.2d-e, respectively.

Though pixel-locking was a small source of error, it led to large systematic errors in dynamical quantities such as the 1D velocity distribution. Without further modeling the effects of pixel-locking, these errors can be easily mistaken for stochastic noise with $\alpha < 2$. In a stochastic under-damped harmonic oscillator simulated with $\alpha = 2$ and Gaussian measurement error, the 1D velocity distribution was well-fit by the form $\log P(v_x) = Av_x^p$ with $p = 2$ (Fig. 3.3a, red circles). However, a simulation with either a smaller value of α (green squares), or pixel-locking (yellow triangles) both led to a significantly smaller value of the fitted parameter p. Experimentally, the fitted p was usually smaller than 2 (Fig. 3.3b). It is possible to minimize pixel-locking errors in the velocity distribution function by defocusing the camera [118, 119], however, our 3D imaging and tracking methodology required particles with significant brightness due to the low exposure time. Subsequently, it was not possible to determine whether $\alpha < 2$ or pixel-locking leads to non-Gaussian distributions with our current analysis.

3.3.3 Features for ML

The data used to train the ML model consisted of simulated time series of both the x and y motion of the particle. Typically, each time series contained 15,000 to 100,000 elements, depending on the total length of time of the motion. Although in principle it is possible to use the raw data as input to the ML model, this would drastically increase the computation time. Thus, we choose to extract hundreds of relevant dynamical features of the motion in order to train the model. These ranged from Fourier transforms and autocorrelations, to more sophisticated inference algorithms such as underdamped Langevin inference (ULI) [125].

The confining potential for the particles consists of an asymmetric harmonic trap in x and y, as shown in Fig. 3.2a. We first extracted a rough estimation of the principle axes, defined by θ, for a 2D time series $[x_t, y_t]$, $t = 0, 1, 2, \ldots, T$. T is the length of a single time series, and is the first feature. The total time duration of the series is $T \times \Delta t$, where $\Delta t = 0.02$s. In polar coordinates, $\phi_t = \arctan \frac{y_t}{x_t}$. We used 20 bins to form a histogram of ϕ_t between $(-\pi/2, \pi/2)$ and fit the probability density with

$$p(\phi) = \frac{1 + \delta_{hist} \cos 2(\phi - \theta_{hist})}{\pi}. \tag{3.8}$$

Here δ_{hist} and θ_{hist} are two features.

Let $\langle p_i, q_i \rangle = \Sigma_i^T p_i q_i / T$. The correlation matrix $\mathbf{C}$ was computed:

$$\mathbf{C} = \begin{bmatrix} \langle x, x \rangle & \langle x, y \rangle \\ \langle x, y \rangle & \langle y, y \rangle \end{bmatrix}. \tag{3.9}$$

The eigenvalues of the matrix are $\lambda(1 - \delta_{eig})$ and $\lambda(1 + \delta_{eig})$ and their eigenvectors are $(\cos\theta_{eig}, \sin\theta_{eig})$ and $(-\sin\theta_{eig}, \cos\theta_{eig})$. Here λ, δ_{eig}, and θ_{eig} are three features. After calculating the eigenvectors, (x_t, y_t) are projected onto the (estimated) weaker

and stronger principle axes for further analysis:

$$\begin{aligned} w_t &= x_t \cos\theta_{eig} - y_t \sin\theta_{eig} \\ s_t &= x_t \sin\theta_{eig} + y_t \cos\theta_{eig} \end{aligned} \tag{3.10}$$

w_t and s_t are then normalized into unit STD, and the following feature extraction algorithms are applied to (w_t, s_t):

1. Fourier spectrum. This is the most commonly used tool to analyze the motion of a 1D harmonic oscillator, ξ_t. We compute the Fourier spectrum and only analyzed data between $0.5\ \mathrm{s}^{-1} < \omega < 4\ \mathrm{s}^{-1}$. This is fitted to analytical prediction for a 1D stochastic harmonic oscillator:

$$\omega I(\omega) = A_{FT}\left[\omega^2\left(1 - \frac{\omega_{FT}^2}{\omega^2}\right)^2 + \gamma_{FT}^2\right]^{-1/2} \tag{3.11}$$

   where A, ω_{FT} and γ_{FT} are fitting parameters. Although θ_{eig} is a good estimate of the principal axes, we performed Fourier analysis on a combination of w_t and s_t: $\xi_t = w_t \cos\phi + s_t \sin\phi$. The following pseudocode describes the procedure:

   for $\phi = [-\pi/4,\ 0,\ \pi/4,\ \pi/2]$:
   $\xi_t = w_t \cos\phi + s_t \sin\phi$,
   Conduct 1D Fourier spectrum on ξ_t,
   Fit the spectrum using Eq. 3.11,
   $A_{FT,\phi}$, $\omega_{FT,\phi}$ and $\gamma_{FT,\phi}$ are features.

   Altogether 12 features are extracted using the Fourier spectrum.

2. Autocorrelation is another analysis technique used on 1D time series, ξ_t, and is

defined as:

$$A(\tau) = \sum_{t=0}^{T-\tau} \xi_t \xi_{t+\tau} / (T - \tau). \tag{3.12}$$

$A(\tau)$ was computed for ξ_t and fitted to the analytic form for a 1D stochastic harmonic oscillator:

$$A(\tau) = \left(1 + \frac{\gamma_A^2}{\omega_A^2}\right) e^{-\gamma_A \tau} \cos\left(\omega_A \tau - \arctan\frac{\gamma_A}{\omega_A}\right) \tag{3.13}$$

Similar as Fourier spectrum, the following loop is performed to extract features.

for ϕ in $[-\pi/4,\ 0,\ \pi/4,\ \pi/2]$:

$\xi = w \cos\phi + s \sin\phi$,

Normalize ξ into zero mean and unit variance

Calculate the autocorrelation by Eq. 3.12,

Fit the autocorrelation using Eq. 3.13,

$\omega_{A,\phi}$ and and $\gamma_{A,\phi}$ are features.

Altogether 8 features are extracted using autocorrelation.

3. Percentiles and equipartition law. Let $P(\xi, p)$ indicate the p percentile of a 1D time series ξ_t, the quantity $\zeta = \frac{P(\xi,1)-P(\xi,99)}{P(\xi,30)-P(\xi,70)}$ contains qualitative information about the heavy-tailness of the distribution of the stochastic noise that drives ξ. Furthermore, according to equipartition, the time-averaged kinetic and potential energies should be equal. As a result,

$$\omega_{ep}^2 = \frac{\sum_{t=1}^{T-1} \xi_t'^2}{\sum_{t=1}^{T-1} \xi_t^2} \tag{3.14}$$

is a rough estimation of the eigenfrequency if $\vec{\mathbf{e}}_\xi$ is a principle axis for the confinement, where $\xi_t' = \frac{\xi_{t+1}-\xi_{t-1}}{2\Delta t}$ and $\Delta t = 0.02s$. To extract features, the

following loop is performed.

for ϕ in [$-2\pi/3$, $-\pi/3$, 0, $\pi/3$, $2\pi/3$, $\pi/2$]:

$\xi = w\cos\phi + s\sin\phi$,

Calculate ζ_ϕ and $\omega_{ep,\phi}$ as features.

Altogether 12 features are extracted.

4. Velocity distribution. For a 1D time series ξ_t, the central difference velocity is calculated, ξ'_t. Then we compute the probability distribution $P(\xi'_n)$ of $\xi'_n = |\xi'_t|/\sqrt{\langle \xi'^2_t \rangle}$, as done in Fig. 3.3. Were the noise purely Gaussian ($\alpha = 2$) with no measurement error, then $\log(P(\xi'_n)) \propto -\xi'^2_n$. A more heavy-tailed distribution (see Fig. 3.3) may indicate $\alpha < 2$ or pixel-locking measurement error. Since the distribution is rather complicated, three different fits are performed to extract features. The first is a fit of $\log P$ versus ξ'_n:

$$\log P(\xi'_n) = A_0(\xi'_n)^{p_0}, \tag{3.15}$$

where a fitting weight, $e^{\frac{\log P}{2}}$, is applied to attach more importance to the beginning of the curve. A_0 and p_0 are fitting parameters. The second fit linearly fits the $\log P$ vs. ξ'_n curve with $\xi'_n > 2.5$. The linear coefficient p_1 is recorded. The third fit linearly fits P VS ξ'_n with $\xi'_n > 2.5$. The linear coefficient p_2 is recorded. Note that the second and third fits lack physical meaning, but they provide some qualitative information that helps the ML model give quantitative predictions. The following loop was used:

for ϕ in [$-\pi/12$, $\pi/4$, $7\pi/12$]:

$\xi = w\cos\phi + s\sin\phi$,

Plot the histogram of $P(\xi'_n)$

Fit histograms to get features $p_{0,\phi}$, $p_{1,\phi}$, $p_{2,\phi}$.

Altogether 9 features are extracted.

5. Intermittency analysis. For a 2D time series (w_t, s_t), a scalar velocity is defined as

$$\xi'_t = \frac{\sqrt{(w_{t+1} - w_{t-1})^2 + (s_{t+1} - s_{t-1})^2}}{2\Delta t} \tag{3.16}$$

and its average over time τ is defined as

$$\bar{\xi}'_i(\tau) = \sum_{t=i\tau+1}^{(i+1)\tau} \frac{\xi'_t}{\tau} \tag{3.17}$$

where $i = 0, 1, 2, \ldots, \lfloor \frac{T-1}{\tau} - 1 \rfloor$. We introduced this particular measure because at relatively high values of the vortical force amplitude, k_c, the particle displays intermittent behavior characterized by large orbital excursions from equilibrium, yet below the critical value of $k_{c,max}$. As a result, the ξ' fluctuates at lower frequencies than other time scales in this system. This is characterized by the standard deviation (STD) of $\bar{\xi}'_i(\tau)$ over i. Two features are extracted from the 2D trajectory with $\tau = 500$ and 1300, respectively. The numbers 500 and 1300 are chosen to be much larger than the oscillation timescale (100 Δt) and much smaller than the time length of the trajectories (>10000 Δt)

6. Vorticity estimation. Given a 2D time series (w_t, s_t), the 2D velocity vector $\vec{\mathbf{v}}_t$ is first calculated. Let $v_{mean} = \sqrt{\langle v_t^2 \rangle}$ where $\langle \cdots \rangle$ represents averaging over t. A qualitative estimation of angular velocity is used:

$$\Omega(\tau) = \frac{1}{\Delta t} \left\langle \frac{\vec{\mathbf{v}}_t \times \vec{\mathbf{v}}_{t+\tau}}{v_{mean} \left(\frac{v_t + v_{t+\tau}}{2} \right) \tau} \right\rangle. \tag{3.18}$$

This form puts a larger weight on larger velocities, which is necessary since Ω is completely dominated by noise for small velocities. $\Omega(1)$ and $\Omega(5)$ are two features used in the model.

7. Linear correlation and mutual information. Built-in python packages [126] are used to compute the linear correlation and mutual information between all pairs of time series (w, s), (w, v_w), (w, v_s), (s, v_w), (s, v_s), where v_w (v_s) is the central difference velocity associated with w (s). These measurements are most relevant for large values of k_c, where circular motion can be detected. Altogether this provides 10 features.

8. Underdamped Langevin Inference (ULI) [125]. ULI is a maximum-likelihood algorithm based on modified linear-regression. The time series w, s, v_w, and v_s are used as inputs, along with a linear model of the forces, and the parameters of interest (i.e. ω, γ, etc.) are estimated. There are 8 coefficients in the linear regression, which are 8 features.

9. The previous 8 analyses gives 63 features. Then, a band-pass filter is applied to w_t and s_t with an upper threshold = 2 Hz and a lower threshold = 0.01 Hz. The previous 8 analyses are repeated for 63 more features. This was done to reduce noise in the original data, yet by including analysis on both filtered and unfiltered data, we avoid losing information with little cost of adding features. Counting the 6 features in preprocessing, altogether there are 132 features for the motion of single particles.

3.3.4 ML methods and performance

Two python-based ML algorithms ([a], gradient boosting, which is an ensemble of decision trees, and [b] neural network [126]) were trained on 132 extracted features from 400,000 simulated time series (training data set) to predict the 6 randomly-chosen

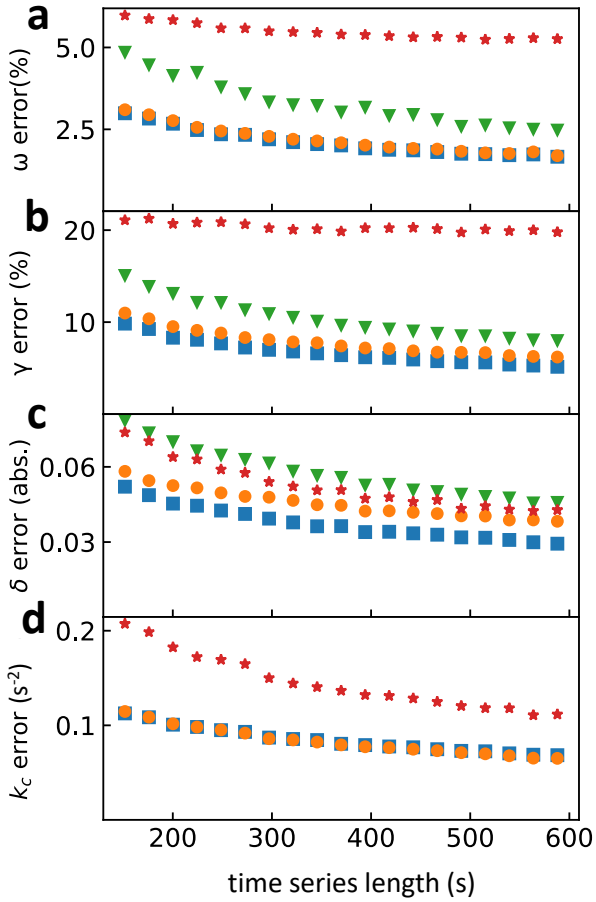

Figure 3.4: The prediction error of various models for multiple parameters on one particle simulated test data. Red stars represent ULI, green triangles represent Fourier spectrum, blue squares represent neural network, and orange circles represent gradient boosting. Note that the Fourier spectrum cannot predict k_c and must be based on a known θ. Since ML is trained on a certain range of all parameters (Table 3.1), unreasonable predictions of Fourier spectrum and ULI are also cropped to that range.

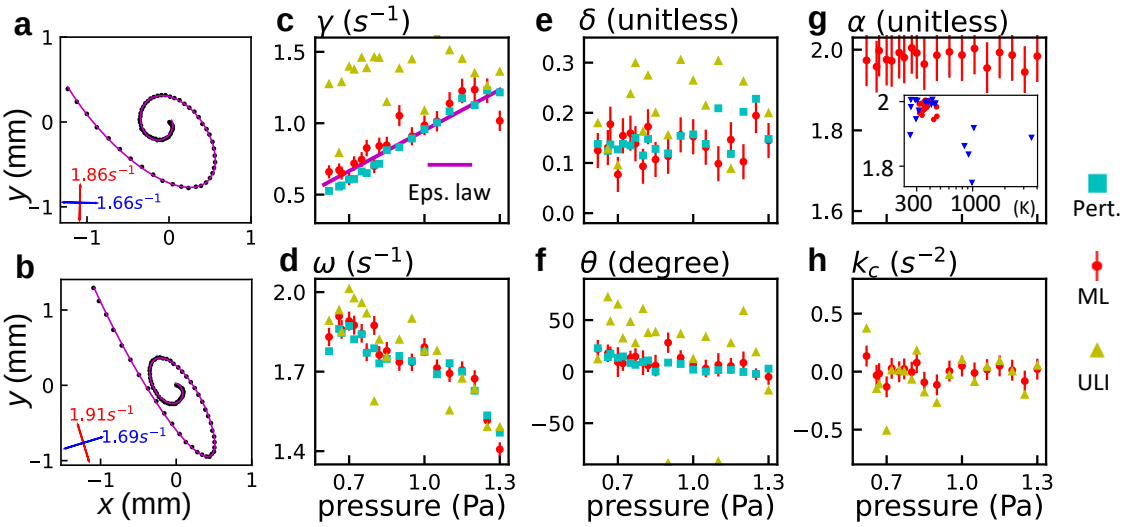

Figure 3.5: (a-b) Two different experiments of the same particle relaxing to equilibrium after a perturbation. The pressure was $P = 0.80$ Pa. The magenta lines are fits using Eqs. 3.21-3.22. The red and blue lines indicate ω_+ and ω_- and their orientations, respectively. (c-f) The prediction from ML (the mean of the predictions from neural network model and gradient boosting model, red circles), ULI (yellow triangles), and reference estimation from the perturbation experiments (Pert., cyan squares) for γ, ω, δ, and θ for particles with diameter 12.8μm. The purple line in (c) represents the theoretical value of Epstein's Law (Eq. 4.2). (g) α and (h) k_c as predicted by ML. These parameters cannot be verified by the perturbation experiments. The inset in (g) shows the prediction of α correlates with the potential temperature of the particle. Red squares represents 12.8 μm particles and blue triangles represent 9.46 μm particles. Error bars were obtained from predictions on the simulated test data set, and errors based on fitting perturbed trajectories are smaller and not shown for clarity.

parameters. Within the algorithms, the gradient boosting model has parameters n_estimators = 250, max_depth = 5, and the dense neural network has 5 hidden layers, with size (128,64,64,32,16) and all hyperbolic tangent activations. Before training, both the features and the targets are normalized by the whole training batch to zero mean and unit variance. The performance of each method was benchmarked on 80,000 simulated time series (test data set). Figure 3.4f shows that ML methods are $\approx 1.5\times$ more accurate at predicting ω and γ than simply fitting analytical expressions to the Fourier spectrum of the data along the principal axes of confinement, and 2-3$\times$ more accurate than ULI [125].

With regard to Underdamped Langevin Inference (ULI), we note that the performance was excellent and comparable to the prediction error for ML *when using only Gaussian noise, no pixel-locking, and no drift.* These sources of noise seemed to dramatically reduce the performance of ULI, yet these sources of noise are unavoidable in real experimental data. However, despite its lack of parameter estimation power on single, noisy data sets, ULI consistently ranked as one of the most important predictive features in the ML algorithms. Employing ULI in the simulated features increased the total simulation and feature extraction time by 150%.

3.3.5 Labeling experimental data

It is challenging to verify the accuracy of results when applying ML models to unlabeled experimental data. However, in our experiments, we measured the parameters using an independent, alternative method. By perturbing the particle with a magnet outside the chamber and observing the particle's relaxation to equilibrium, we fit the 2D trajectory and obtained estimates of ω, γ, δ, and θ. Initially, we used a "mechanical" method to peturb the particle position by moving a grounded metal rod in close proximity to the single, levitated particle. However, this method would sometimes lead to unwanted particles being deposited in the experiment. By using a small,

rare-Earth magnet outside of the vacuum chamber, we found nearly identical results without introducing unwanted particles. The magnet was removed in a fraction of a second, while the particle relaxation process took more than 4 s.

Two examples of particle trajectories during relaxation to equilibrium after a perturbation, and the corresponding best fit, are shown in Fig. 3.5a-b. Assuming $k_c = 0$ and ignoring the stochastic noise term, Eqs. 3.1-3.3 can be solved analytically:

$$w(t) = A_w e^{-\gamma t/2} \cos\left(t\sqrt{\omega_-^2 - \frac{\gamma^2}{4}} + \phi_w\right) \tag{3.19}$$

$$s(t) = A_s e^{-\gamma t/2} \cos\left(t\sqrt{\omega_+^2 - \frac{\gamma^2}{4}} + \phi_s\right) \tag{3.20}$$

$$x(t) = w(t)\cos\theta - s(t)\sin\theta \tag{3.21}$$

$$y(t) = s(t)\cos\theta + w(t)\sin\theta \tag{3.22}$$

Here the fitting parameters A_w, A_s, ϕ_w, and ϕ_s depend on the initial conditions, and γ, ω_-, ω_+, and θ are an estimation of the model parameters as described in Sec. 3.3.1, assuming $k_c = 0$.

3.3.6 Predicting experimental data - Results

We directly compared these measurements with the results from the ML model (the mean of the predictions from neural network and gradient boosting), which measures the parameters *in situ* without perturbations. The difference between the model's predictions and the labels inferred from the aforementioned perturbation method lay within the error bars estimated from the simulated test data in parameters γ, ω, δ and θ. In other words, the model predicts experimental data as accurately as simulated data, so the mismatch between experimental and simulated data was alleviated. In general, ULI was able to predict ω, δ, and θ, yet with an accuracy that was poor compared to ML, which may be expected since ULI does not require training from

multiple datasets.

Both the perturbation method and ML show excellent agreement with the prediction of γ from Epstein's Law (Eq. 4.2). The confinement asymmetry, δ, could be as large as 0.2 although the experimental configuration was quite symmetric and the illuminating laser only contributed to a 1% asymmetry since a gradient in laser intensity is needed to change the confinement strength. Additionally, the gas flow and pumping rate were low and did not affect δ. We speculate that the asymmetry in the confinement may be due to background flows in the plasma environment. ULI produced wildly varying predictions of γ, even sometimes negative values. Thus, we did not include it in Fig. 3.5c.

In analyzing the stochastic noise, we found that the prediction of the Lévy parameter α reflected the particle's effective temperature, $2k_BT \approx m\omega^2(\langle x\rangle^2 + \langle y\rangle^2)$, where k_B is Boltzmann's constant (Fig. 3.5g, inset). We have assumed an equipartition between kinetic and potential energy, and expressed the temperature here in terms of the average potential energy to avoid calculating derivatives for the velocity. Importantly, no information about the temperature was passed to the ML model since all time series were normalized. Reported values of T in dusty plasmas driven by Brownian motion vary from 300-1000 K [127, 128]. For most experiments, we found $T = 300 - 460$ K, with $1.9 < \alpha < 2$, indicating nearly Gaussian noise from the room-temperature neutral collisions (Fig. 3.5g, inset). Larger temperatures typically corresponded to smaller values of α. We speculate that this could be caused by contamination with undetectable, small dust particles since the effective temperature was seen to increase over time in some experiments. Often these particles were "dropped" by shutting off the plasma, and a new particle was deposited in its place. In any case, the source of the higher effective temperatures was non-Gaussian, although we could not definitively identify the origin of the noise.

The non-conservative force from Eq. 3.3 was smaller than the prediction error

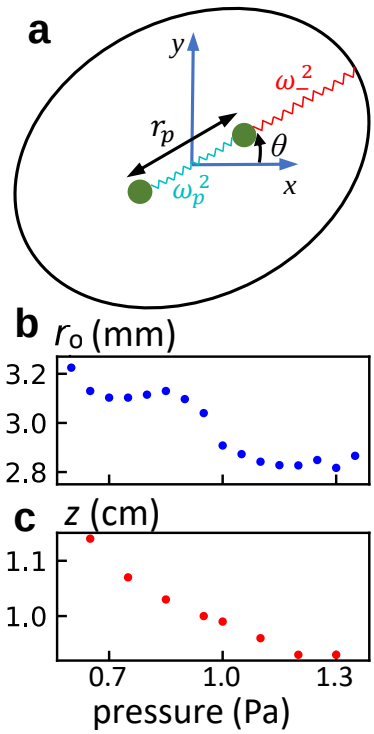

Figure 3.6: (a) Two charged particles experience mutual repulsion, characterized by frequency ω_p at equilibrium, and external harmonic confinement. k_c and ω_+ are omitted for clarity. All susequent panels show parameter estimates as a function of pressure, P. (b-c) The equilibrium particle separation and vertical height above the electrode varied with the gas pressure.

bars for most experiments (Fig. 3.5h). Part of the motivation for including k_c in our linearized model were observations that particles can undergo small elliptical orbits without any apparent input of energy [122]. In Nosenko et al. [122], the gravitational leveling of the electrode played a role, presumably due to a feedback between the plate geometry and the background ion flows. Another possibility would be a non-spherical or broken particle, which could then interact with background ion flows.

3.4 Two particle potion

3.4.1 The linearized model

When two particles are present, their mutual repulsion, $m\vec{\mathbf{f}}_{ij} = mf_p(r)\vec{\mathbf{e}}_{ij}$, displaces them from the center of the confining potential, as shown in Fig. 3.6a. Here, f_p is the reduced force, $\vec{\mathbf{e}}_{ij}$ is a unit vector from particle i to j, r is the particle separation, and m is the mass of a particle. At equilibrium, the particle separation is r_0, which varies with pressure and the vertical position z (Fig. 3.6 b-c). In particular, below P $\approx$ 1 Pa, r_0 sharply increased to a plateau and the height increased, presumably due to an increase in the plasma Debye length. Here we aim to simultaneous infer:

$$\omega_-^2 \frac{r_0}{2} = f_p(r_0), \tag{3.23}$$

$$\omega_p^2 = -\left.\frac{df_p}{dr}\right|_{r=r_0}, \tag{3.24}$$

and all other model parameters from Eqs. 3.1-3.3 with high accuracy using noisy data. We linearize the small-amplitude motion of each particle about their equilibrium position. The equation of motion for particle i is:

$$\ddot{\vec{\mathbf{r}}}_i = -\vec{\nabla}\phi + \vec{\nabla} \times \vec{\mathbf{A}} - \vec{\mathbf{f}}_{ij} - \gamma\dot{\vec{\mathbf{r}}}_i + \vec{\mathbf{N}}(\alpha), \tag{3.25}$$

$$\vec{\mathbf{f}}_{ij} = f_p\vec{\mathbf{e}}_{ij} = \left(-\omega_p^2(r - r_0) + \omega^2(1-\delta)\frac{r_0}{2}\right)\vec{\mathbf{e}}_{ij}. \tag{3.26}$$

The equilibrium force and its differential can be used to solve for 2 independent parameters in a model for f_p. The most commonly used model for f_p assumes a screened, Coulomb interaction (the same as Eq. 1.7):

$$F_D = mf_D = \frac{Q^2}{4\pi\epsilon_0 r}\left(\frac{1}{r} + \frac{1}{\lambda}\right)e^{-r/\lambda}. \tag{3.27}$$

Table 3.2: The parameters for 2-particle simulation.

Name	Description	Range	Drift amp.	Drift time
ω	confinement freq.	(1.3,2.5) s^{-1}	(0,2%)	(12,800) s
ω_p	interaction freq.	(1.7,3.3) s^{-1}	(0,2%)	(12,800) s
γ	damping coef.	(0.4,1.7) s^{-1}	(0,2%)	(12,800) s
δ	asymmetry	(0,0.35)	(0,0.01)	(12,800) s
θ	weak dimension	$(-\pi/2, \pi/2)$	(0,0.1)	(12,800) s
k_c	vortex force coef.	$(-k_{c,max}, k_{c,max})$ s^{-2}	None	None
α	noise distribution	(1.6,2.0)	None	None
c_0	noise scale	(0.005,0.03)	None	None
x_0	equi. position	0	(0,0.02)	(12,800) s
y_0	equi. position	0	(0,0.02)	(12,800) s
r_0	equi. seperation	1	(0,0.02)	(12,800) s
m_1	mass ratio	(0.9,1.1)	None	None
A	2nd order coef.	(-3,10) s^{-1}	None	None
l_{pixel}	simulated pixel width	(0.005,0.02)	None	None

Here ϵ_0 is the permittivity of free space. With this assumption, similar linearized models have been used to directly infer Q and λ from the one-dimensional motion of two particles using Fourier analysis [118, 129–131]. Here we allow for entanglement between motion in two dimensions, and provide estimates of all model parameters. Analogous to the single particle model, parameters γ, ω, δ, θ, k_c, α, and ω_p were randomly chosen to simulate time series using Eqs. 3.25-3.26. The same feature extraction methods as described for a single particle were applied to the center-of-mass and relative coordinates, $(\vec{\mathbf{r}}_1 + \vec{\mathbf{r}}_2)/2$ and $\vec{\mathbf{r}}_1 - \vec{\mathbf{r}}_2$ with some alterations described in Sec. 3.4C. The neural network and gradient boosting models were trained on 227 extracted features from 400,000 simulated time series to predict the 7 parameters, and their performance on simulated test data is shown in Fig. 3.7.

3.4.2 Simulation details

For simulations involving two particles, the drift of the parameters can change the equilibrium separation of the particles, which is comparable to the amplitude of the

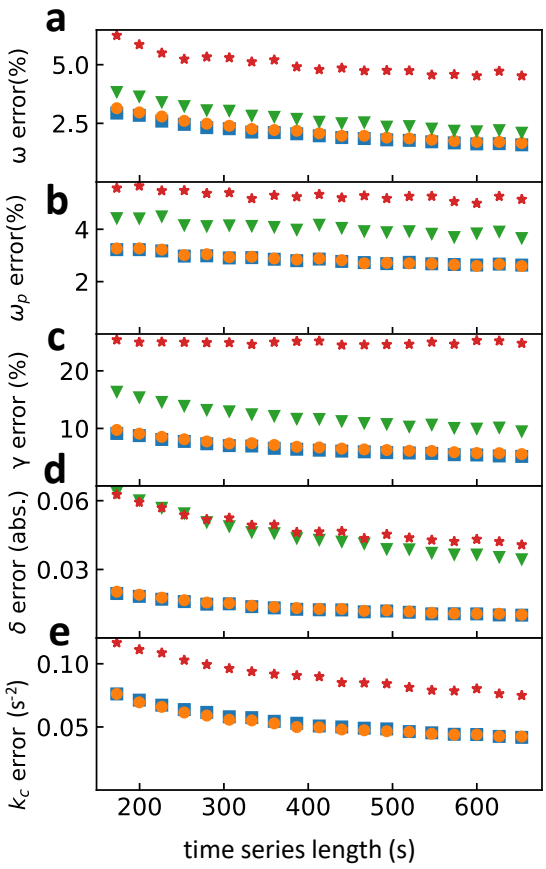

Figure 3.7: The prediction error of various models for multiple parameters on two particle simulated test data. Red stars represent ULI, green triangles represent Fourier spectrum, blue squares represent neural network, and orange circles represent gradient boosting.

Brownian motion. Thus, we allowed for a small drift of many parameters, as listed in Table 3.2. Importantly, the introduction of a repulsive force between the particles leads to a natural length scale, r_0, which is the equilibrium separation between the particles after balancing external confinement and mutual repulsion. In the simulations, r_0 is set to 1, but is allowed to drift. This fixed length scale means we must choose the amplitude of the noise to match what is observed in the experiments. The noise scale, $c = c_0\sqrt{\gamma\omega^2/\Delta t}$, is similar to simulations of for one particle, but here $c_0 \ll r_0$. The value of c_0 is randomly chosen in each simulation, and represents the amplitude of Brownian motion in units of length measured by the particle separation, r_0. Note that c has units of acceleration since mass is normalized and c_0 has units of length.

Furthermore, to make the model more general, a second order term with random coefficient A was added to the reduced particle interaction force,

$$f_p = \left(\frac{A}{r_0}(r - r_0)^2 - \omega_p^2(r - r_0) + \omega^2(1 - \delta)\frac{r_0}{2}\right). \tag{3.28}$$

This is identical to Eq. 3.26, albeit with the addition of the second order term. Note that typically $r - r_0 \approx c_0 \ll 1$, so the second order term is negligible, but was included for generality. Experimentally, the two particles may be slightly different in size, so a mass difference was considered in simulations. We randomly chose the mass of one particle, m_1, to vary by 10% (Table 3.2). As a reminder, none of the parameters have a mass unit, so we can arbitrarily fix the sum of the masses, $m_1 + m_2 = 2$. The acceleration of each particle $\ddot{\vec{\mathbf{r}}}_i$ was calculated as

$$\ddot{\vec{\mathbf{r}}}_i = \vec{\mathbf{f}}_i/m_i \tag{3.29}$$

where $\vec{\mathbf{f}}_i$ is the sum of all the reduced forces exerted on particle i. After each simulation, pixel-locking noise was added to the trajectory of each particle with l_{pixel}, as

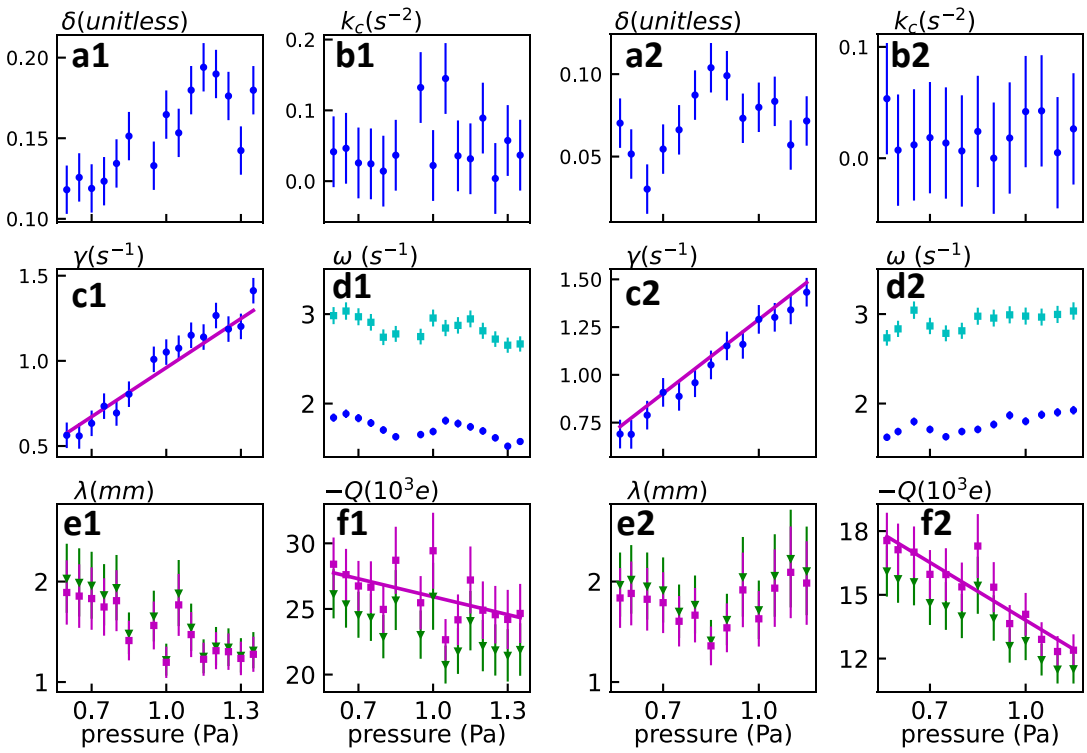

Figure 3.8: ML predictions for the two particle systems. Data is shown for 12.8 μm particles (denoted by 1) and for 9.46 μm particles (denoted by 2). The ML prediction is the average of results from the neural network and gradient boosting methods. (a-c) The predictions of δ, k_c, and γ by ML are represented by blue circles with error bars estimated from Fig. 3.4. The magenta line in (c) is the theoretical γ from Epstein's law. (d) The confinement frequency ω (blue circles) and interaction frequency $\sqrt{2}\omega_p$ (cyan squares) predicted by ML. (e-f) The Debye length λ and particle charge Q calculated from the frequencies using Eqs. 3.27 (green triangles) and 3.30 (magenta squares) from the main text. The magenta line is a linear fit to the magenta squares to guide the eye.

listed in Table 3.2. For all simulations, we used a second order, Velocity Verlet time stepping method to integrate the equations of motion.

3.4.3 Features of two particle motion

For two particle systems, the rough estimation of θ is simply the direction in which the particles align (the weak axis), so we don't perform the preprocessing step. The 4D time series representing the motion of the two particles is projected into the center-of-

mass motion and the relative motion. The same steps 1-9 as Sec. 3.3C applies to the center-of-mass motion (126 features), and similar methods are applied to the relative motion with the following revisions:

1. The fit of the Fourier spectrum only needs 2 projections, parallel and perpendicular to the alignment of the two particles, instead of 4. Furthermore, an additional fit is conducted to the Fourier spectrum of the mode perpendicular to the alignment, where motion predominantly occurs in the azimuthal direction. If the asymmetry $\delta = 0$, this mode would have zero frequency. Thus we used a window $0.1\ \mathrm{s}^{-1} < \omega < 1\ \mathrm{s}^{-1}$, and γ_{FT}, ω_{FT}, but not A_{FT}, are recorded as features. Altogether there are 8 features instead of 12.

2. The same logic applies for autocorrelation, so there are 6 features instead of 8.

3. Percentiles and equipartition analysis are performed to 2 (parallel and perpendicular) projections rather than 6. Altogether 4 features instead of 12.

4. Velocity distribution analysis is performed to 2 projections rather than 3. Altogether 6 features instead of 9

The revised 8 analyses gives 46 features. After the aforementioned smoothing, the analyses are performed again for another 46 features. Moreover, since the trajectory is normalized by the particle separation so that $r_0 = 1$, the STD of each of the 4 modes before and after smoothing are 8 new features. Plus the time series length, altogether we have $63 \times 2 + 46 \times 2 + 8 + 1 = 227$ features for the motion of two particles.

3.4.4 Predicting experimental data - results

Fig. 3.8 shows the ML model prediction on experimental data, for particles with diameters 12.8 μm (label 1) and 9.46 μm (label 2). The prediction of δ is significantly

different between the two sizes of particles, as shown in Fig. 3.8a. This is likely due to their difference in vertical equilibrium position in z (Fig 3.1g). Though k_c seems systemically positive for both particles, its amplitude was usually smaller than the error bar (Fig. 3.8b). We did not specifically train the model on the parameter θ since it is essentially determined by the alignment of the vector $\vec{\mathbf{r_2}} - \vec{\mathbf{r_1}}$. Although a finite value of k_c would lead to an angular displacement away from the weak confinement axis, we found that a numerical value of $k_c = 0.1$ s^{-2} would lead to an small angular displacement of ≈ 0.1 radians.

The damping γ varied linearly with P and was well-described by Epstein's law (Eq. 4.2) for both particles, as illustrated in Fig. 3.8c. The error bars also decreased considerably when compared to the analysis of a single particle (Fig. 3.4 vs. Fig. 3.7). Both ω and ω_p displayed a slight, non-monotonic variation with pressure, outside the range of the error bars in the prediction (Fig. 3.8d). We note that the eigenfrequency for the relative coordinate motion is $\sqrt{\omega_p^2/\mu + \omega_-^2}$, where $\mu = m_1 m_2/(m_1 + m_2)$ is the reduced mass. If the masses of the particles are identical, then $\mu = 1/2$. However, assuming that the particles' mass differ by less than 10%, $\mu = 0.495 \pm 0.005$. Therefore, the coefficient $\sqrt{1/\mu} \approx \sqrt{2}$ is included in Fig. 3.8d for clarity.

For 12.8 μm diameter particles, the "kink" for ω and ω_p lay at the steepest decrease of r_0 in Fig. 3.6. Although these features may be related, we cannot say for sure since the particle height, charge, and Debye length all vary with pressure, and all contribute to ω and ω_p. Additionally, we found that the parameter α could not be well-predicted from the center-of-mass and relative coordinates in the two particle system. Although we are uncertain why the prediction failed for α, we speculate that the distribution in errors from pixel locking are non-additive (unlike the Lévy stable distribution). The motion of the center-of-mass, for example, is the sum of the particle positions. Thus the total noise distribution for the center-of-mass and relative coordinates could be quite different from one-particle system.

Finally, to estimate Q and λ, we used two models for f_p. The first is Eq. 3.27, and the second model is derived from a potential ($mf_w = -d\phi_w/dr$) that incorporates the virtual charge ($\tilde{q}$) from the ion wake beneath each particle [132, 133]:

$$\phi_w = \frac{Q^2}{4\pi\epsilon_0\lambda}\left[\frac{e^{-r/\lambda}}{r/\lambda} - \tilde{q}\frac{\lambda e^{-r_w/\lambda}}{r_w + b\lambda e^{-r_w/\lambda}}\right]. \tag{3.30}$$

Here $r_w = \sqrt{r_0^2 + 0.12\lambda^2}$, $\tilde{q} = 0.3$, and $b = 1$. The parameter b controls the size of the virtual charge cloud. After inferring ω_p and ω_-, the interaction force and it's derivative at $r = r_0$ were numerically solved for Q and λ, following Eqs. 3.23 and 3.24. For both models of the interaction force, the predictions of Q and λ differed by only 10%, as shown in Fig. 3.8e-f, for both sizes of particles. We expect this difference to be much larger if the particles have significant vertical separation, where ion wake interactions lead to non-reciprocal forces [69].

For both particles, Q decreased with pressure. The Debye screening length λ also decreased with pressure for 12.8 μm particles, but there seemed to be a kink in λ for the 9.46 μm particle data at $P \approx 0.75$ Pa. This is likely due to the variation in height with pressure, and a similar feature is also visible in δ (Fig. 3.8a2). It is also important to note that the error in estimating Q and λ can be up to 10$\times$ larger than ω (Fig. 3.8e-f). This can be illustrated by examining Eqs. 3.23, 3.24, and 3.27. These equations can be solved analytically, resulting in the following expression for λ:

$$\lambda = \frac{r_0}{2}\left(\frac{\omega_p^2 + \omega_-^2}{\sqrt{\omega_p^4 - \omega_-^4}} - 1\right). \tag{3.31}$$

When ω_p is close to ω_-, perhaps with overlapping error bars, then the uncertainty in λ diverges. This emphasizes the importance of accurate estimation of all parameters, independent of the model chosen for f_p. Although we allowed for a 10% variation in mass between the particles, this variation was not considered when calculating

Q. The reported values of Q should be taken as an average of the charge on both particles since the mass of each particle may be slightly different.

Finally, we can compare the results shown in Fig. 3.8f to theoretical predictions in our plasma conditions. First, we can estimate the total Debye length in the plasma,

$$\lambda_D = \sqrt{\frac{k_B \epsilon_0 T_e T_i}{e^2 n_p (T_e + T_i)}}, \tag{3.32}$$

where n_p is the quasi-neutral plasma density, T_i is the ion temperature, and e is the elementary charge. As stated previously, $T_e \approx$ 1.3-1.5 eV, and $T_i \approx$ 0.026 eV, so that λ_D is dominated by the ion temperature. For our experimental conditions, the plasma density has been measured previously using a Langmuir probe, and $n_p \approx 2 - 5 \times 10^{13}$ m^{-3} [47]. Thus, we expect $\lambda_D \approx$ 160-260 μm. However, the screening length between particles (λ) is known to be 5-15 times larger than λ_D [134]. Thus, our measurement of 1-2 mm shown in Fig. 3.8e is reasonable and approximately 10$\times$ larger than λ_D. Although λ_D is expected to increase at low pressures since n_p decreases, the exact dependence of the screening length λ on the ion Debye length λ_D is not well understood, especially within a plasma sheath. Subsequently, we do not currently have an explanation for the non-monotonic behavior seen in Fig. 3.8e2.

Second, the particle charge Q can be estimated, to lowest order, by orbital-motion-limited (OML) theory [31, 135, 136]. In its simplest form, we assume that the electron and ion concentrations are equal (quasi-neutrality). The electron velocity distribution is Maxwellian, but the ion drift velocity u_i towards the electrode must be considered in the ion velocity distribution. In this regime, the dust charge is determined by solving the following equation numerically (see section 2.4.3 in [31]):

$$\begin{aligned} 0 = &\sqrt{\frac{T_e m_i}{T_i m_e}} e^{eQ/4\pi\epsilon_0 a k_B T_e} - \\ &\frac{\mathrm{erf}(\xi)\left(2\pi\epsilon a k_B T_i \left(2\xi^2 + 1\right) - qQ\right)}{8\sqrt{\pi}\epsilon a k_B T_i \xi} - \frac{1}{2} e^{-\xi^2}, \end{aligned} \tag{3.33}$$

where erf(ξ) is the error function. The parameter ξ is the ratio of the drift velocity to the ion thermal velocity, $\xi = u_i/v_{i,th}$, where $v_{i,th} = \sqrt{2k_BT_i/m_i}$, m_i is the mass of an argon ion, and m_e is the electron mass. For a simple estimate, we use the Bohm velocity for the ions because the particles levitate near the edge of the plasma sheath, so that $u_i = \sqrt{k_BT_e/m_i}$.

Using the parameters from our experiment, $\xi \approx 5$, and OML theory predicts that the 9.46 μm particles are negatively charged with 16,600-19,200 electrons, and the 12.8 μm particles are negatively charged with 22,500-26,000 electrons (results shown in Fig. 3.8f). Additionally, the dust charge should decrease as pressure increases since ion-neutral collisions become more important as the mean free path decreases ([137], [138], section 2.4.4 in [31]). This expectation is also consistent with Fig. 3.8f. A more quantitative analysis of the pressure dependence of the particle charge is hampered by small but simultaneous variations of electron temperature, drift velocity, and plasma density as the pressure is changed in the experiment. Additionally, alterations to OML theory to include collisions typically ignore ion drift, and both are present in our experiments. Overall, these results highlight the importance of measuring particle charge *in-situ*, as demonstrated here.

3.5 Limitations of this approach

In this chapter, we have overcome two major restrictions when inferring parameters from experimental data with ML: data labeling and mismatch. In our dusty plasma experiments, we label our data by observing particles' relaxation after perturbation. The mismatch between commonly-simulated data (with Gaussian stochastic forces or Gaussian measurement error), and experimental data (with drift, pixel-locking, non-Gaussian stochastic force, etc.) is handled by including these artifacts in our simulation. The agreement between the label for experimental data and our models'

prediction demonstrates the alleviation of this mismatch. Additionally, this work provides simultaneous and accurate estimates of multiple parameters from noisy data, for example, the model provides an accurate in-situ determination of Epstein drag, the particle charge, and the Debye length in dusty plasmas.

Our ML model employed supervised machine learning since stochastic forces and trajectories are an inevitable part of the dynamics. Ideally, the forces in dusty plasmas could be inferred from the experimental data itself, without the need for simulations in the training data set. In dynamical systems with many particles, the interaction force cannot be linearized, yet particle motion is dominated by deterministic forces, and noise is secondary. Therefore, the limitations of this chapter that will be studied in the next chapter would be:

1. This chapter studies the motion of particles around their equilibrium position, whose advantage is the validity of linearizing the forces given the small amplitude of the motion. However, the disadvantage is that only information about the force around their equilibrium position is inferred. To calculate global parameters, for example, Q and λ, a formula (Eq.1.7) must be used, which can be inaccurate. A further study would better infer the force, as a function of arbitrary positions.

2. As mentioned in Sec. 1.2.2, parameters like $Q(z)$ (rather than a fixed Q) should depend on z. However, this method can only study the force at one certain height of the particle, rather than a function of z. A highly dynamic system is required to study this function.

3. The particles are assumed nearly identical in the 2-particle experiment. Thus, at a given z, how the charge and pairwise interaction would depend on particle size (for example, the in-question linearity relationship between Q and U^p that I discussed in Sec. 1.2.1) requires further study.

4. The ML models in this section are trained on simulated data. Is it possible to solely use experimental data?

Chapter 4

Learning generalized force laws in many-particle DP

4.1 Introduction

This work is available on ArXiv [139], and is under review by PNAS.

In Chap. 1, we have discussed the historical and theoretical frameworks that have guided centuries of scientific inquiry into the mechanics of the universe, from the epicycles of the ancient world to the Newtonian physics that underpin much of modern science. The advent of machine learning (ML) has opened new vistas in the study of complex systems, especially many-body systems, that defy easy categorization or prediction using conventional physical laws alone. These systems are not only complex but also dynamic, exhibiting behaviors that traditional physical equations are ill-equipped to predict. Yet, predicting physics from real experiments is challenging.

Endowing ML methods with an inductive bias based on physical intuition can facilitate progress in realistic situations. This is especially important for many-body data, where such intuition is needed to tame the combinatorial complexity of interactions among the measured components [140]. Because of this, physics-constrained

machine learning for many-body systems is still emerging [7, 13, 14, 141–144]. Here, in the context of DP, we simultaneously address many of these challenges by introducing a physics-constrained ML approach based on neural networks as universal approximators, which is able to learn *new*, unanticipated interaction laws from real many-body physical experiments, and be validated on real experimental data.

In a dusty plasma, particle interactions have known approximations based on tractable physics, yet they are poorly understood in environments that deviate from the simplest equilibrium conditions, for example, in systems with background plasma flows [145] or with external magnetic fields [48, 146]. Particles interact through complicated forces mediated by the plasma environment [44], and violate some of our basic expectations: they are non-reciprocal and break the conservation of energy [69, 147–150]. Limited information about these interactions can be obtained by carefully investigating quiescent systems of particles, for example, the Brownian motion of two particles [61, 82, 117] or the vibrational modes in a strongly-coupled crystal [65–68]. Yet particles must be highly dynamic and explore phase space to learn a separation-dependent interaction law [79, 151]. Thus, compact and precise mathematical expressions that summarize interactions among dust particles as physical laws do not exist, yet some constraints on the interactions are clear. For example, the forces between particles are expected to be pairwise *to leading order* and to depend only on their mass, charge, and the spatial configuration [152–155]. Our proposed broadly-applicable approach to infer new, previously unknown interactions from many-body data incorporates these constraints in its underlying neural network architecture to learn the external forces and the unknown particle interactions directly from experimental dusty plasma data.

To infer interaction laws in dusty plasma, we captured three dimensional (3D) trajectories of individual dust particles using scanning laser sheet tomography (See Sec. 2). Our physics-constrained neural network model used this to infer *non-reciprocal*

interactions between individual pairs of non-identical particles, environmental forces that trap particles and drive their motion, and velocity-dependent drag forces from the background gas. Remarkably, the model was extraordinarily accurate in capturing the dynamics of dusty plasma, achieving $R^2 > 0.99$ over multiple experiments. We validated the model using only *unlabeled* experimental data by extracting the mass, m, of each particle in two independent ways, which agreed with each other. Moreover, we fitted the interaction force of each particle pair to the approximation Eq. 1.7, allowing us to estimate the charge, q, of each particle, and the Debye screening length, λ. We find that λ is not solely a property of the plasma environment, and depends on the size of interacting particles, contrary to Sec. 1.2.1. Furthermore, we find that $q \sim m^p$, where p ranges between 0.30 and 0.80 across different experiments and plasma conditions, in contrast to the most widely-used theory of particle charging where $q \propto m^{1/3}$ [31, 156] (Sec. 1.2.1 Spherical capacitor model).

4.2 Experiments and model

Our dusty plasma experiments confined 10-20 spherical melamine-formaldehyde (MF) particles in an RF argon plasma. We purposefully used a combination of manufactured particles (microParticles GmbH) with labeled diameters of 12.8±0.32 μm, 9.46±0.10 μm, and 8.00±0.09 μm since our model is able to handle different particle sizes. The particles were levitated at the edge of the plasma sheath formed above a cylindrical aluminum electrode (diameter = 150 mm, Fig. 4.1A), a setup similar to previous experiments [47, 79, 81, 82]. A unique feature of our experiments was that a cylindrical neodymium magnet with diameter 7.5 cm was placed inside the electrode. The particles levitated ≈ 5 mm above the electrode surface, where the magnetic field strength was ≈ 0.04 T. The gradient in the field produced a vortical ion flow and corresponding ion drag force on each particle. This produced a highly-dynamic system of

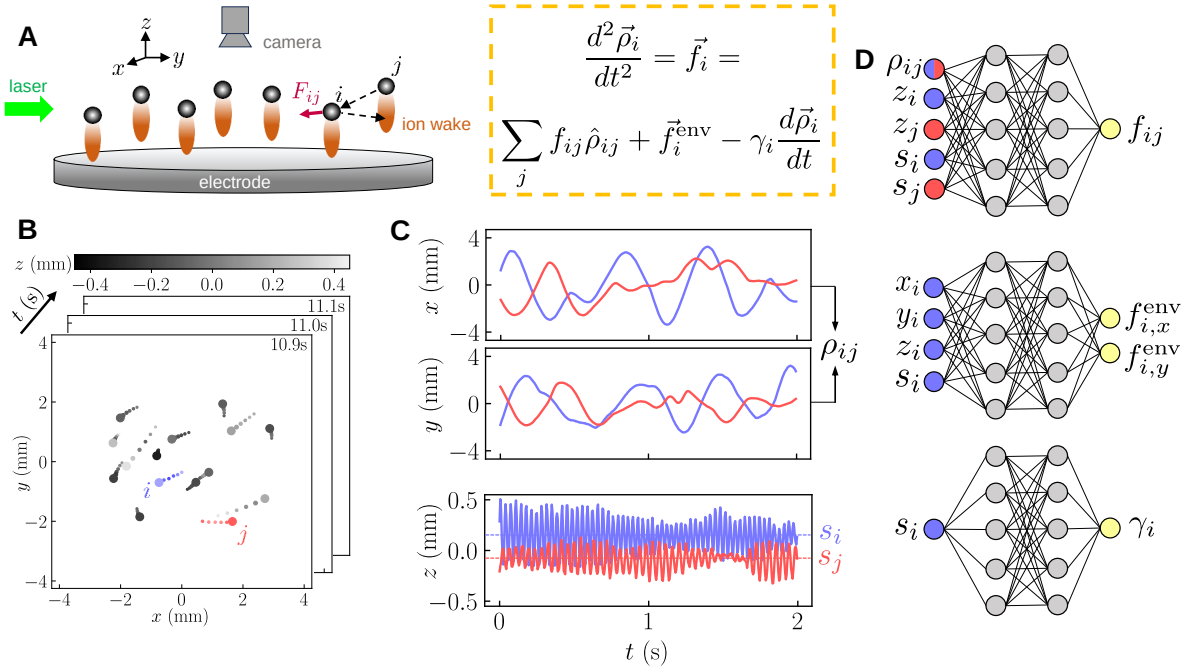

Figure 4.1: Overview of data workflow. (**A**) Particles levitated above the electrode move mostly in the xy-plane, with small deviations above and below the plane. The focused ion wake (red) is directly below each particle, and contributes a small attractive part of the total force (F_{ij}) on particle i. The objective is to infer the horizontal reduced forces on particles using the equation of motion to the right. (**B**) Snapshot of particle positions from a single experiment of 15 particles. The grayscale color indicates the z-position, and the tails of each particle represent the previous 5 frames. (**C**) The x, y, and z position of two particles during two seconds. The particles are marked i (blue) and j (red) in panel (B). The quantity $s_i = \langle z_i \rangle$ is used as a size identifier for each particle. (**D**) The schematic of the model, which consists of three neural networks trained concurrently (particle interaction g_{int}, environmental $\vec{g}_{\mathrm{env}}$, and damping g_γ). The color of the inputs designates the source (particle i or j).

particles with circulation (movie S1 in [139]), where particles were strongly confined to a horizontal plane, and explored a space roughly 10 mm × 10 mm × 1 mm in size (Fig. 4.1A). The particles obtained a negative charge ($\approx 10^4$ e) in the plasma, resulting in a repulsive Coulomb force that was generally non-reciprocal [69, 147–150]. The ions wakes beneath each particle gave rise to non-reciprocal interactions when particles were vertically separated in the z direction, plus a breaking of translational symmetry in z, while maintaining translational symmetry of particle interactions in the xy-plane. Specific details of our dusty plasma experimental setup and the method used for 3D particle tracking are described in prior work [47, 81, 82].

The tracked 3D trajectories, $x_i(t)$, $y_i(t)$, and $z_i(t)$ (Fig. 4.1B), of all the particles were used as input to train our ML model. An example of trajectories for two particles is shown in Fig. 4.1C. The model assumes that the horizontal (xy-plane) acceleration of each particle is determined by Netwon's 2nd law:

$$\ddot{\vec{\rho}}_i = \vec{f}_i = \sum_{j \neq i} f_{ij}\hat{\rho}_{ij} + \vec{f}_i^{\text{env}} - \gamma_i \dot{\vec{\rho}}_i, \tag{4.1}$$

where $\vec{f}_i$ is the horizontal reduced force on particle i, or equivalently the net force, $\vec{F}_i = (F_{i,x}, F_{i,y})$, divided by its mass, m_i. Dotted variables represent differentiation with respect to time. The vectors $\vec{\rho}_i = (x_i, y_i)$ and $\vec{\rho}_{ij} = (x_i - x_j, y_i - y_j) = \rho_{ij}\hat{\rho}_{ij}$ ($\hat{\rho}_{ij}$ is the direction of the reduced horizontal interaction force from particle j to i), and $f_{ij} = F_{ij}/m_i$, where F_{ij} is the magnitude of the force. Since the ion wake is directly below each particle, as shown in Fig. 4.1A, the ion wake will change the direction of the z-component of the force, but interaction forces in the xy-plane will still point along $\hat{\rho}_{ij}$ [69]. The reduced environmental force is $\vec{f}_i^{\text{env}} = \vec{F}_i^{\text{env}}/m_i$, where $\vec{F}_i^{\text{env}}$ is the horizontal environmental force on particle i, and the damping coefficient of particle i is γ_i. Particles are confined by gravity and electrostatic forces in the z-direction, which are about 100 fold larger than other forces in the system, as evidenced by

the different frequencies and amplitudes of motion shown in Fig. 4.1C. This makes determination of vertical forces difficult without higher time resolution, thus we only aim to infer forces in the xy-plane. In general, these forces will depend on the z-position of each particle. Importantly, the particles in our experiments were not identical, thus the model requires particle-level identifiers. Ideally, this would be the mass of each particle, which is unknown. But heavier particles sit lower in the plasma sheath, and we found that a good identifier (s_i) for the size of each particle was simply its mean z-position, averaged over an entire time series: $s_i = \langle z_i \rangle_t$.

In the model, three neural networks (NN) act as universal approximators to the forces on each particle (Fig. 4.1D). They have separate inputs and are trained in parallel. The first NN, g_{int}, requires ρ_{ij}, z_i, z_j, s_i, and s_j as inputs. It outputs the magnitude of the effective reduced interaction force, f_{ij}. We note that this structure conserves translational symmetry in x and y, but breaks this symmetry in z. The second NN, $\vec{g}_{\text{env}}$, requires x_i, y_i, z_i, s_i as inputs. It outputs $\vec{f}_i^{\text{env}}$. The third NN, g_γ, uses s_i as its sole input, and outputs γ_i. Requiring a drag force linear in velocity is supported by theory: according to Epstein's law [124], for spherical MF particles with a density of 1,510 kg·m^{-3} inside argon gas [44],

$$\gamma_i = \frac{12.2P}{d_i} \mu\text{m} \cdot \text{Pa}^{-1} \cdot \text{s}^{-1}. \tag{4.2}$$

Here P is the plasma pressure and d_i is the diameter of particle i. Inferring an individual particle's damping coefficient provides direct information about its size (and mass), thus g_γ constructs a map from the size identifier s_i to the physical parameter γ_i (or m_i). During training, the model adjusts the weights in each neural network concurrently to minimize a loss function that compares the predicted reduced force, $\vec{f}_i$, to the measured horizontal acceleration, $\ddot{\vec{\rho}}_i$. To prevent excessive noise when calculating time derivatives of experimental data, we use the weak form in our loss function [157].

Since we are calculating the forces between all pairs of particles, the total training time scales as N_p^2. The complete details of the model structure, minimization of the loss function, and the application of the weak form are described in chap. 4.6.1

4.3 Model prediction results

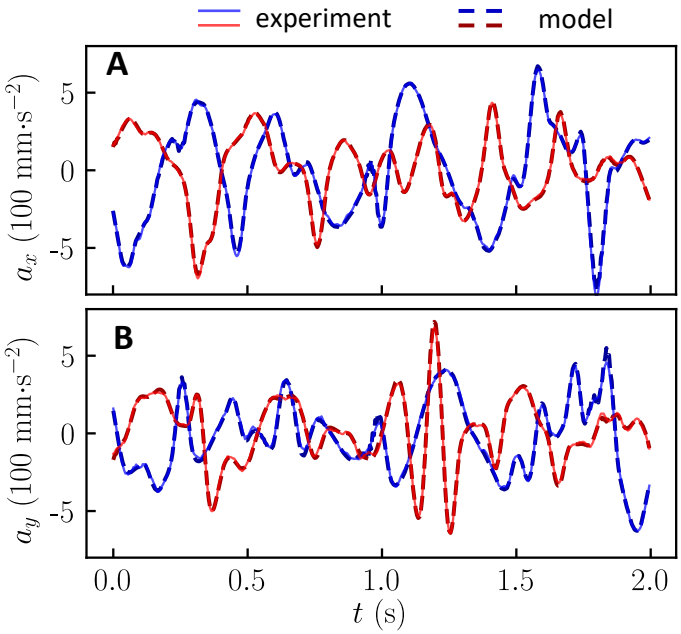

Figure 4.2: The predicted reduced force ($\vec{f}$, dashed lines) and measured experimental acceleration ($\ddot{\vec{\rho}}$, solid lines) for 2 particles (red and blue) in the 15 particle system. Data is shown for 2 s out of the 4.94 s of test data. The entire experiment was 49.4 s long. (**A**) f_x and $\ddot{\rho}_x$, and (**B**) f_y and $\ddot{\rho}_y$. The two particles are the same particles shown in Fig. 4.1C.

We used the model to infer forces on particles from 5 experiments (movies S1-S5 in [139]) carried out under different conditions: number of particles, gas pressure, and plasma conditions. At least $\sim$ 9 particles were necessary to produce a highly dynamic system; smaller systems with less particles tended to form rotating crystalline structures (see Movies S6-S7 in [139]). For each experiment, ten-fold cross-validation was used to compute a validation R^2 score, which was always larger than 0.99 (Table 4.1). For visual reference of the model performance, we show data for the x and

N_p	P (Pa)	z_{std} (mm)	ρ_{std} (mm)	Test R^2	color
9	1.00	0.060	0.96	0.9949	blue
10	1.00	0.10	1.23	0.9921	green
13	1.00	0.082	1.14	0.9912	red
15	0.75	0.12	2.24	0.9919	orange
18	1.20	0.033	1.38	0.9963	purple

Table 4.1: Parameters and model performance from 5 experiments. N_p is the number of particles, P is the neutral gas pressure, z_{std} and ρ_{std} are the standard deviation of the particle motion in the vertical and horizontal directions, respectively, and are averaged over all particles. Test R^2 is the R^2 score of the model performance on the test data set. Each experiment is assigned a color, indicated by the last column, which is plotted in Fig. 4.4.

y acceleration on two different particles and the corresponding model prediction in Fig. 4.2A-B. This remarkable agreement is representative of all 49.4 s of data captured in the experiment. We note that a high R^2 only indicates that the model fits the *sum* of the three reduced force components in Eq. 4.1, and does not necessarily indicate that *each* component is fit correctly. Thus, we ensured that the set of input parameters for each component was parsimonious and contained minimal overlap, i.e., x_i and y_i appear directly as inputs to $\vec{g}_{\text{env}}$, but only appear in the particle separation ρ_{ij} for g_{int}. Furthermore, as we will show, the accuracy of each component is validated by inferring particle-level properties in two independent ways.

Recent examples using graphical neural networks show that effective *local* interaction forces can be learned from experimental data by assuming all particles are identical, and computing the average force [13]. Underdamped Langevin inference (ULI) can also extract complex interactions between identical particles [125]. In contrast to these examples, our model predicts the effective reduced interaction force, f_{ij}, which can be non-reciprocal, between *any* particle pair i and j at *any* position represented in the experimental data. We are not aware of any other force inference technique that is capable of treating particles as individuals. For simplicity, since $\rho_{ij} = \rho_{ji}$, we use ρ to denote the horizontal separation of two particles. Figure 4.3A demonstrates the model's ability to capture non-reciprocal interactions for

two nearly identical particles with identifiers $s_1 \approx s_2$ at different vertical positions, $z_1 < z_2$. Non-reciprocity is clearly observed for $\rho < 0.6$ mm, and $f_{21}/f_{12} \approx 2$ at the shortest separation. For the same particles with a larger vertical separation, f_{12} is attractive (Fig. 4.3A inset). The dramatic non-reciprocity is due to the presence of an ion wake structure beneath each particle (the deviation of an ion's linear drift towards the electrode due to a particle's charge) [158]. However, interactions are expected to be reciprocal when $z_i = z_j$ [69]. This reciprocity is illustrated in Fig. 4.3B for the same two particles (the main panel) and two different particles (inset).

In this reciprocal regime, we used the well-known screened Coulomb interaction to fit the prediction of the model:

$$m_i f_{ij} = m_j f_{ji} = \frac{A}{\rho}\left(\frac{1}{\rho} + \frac{1}{\lambda}\right) e^{-\rho/\lambda}. \tag{4.3}$$

Here the coefficient A is a fitting parameter, but theory suggests that $A = q_i q_j / 4\pi\epsilon_0$, where q_k and m_k are the charge and mass of particle k, respectively, ϵ_0 is the permittivity of free space, and λ is the effective screening length [31, 44, 151]. Importantly, systematic error can be clearly observed in the fit (solid lines in Fig. 4.3B), indicating that there are deviations from Eq. 4.3 as a universal law for all particle separations. This deviation is expected since the real interaction involves both negatively-charged particles and their associated ion wake structures. These structures are often modeled as a virtual, positive charge below each particle [133]. Nevertheless, Eq. 4.3 is a good analytical approximation for each pair of particles when they are at the same z, although as we will show, care must be taken when interpreting both q and λ from the fits to Eq. 4.3. When $z_i = z_j$, but $s_i \neq s_j$, as shown in the inset of Fig. 4.3B for different particles with indices 1 and 3, the reduced force can be shifted to coincide using a multiplicative factor of 2.6. This factor is the particles' mass ratio, m_3/m_1, when the forces are reciprocal ($F_{13} = F_{31}$).

In addition to the dependence on ρ, the model can predict the dependence of the interaction force on z, revealing the spatial structure of the plasma sheath. Figure 3C shows the reciprocal reduced force versus z for particles 1 and 2 when $z_1 = z_2 = z$. At larger z, the force is nearly uniform, but then rises precipitously as z decreases, more than a factor of two over a span of 200 μm. This sharp rise is mostly due to the variation of accumulated charge on each particle. In the bulk plasma, properties such as the ion and electron temperature and density are expected to be constant [43, 49]. Thus, the particle charge should also be constant. However, inside the plasma sheath, these properties change, and the charge on the particles can increase dramatically [47, 52]. This is also evidenced by an increase of the screening length (λ) at the boundary of the plasma sheath (Fig. 4.6). Additionally, we show the model's prediction of the reduced environmental force ($\vec{f}_i^{\text{env}}$) in Fig. 3D. This force acts on each particle separately, and is due to local electric fields and ion drag forces that trap the particle and drive its vortical motion. Taken together, Fig. 4.3 shows how our ML model can turn the particles into non-intrusive, local probes of the plasma environment.

4.4 Inference of plasma and particle properties

In many-body systems, measured properties of individual particles are often inaccessible or assumed from simple theories, yet our ML approach can infer both the mass and charge of each particle from experimental data alone. Using nonlinear regression, we simultaneously fitted the model's predicted interaction (e.g., Fig. 4.3B) to Eq. 4.3 for every pair of particles in each experiment at $z = 0.03$ mm, with fitting parameters m_i, q_i, q_j, and λ_{ij}. Note that here q_i is used rather than Q in previous chapters, to highlight that charge in this chapter would vary since we use various particles. To obtain good fits, it was necessary to allow the screening length (λ_{ij}) to vary between

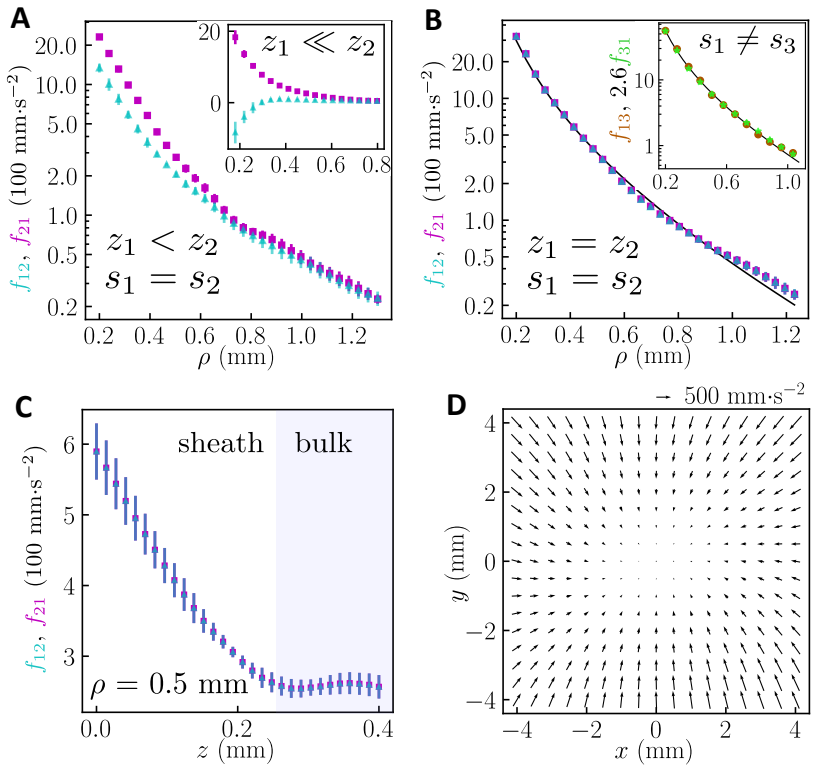

Figure 4.3: Model prediction of interaction and environmental reduced forces for the 15-particle experiment. (**A**) The magnitude of the reduced interaction force (f_{12}, cyan triangles; f_{21}, purple squares) between two similar particles ($s_1 = 0.234$ mm, $s_2 = 0.232$ mm), at $z_1 = 0.15$ mm and $z_2 = 0.30$ mm. The force is plotted versus the horizontal separation ρ. The inset shows the interaction at $z_1 = 0.05$ mm and $z_2 = 0.35$ mm. (**B**) The model predicts the same two particles' interaction is reciprocal at $z_1 = z_2 = 0.15$ mm. The black solid line is a fit of the average of the two predictions to Eq. 4.3 with $\lambda = 0.42$ mm. The inset shows the interaction of two different particles (f_{13}, brown circles; f_{31}, green stars) at $z_1 = z_3 = 0.15$ mm. Here $s_3 = -0.053$ mm, and f_{31} is shifted by a factor of 2.6 (the mass ratio) to collapse the curves. The black solid line is a fit to Eq. 4.3 with $\lambda = 0.48$ mm. (**C**) f_{12} and f_{21} evaluated at $\rho = 0.5$, plotted versus $z = z_1 = z_2$. The sharp rise in the model prediction indicates the boundary between the plasma sheath and bulk plasma (purple). (**D**) Environmental reduced force field of particle 1, $\vec{f}_1^{\,\mathrm{env}}$, at $z_1 = 0.15$ mm. The error bars represent the standard deviation of the prediction from 10 models trained on different sections of the experimental data, as detailed in chap. 4.6.2 (**SM**).

particle pairs, rather than be represented by a single constant that only depends on the plasma environment as theory suggests [31] (See Sec. 1.2.1). This is evidenced in Fig. 4.4A, where f_{ij} is plotted for a pair of small particles, and a pair of large particles. The Debye length varies by almost a factor of 3. This surprising result suggests that in plasma sheaths, and potentially in weak magnetic fields, particle size can affect ion and electron screening in new, unexpected ways. In addition to the mass inferred from the interaction, $m_{i,\mathrm{int}}$, we obtained an independent estimate of the mass, $m_{i,\gamma}$, from the inferred damping coefficient, γ_i, by computing the particle's diameter using Eq. 4.2, and the mass was calculated assuming the particles were spheres. The two independent masses inferred from parallel-trained NNs show excellent agreement (Fig. 4.4B), demonstrating that the model correctly infers each term in Eq. 4.1 using experimental data.

The inference of the particle charge reveals discrepancies from widely-used theoretical assumptions. Orbital-motion-limited (OML) theory predicts the charge on a spherical particle in a dusty plasma if the electron and ion temperatures (and densities) are known (Sec. 1.2.1). These properties vary most strongly with z in the plasma sheath, so at the same z-position, theory suggests that two particles of different sizes *should* act as spherical capacitors and have the same floating potential, $V_i = 2\pi\epsilon_0 d_i q_i$. Thus, we expect $q_i \propto m_i^{1/3}$ since $m_i \propto d_i^3$. We tested this relationship by fitting the inferred charge versus mass in all 5 experiments using $q_i \propto m_i^p$. As shown in Fig. 4.4C, the power p ranged from 0.30-0.80. This result is unexpected since our experiments lie in the regime where OML theory should be the most accurate, i.e., for small particles ($d \ll \lambda$) and low collisionality (low pressure and density) [159]. Thus, even when the particle charge is inferred at the same z-position, where plasma properties should be the same for all particles, the power p can vary substantially from the expected value of 1/3. Moreover, the power p increased monotonically with pressure P (Fig. 4.4 inset), indicating that the plasma sheath environment and par-

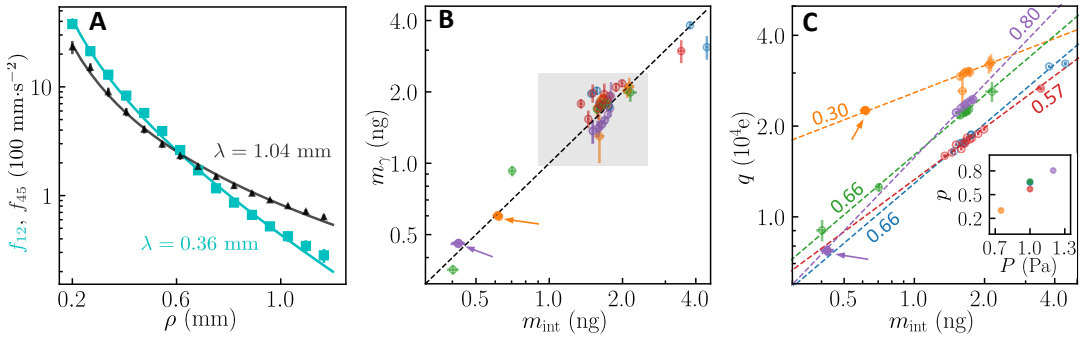

Figure 4.4: The inferred measurements of mass, charge, and Debye length using Eq. 4.3, at $z = 0.03$ mm. (**A**) In the 15-particle experiment, the interaction between small particles 1 and 2 ($s_1 = 0.234$ mm, $s_2 = 0.232$ mm, cyan) and between large particles 4 and 5 ($s_4 = -0.150$ mm, $s_5 = -0.161$ mm, gray) have a distinctly different decay with length scale λ. The solid lines are fits using Eq. 4.3. Note that a larger λ means slower decay. (**B**) The mass of all particles inferred from the drag coefficient (m_γ) versus the mass inferred from the particle interaction ($m_{\rm int}$). Different colors represent the 5 different experiments (Table 1). The dashed line is the theoretical value of $m_\gamma = m_{\rm int}$. The gray box represents particles with an average diameter of 12.8 ± 0.32 μm, corresponding to a mass of $m_0 = 1.65 \pm 0.12$ ng, which is necessary for quantifying the mass. (**C**) Particles charge, q, versus $m_{\rm int}$, both inferred from the fitting procedure using Eq. 4.3. The dashed lines are power law fits with the fitting power p displayed alongside the lines. In both panels, the two clusters of purple and orange data (indicated by the arrows) each consist of 5 similar particles whose manufacturer-labeled diameters are 9.46 ± 0.10 μm (0.66 ± 0.02 ng) and 8.00 ± 0.09 μm (0.40 ± 0.01 ng), respectively. Inset: the fitting power p versus the plasma pressure P. Note that the blue and green data coincide.

ticle charging mechanism change substantially with pressure, although more data is needed to determine this relationship. Furthermore, to ensure that our results are not an artifact of the inference process and accurately represent the physics, we simulated systems of many particles with similar non-reciprocal forces and environmental forces as in the experiment, and required that $q_i \propto m_i^{1/3}$ (see appendix 4.6.4). The model achieved a validation $R^2 = 0.9989$ and demonstrated remarkable performance when extracting the mass and charge of each particle (Fig. 4.7A-B), suggesting that the inferred deviations from the accepted theory in experimental data are real.

While our model only fits the horizontal acceleration due to the limit of the laser scanning frequency, the particle's vertical motion also contains useful information, which can be analyzed with the aid of our model. First, the (radial) eigenfrequency of vertical motion for particle i, $\omega_{z,i}$, can be easily obtained by fitting the Fourier spectrum with Eq. 3.11 (Fig. 4.5A). We can repeat the same step as above at different z to obtain *each* particle's charge q_i as a function of z. Rather than fitting all particles' interactions, at a given z, particle i is used in the fit if and only if it explores this z in the experiment, or more rigidly, z is within the 5% to 95% percentile of $z_i(t)$. The selection of particles may cause a $< 5\%$ systematic error in the fitted charge, as shown in Fig. 4.5B at around $z = 0.00$ mm. Each particle's equilibrium change $q_i(z)$ decreases as a function of z, as plotted in Fig. 4.5a. A flattening of the decrease is observed at $z = 0.26$ mm, which indicates a flattening of particles' charge. As theory suggests [31], the particles' charge sharply increases in the plasma sheath and is uniform in the bulk plasma. $z = 0.26$ mm can be viewed as the boundary of the plasma sheath in our experimental setup.

The vertical electric field E_z can further be calculated at the equilibrium z of each particle i, s_i. All the differential with respect to z are noted prime ($'$) in this paragraph. In the z-direction, the dominating forces are gravity and electrostatic

force $E_z(z)q_i(z)$ which is a function of z, which balances each other at $z = s_i$:

$$m_i g = E_z(s_i)q_i(s_i) \tag{4.4}$$

We linearized this restoring force as a harmonic oscillator. So, $\omega_{z,i}$ should depend on the 'steepness' of the restoring forces at their equilibrium position, $z = s_i$:

$$m_i\omega_{z,i}^2 = (E_z q_i)'(s_i) = E_z'(s_i)q_i(s_i) + E_z(s_i)q_i'(s_i) \tag{4.5}$$

With known $m_i, q_i(z)$ thus known $q_i'(z)$, we can calculate $E_z(s_i)$ and $E_z'(s_i)$ by solving Eq. 4.4-4.5 for each i, which is shown in Fig. 4.5C. The electric field decays sharply near the boundary of plasma sheath.

The gradient E_z' intrinsically links the points, which implies that the model captures the underlying physical relationship between the electric field and its spatial variation without explicitly being fed this information. This would generally be considered strong evidence that the model has learned a genuine physical law or pattern that reflects the real-world behavior of the system its modeling, rather than merely being able to predict a future state. The ability of the model to accurately predict the linkage between E_z and E_z' at various z positions demonstrates its robustness and hints at the possibility of leveraging such models to infer other plasma characteristics. An accurate measurement of plasma properties may have profound implications for controlled fusion research, space physics, and industrial applications where plasma behavior plays a critical role.

4.5 Conclusion

We have developed a machine learning model that accurately infers the forces acting on individual particles in a many-body system. What makes this model different

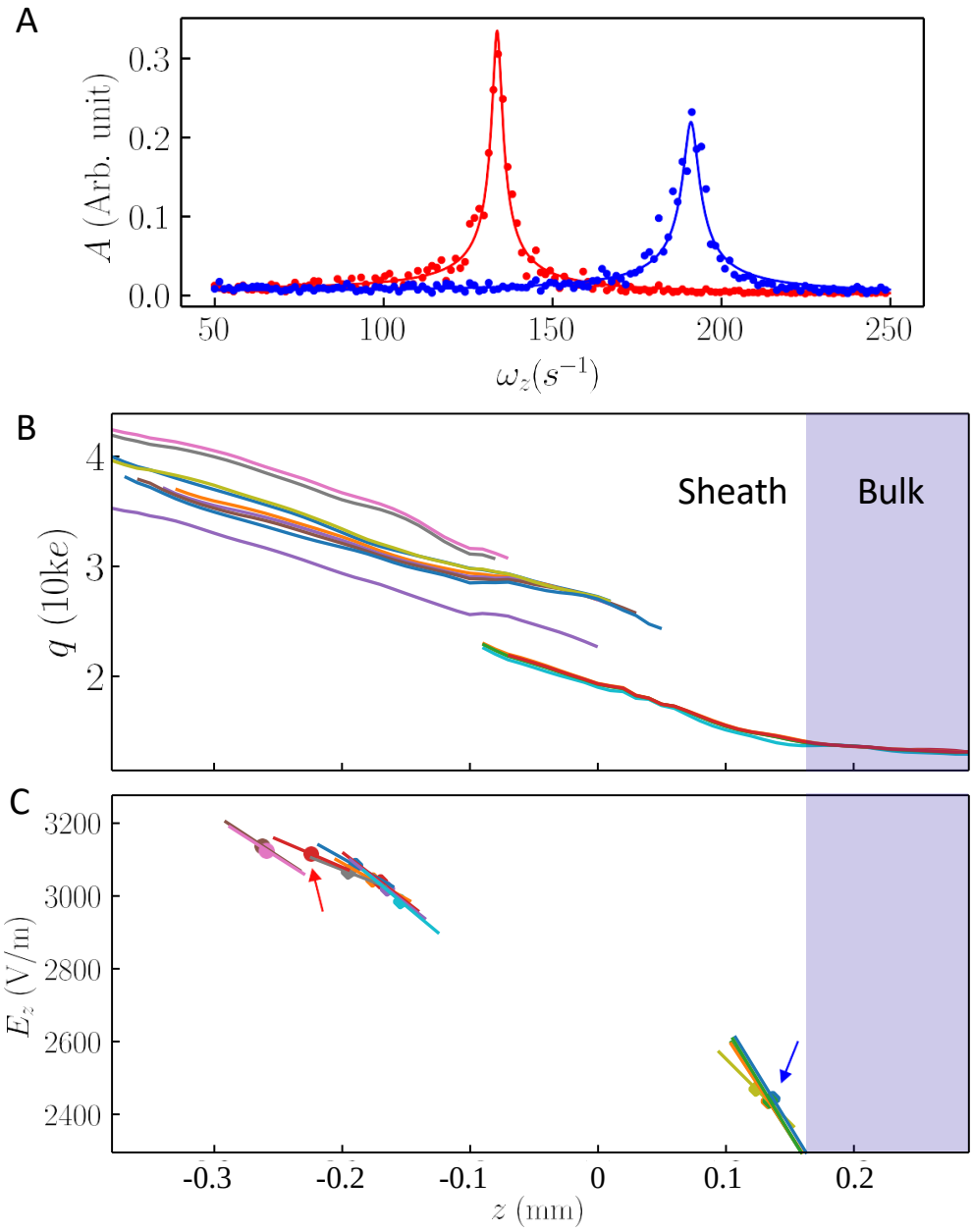

Figure 4.5: (A) The Fourier spectrum amplitude (A) of the blue and red particles in Fig. 4.1. The fit is conducted with Equation. 3.11. (B) Variation of the predicted charge q (in units of 10^4e) as a function of the vertical position z (in mm) for individual particles within the plasma. Each curve corresponds to a different particle, and the flattening of the curve at $z = 0.26$ mm indicates the boundary between the plasma sheath and bulk plasma (purple). (C) Simultaneous prediction of the electric field E_z and its gradient E_z' at the equilibrium positions of the particles, with circles denoting E_z values and connected lines indicating E_z'. The model's accuracy in linking these values without prior knowledge emphasizes its proficiency in encapsulating the physical dynamics governing the system. The arrows point to the blue and red particles in panel A.

from past approaches is its ability to approximate complex, nonlinear interaction laws using NNs, to effortlessly scale with the number of particles and build in physical symmetries into the model structure, and to learn purely from experimental data. Furthermore, the model's ability to know the *physics* is validated exclusively on experimental data, by 1) self-consistently predicting the mass of the particles in two separate ways, and 2) self-consistently predicting the vertical electric field and its differential at the equilibrium positions of each particle. By applying this new approach to dusty plasmas, we learned both environmental forces and pairwise interaction forces between particles, extracted the mass and charge of each particle, and the electric field *in situ*. In doing so, we discovered unexpected scaling laws between the charge and mass of each particle and a variation in the Debye screening length between particle pairs, suggesting that charging mechanisms in the plasma sheath are more complex than widely-used theories often assume. We expect these results to serve as seeds for new directions of research in dusty plasma physics. Outside of dusty plasma research, our ML approach is widely applicable to physical and biological systems composed of many interacting agents. They can be active or passive, with arbitrarily complex interactions. Although intuition guides the underlying symmetries and expected structure of the model, the ability to surpass intuition and avoid biased assumptions is an essential first step in discovering new scientific laws from experiments.

4.6 Appendix for Chap. 4

4.6.1 Model details

Our model is implemented in TensorFlow [160]. In this section, all the bold text are functions in TensorFlow, with input parameters in the bracket after the function, if necessary. If parameter values are not mentioned, they are assumed to be the default. As described before, the model consists of 3 neural networks (NNs) trained in parallel: $g_{\text{int}}, \vec{g}_{\text{env}}$, and g_γ. Both g_{int} and $\vec{g}_{\text{env}}$ have 3 dense-connected hidden layers, with **he_normal** initialization and **L2** regularization. The network g_{int} has 32 neurons for each hidden layer with **leakyrelu** (alpha = 0.1), **tanh**, and **leakyrelu** (alpha = 0.1) as activation functions, respectively. These parameters are not strictly investigated, because varying them only leads to a small change in the R^2 ($\approx$0.001). As for the choice of these parameters, 3 hidden layers is a typical choice for standard NNs, which I did not tune. I tried 64 neurons per layer first, and then 32 neurons for a speed boost, and discovered that 32 neurons perform as well as 64, so the decision is settled on 32. As for the choice of activation function, **leakyrelu**, due to its simplicity, is about 20% faster than **tanh**. However, after some training, I found having one **tanh** among the 3 layers results in a slight improvement, probably because the better non-linearity that **tanh** provides. Finally, the last layer must be **leakyrelu** to ensure that the output would not saturate to 1, the maxima of **tanh**. The last hidden layer is fully connected to a single output, the magnitude of the reduced interaction force in the xy plane, multiplied by horizontal separation, $f_{ij}\rho_{ij}$. The multiplication of the force by ρ_{ij} serves two purposes. The first is to lessen the divergence of the output as $\rho_{ij} \to 0$. The second is to save considerable computing time by not calculating a square root for every interaction force vector, which is calculated for each particle interaction pair:

$$\vec{f}_{ij} = f_{ij}\hat{\rho}_{ij} = \frac{f_{ij}\rho_{ij}\vec{\rho}_{ij}}{\rho_{ij}^2}. \tag{4.6}$$

The network $\vec{g}_{\text{env}}$ has 16 neurons for each hidden layer with **elu**, **tanh**, and **elu** as activation functions, respectively. The last hidden layer is fully connected to two outputs, $f_{i,x}^{\text{env}}$ and $f_{i,y}^{\text{env}}$. Finally, the network g_γ has 2 hidden layers with 16 neurons each, and **elu** and **tanh** as activation functions, respectively. The last hidden layer is fully connected to a single output: the damping coefficient, γ_i. Note that the activations were intended to be **relu**, and initially **elu** was a typo. However, The typo was discovered after several models were trained and saved, and I then investigated that **elu** performs as well as **relu**. For consistency, I used **elu** for the remaining models. As described before, our model fits the reduced net force, $\sum_j \vec{f}_{ij} + \vec{f}_i^{\text{env}} - \gamma_i \dot{\vec{\rho}}_i$, to each particle's experimental acceleration, $\ddot{\vec{\rho}}_i$.

To reduce the amplification of measurement error by temporal differentiation, we apply the weak form [157] in our loss function:

$$L = \frac{1}{2N_p T_{\text{train}}} \sum_{i=0}^{(N_p-1)} \sum_{t\in\mathbb{T}_{\text{train}}} \sum_{\alpha}^{\{x,y\}} L_{i,t,\alpha}, \tag{4.7}$$

$$L_{i,t,\alpha} = H\left(w \circledast_t (\vec{f}_i^{\text{env}} + \sum_j \vec{f}_{ij} - \gamma_i \dot{\vec{\rho}}_i - \ddot{\vec{\rho}}_i)_\alpha ; \delta \right) \tag{4.8}$$

Here T_{train} is the total number of frames for the particle trajectories in the training dataset, $\mathbb{T}_{\text{train}}$, and w is a customized weight function, defined in the range $[-\tau\Delta/2, \tau\Delta/2]$:

$$w_{t'} = w(t'\Delta) = \frac{30}{(\tau\Delta)^5}\left((t'\Delta)^2 - (\tau\Delta/2)^2\right)^2, \tag{4.9}$$

where the recording time step $\Delta = 0.005$ s, and $\tau = 16$ is the size of the convolution window. The function H is a Huber loss function that reduces the relative weight of outliers in the loss function. The parameter δ controls the threshold of this reduction.

The convolution function $\circledast_t$ is defined as:

$$a \circledast_t b = \int_{-\tau/2}^{\tau/2} a(t'\Delta) b(t'\Delta + t\Delta)\, dt' = \Delta \sum_{t'=-\tau/2}^{\tau/2} S_{t'} a_{t'} b_{t+t'}. \tag{4.10}$$

In the last step of the equation above, Simpson discretization is used to compute the integral over each window, with the coefficient:

$$S_{t'} = \begin{cases} 1/3, & \text{if } |t'| = \tau \\ 4/3, & \text{if } |t'| < \tau \text{ and } (t'+\tau) \text{ is odd} \\ 2/3, & \text{if } |t'| < \tau \text{ and } (t'+\tau) \text{ is even} \\ 0, & \text{else.} \end{cases} \tag{4.11}$$

By definition, at $t' = \pm\tau/2$, $w(t') = 0$ and $\dot{w}(t') = 0$. Therefore, it is easily proven through integration by parts that:

$$w \circledast_t \dot{\vec{\rho}}_i = -\dot{w} \circledast_t \vec{\rho}_i \tag{4.12}$$

$$w \circledast_t \ddot{\vec{\rho}}_i = \ddot{w} \circledast_t \vec{\rho}_i \tag{4.13}$$

As a result, our loss function becomes:

$$L_{i,t,\alpha} = H\left((w \circledast_t \vec{f}_i^{\,\text{env}} + \sum_j w \circledast_t \vec{f}_{ij} + \gamma_i \dot{w} \circledast_t \vec{\rho}_i - \ddot{w} \circledast_t \vec{\rho}_i)_\alpha ; \delta \right) \tag{4.14}$$

Thus, by using the weak form, temporal derivatives of experimental particle positions are replaced by derivatives of the weight function, which is analytic.

As mentioned previously, the parameter δ controls the crossover from quadratic to linear loss in the Huber loss function. When $x < \delta$, $H(x;\delta) \propto x^2$ and when $x > \delta$, $H(x;\delta) \propto x$. Considering that a very large fitting error on a single data point might

arise from other sources of noise (for example, tracking error), this large error should be deemphasized (only matter linearly) in our loss function. The parameter δ is chosen to be:

$$\delta = 0.25\sqrt{\mathrm{TSS}_D} = 0.25\sqrt{\frac{1}{2N_pT_D}\sum_{i=0}^{(N_p-1)}\sum_{t\in\mathbb{T}_D}\sum_{\alpha}^{\{x,y\}}(\ddot{w}\circledast_t\vec{\rho}_i)_\alpha^2}, \tag{4.15}$$

where TSS is total sum of squares of the experimental acceleration in the loss function. D refers to either train or test data set. To quantify the quality of the model's fit, we define R^2 as:

$$R^2 = 1 - \frac{\mathrm{RSS}_{\mathrm{test}}}{\mathrm{TSS}_{\mathrm{test}}}, \tag{4.16}$$

where RSS is residual sum of squares:

$$\mathrm{RSS}_D = \frac{1}{2N_pT_D}\sum_{i=0}^{(N_p-1)}\sum_{t\in\mathbb{T}_D}\sum_{\alpha}^{\{x,y\}}(w\circledast_t\vec{f}_i^{\mathrm{env}}+\sum_j w\circledast_t\vec{f}_{ij}+\gamma_i\dot{w}\circledast_t\vec{\rho}_i-\ddot{w}\circledast_t\vec{\rho}_i)_\alpha^2. \tag{4.17}$$

We note that for $R^2 > 0.99$, the average percentage error should be $\sqrt{1-R^2} < 10\%$. Therefore, we set an arbitrary threshold, $\delta = 0.25$, which indicates that data with an error that is 2.5 times the average error should be considered an outlier in the Huber loss. Finally, the data is split into 10 temporal sections, and 10 models are trained by 10-fold cross-validation. Such splitting ensures that models inferred in one section work in the others, so that there are no significant drifts in the experiments. Note that because of the convolution (Eq. 4.10), for a data with time length T, t can only be defined on $\tau/2 \le t < T - \tau/2$. For the l-th model,

$$\mathbb{T}_{\mathrm{test}} = \left\{t|\tau/2 + \frac{l-1}{10}(T-\tau) \le t < \tau/2 + \frac{l}{10}(T-\tau)\right\} \tag{4.18}$$

and

$$\mathbb{T}_{\text{train}} = \{t|\tau/2 \leq t < T - \tau/2 \text{ and } t \notin \mathbb{T}_{\text{test}}\}\,. \tag{4.19}$$

The average (test) R^2 of the 10 models for the 10-fold validation is reported in Tbl. 4.1. The error bars shown in Figs 4.3,4.4 are calculated from the standard deviation of the 10 models' prediction. We note that this estimation of the error bars only includes the variance of the model, plus the variation caused by the temporal plasma environment fluctuation in the experiments, while the bias of the model is not included.

4.6.2 Data processing

To train the model, the data $x_{i,t}$, $y_{i,t}$, $z_{i,t}$, and $s_{i,t}$ needs to be organized into a form that can be efficiently iterated over to save computational time. Note that s_i is a time-averaged identifier of particle i and is independent of t. However, for consistency in the input, we constructed the array of $s_{i,t} \equiv s_i$ at all times. We need three tensors that can be used to calculated the convolution of the data with w, $\dot{w}$, and $\ddot{w}$. Thus, each term in the loss function was associated with a separate tensor of data to compute the convolution. The data is first processed into three tensors X^0, X^1, and Y. Y is the target, which is a 3D tensor with shape of $N_p \times (T-\tau) \times 2$. $Y_{i,t,\alpha} = \ddot{w} \circledast_t \alpha_i$ where α is either x or y. Similarly, $X^1_{i,t,\alpha} = \dot{w} \circledast_t \alpha_i$. X^0 is a 5D tensor, with a shape of $N_p \times (T-\tau) \times (\tau-1) \times N_p \times 4$. To explain the meaning of $X^0_{i,t,t',k,\alpha}$, we first define an index function on $0 \leq i < N_p$, $0 \leq k < N_p$:

$$n(i,k) = \begin{cases} i, & \text{if } k = 0, \\ k-1, & \text{if } 0 < k \leq i, \\ k, & \text{if } i < k < N_p. \end{cases} \tag{4.20}$$

Then $X^0_{i,t,t',k,\alpha} = \alpha_{j,t+t'+1}$, where α can be x, y, z, or s, and $j = n(i,k)$. Here, note that when calculating $w \circledast_t f_{ij}$, only the input from time $t - \tau/2 + 1$ to $t + \tau/2 - 1$

is needed, with a total length of $\tau - 1$, because $w_{\pm\tau/2} = 0$. Finally, the first two dimensions of all three tensors are flattened, and the last two dimensions of X^0 are flattened, making X^0, X^1 and Y 3D, 2D, and 2D tensors, respectively.

4.6.3 Fitting of charge and mass for each particle from the model

As described in Sec. 4.3, when two particles have the same z coordinates, their interaction is expected to be reciprocal, since oscillations over z are quickly averaged out. In fact, when $s_i = s_j$, the model requires their interaction to be reciprocal. In this regime, even if $s_i \neq s_j$, f_{ij} coincides with f_{ji} by shifting by the ratio of particle masses. For extracting m_i and q_i, we used a screened Coulomb interaction f^C:

$$f^C(\rho; q_i, q_j, m_i, \lambda_i, \lambda_j) = \frac{q_i q_j}{4\pi\epsilon_0 m_i \rho}\left(\frac{1}{\rho} + \frac{1}{\sqrt{\lambda_i\lambda_j}}\right)\exp\left(-\rho/\sqrt{\lambda_i\lambda_j}\right). \tag{4.21}$$

In order to find the mass and charge of all particles at a specific z position, we performed a global least-squares fit of every pair of particle interactions. For example, for a given z position, let $\bar{f}_{ij}(\rho)$ represents the model's prediction of particle j's reduced force on i at vertical position $z_i = z_j = z$ and horizontal separation ρ:

$$\bar{f}_{ij}(\rho) = \frac{g_{\text{int}}(\rho, z, z, s_i, s_j)}{\rho}. \tag{4.22}$$

In the fitting procedure, we aim at finding the optimal values of $\{q_i, q_j, m_i, \lambda_i, \lambda_j\}$ that minimize the following loss function:

$$L^C = \sum_{i=0}^{N_p}\sum_{j=0, j\neq i}^{N_p}\sum_{\rho}^{[a,b,c]}\left(\bar{f}_{ij}(\rho) - f^C(\rho; q_i, q_j, m_i, \lambda_i, \lambda_j)\right)^2. \tag{4.23}$$

Here $[a, b, c]$ defines which particle interactions to include in the sum. The minimum separation is $\rho = a$, the maximum separation is $\rho = b$, and particles within a small range c are included at each separation. For Fig. 4.3, we chose $a = 0.3$ mm, $b = 1.2$ mm, and $c = 0.01$ mm. We note that, although theory suggests the decay length λ does not depend on particle size, our model predicts otherwise. An example showing how the reduced interaction force depends on the size of particles is shown in Fig. 4.4C. Although the fitting function (Eq. 4.21) assigns an individual λ_i to each particle, this is not based on a physical theory, and is solely done to reduce the number of fitting parameters while still allowing flexibility in fitting λ for each particle interaction. Finally, we note that the charge and the mass are coupled in the fitting procedure since they appear as a ratio. For example, if we decrease all particles' mass by a factor of 4, and decrease all particles' charges by a factor of 2, the fitting quality wouldn't change. Thus, we added a constraint in the fitting that the average mass of the particles in the shaded area in Fig. 4.4 should be 1.65 ng, the average mass reported by the manufacturer. The above procedure was implemented for each of the 10 trained models, and the average q_i and m_i over all 10 models plus their standard deviation is reported in Fig. 4.4.

4.6.4 Dusty plasma simulations

In order to test the accuracy of the ML methods, and the inference of the mass and charge of particles, we simulated our dusty plasma system using a custom molecular dynamics code. The simulations are similar to those used in previous studies [79, 80, 82]. The simulations consisted of 15 spherical particles whose diameters were chosen from a Gaussian distribution with a mean of $d_0 = 10$ μm and a standard deviation of 1 μm. In the horizontal, xy-plane, the particles were confined by a harmonic potential with a small degree of asymmetry to match the experiments. They also experienced a vortical force to induce rotation of the system, leading to the following environmental

reduced force:

$$f_{i,x}^{\text{env}} = (1+\beta)\chi_h q_i x_i/m_i + \Omega^2 y_i - \gamma\dot{x}_i, \tag{4.24}$$

$$f_{i,y}^{\text{env}} = (1-\beta)\chi_h q_i y_i/m_i - \Omega^2 x_i - \gamma\dot{y}_i. \tag{4.25}$$

The degree of asymmetry of the potential was determined by the dimensionless number β, χ_h is the electric field gradient, q_i and m_i are the charge and mass of particle i, Ω is the strength of the background vorticity from ion drag, and x_i and y_i are the horizontal coordinates of particle i. Dotted variables indicate differentiation with respect to time and the Epstein drag force is determined by γ. The mass of each particle was computed as $m_i = \rho_p \pi d_i^3/6$, where $\rho_p = 1{,}510$ kg·m^{-3}, and d_i is the diameter of particle i.

In the vertical direction, the particles experienced a force due to a linearly-varying electric field, and gravity. The reduced force was determined by the following equation:

$$f_{i,z}^{\text{env}} = \min(E_0 + \chi_z z_i, 0) q_i/m_i - g - \gamma\dot{z}_i + \eta w(t). \tag{4.26}$$

Here E_0 is a constant vertical electric field, χ_z is the electric field gradient, z_i is the vertical position of the particle, and $g = 9.81$ m·s^{-2} is the acceleration due to gravity. The **min** function guarantees that the electric force will never change sign, and thus the edge of the plasma sheath occurs at $z_{\text{edge}} = -E_0/\chi_z$, a small distance above $z = 0$. The last term provides a small amount of stochastic noise in the z direction. This noise drives oscillations in z since the particles behave as stochastic harmonic oscillators with a well-defined resonance frequency. The function $w(t)$ represents a Wiener process with zero mean and unit standard deviation, and η is the strength of the noise. Since we are not inferring forces in z, this does not affect the inference procedure, and is based on previous experiments in our lab illustrating z oscillations

originating from Brownian motion [82] and spontaneous oscillations due to delayed charging at low pressures [47]. We also allow the charge on the particle to vary linearly within the sheath, increasing in magnitude as z_i decreases. This was done by treating each particle as a spherical capacitor, and parameterizing the charge in the following way:

$$q_i = \min(2\pi\epsilon_0 d_i V(1 - z_i/l_q), -8 \times 10^{-16}), \tag{4.27}$$

where the units of charge are in Coulombs. This guarantees that the magnitude of the (negative) charge on the particle will never be smaller than 5,000e, and the magnitude of the charge increases deeper into the sheath (smaller z_i). Here l_q is a length scale that determines the strength of charge variation in the sheath. The voltage V is a constant that determines the charge on a particle at $z = 0$.

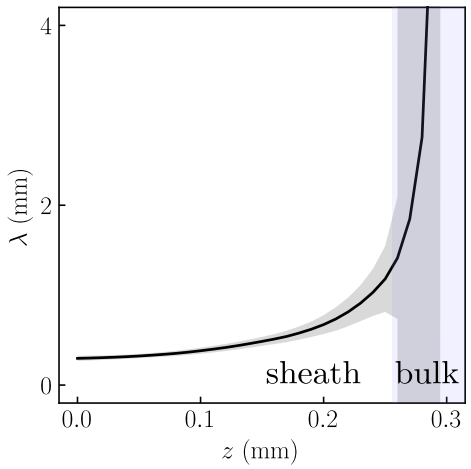

Figure 4.6: The fitted Debye length λ versus z for the 20 interactions of particles 1 and 2. The gray-shaded region indicates uncertainty. Note that our model's accuracy can only infer interaction when $\rho < 1.2$ mm, and the parameter λ is introduced in the term of $\exp(-\lambda/\rho)$ in Eq. 4.3. Thus when $\lambda > 1.2$ mm, the fitting cannot give accurate predictions of λ. The purple shaded region indicates bulk plasma, in which λ is predicted to be larger than 1.2 mm.

The parameters described here, such as electric field, are difficult to relate to experimental measurements. Thus, we fixed these parameters by relating them to

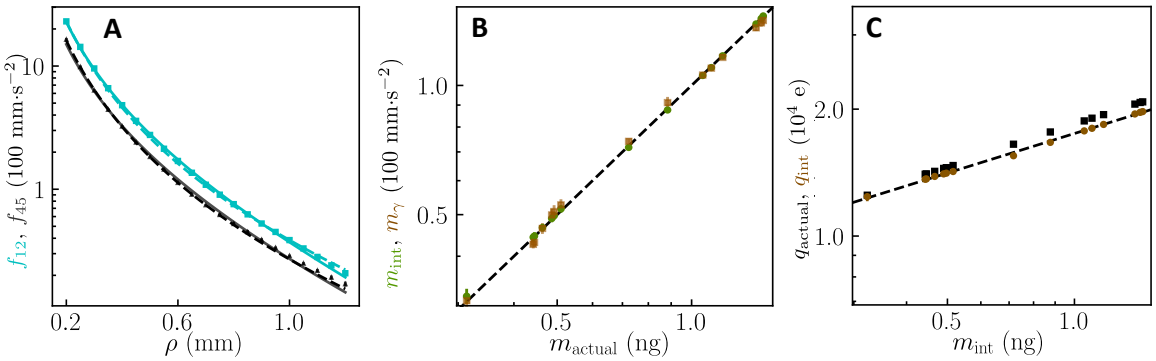

Figure 4.7: Results from the inference of mass and charge in dusty plasma simulations. The parameter values used for this simulation were $N = 15$, $d_0 = 10.0$ μm, $\lambda = 0.8$ mm, $\Omega = 4.25$ Hz, $V =$ -5 V, $\omega_h = 21.2$ Hz, $\omega_v = 157$ Hz, $\beta = 0.1$, $l_q = 1$ mm, $\eta = 5$ m/s^2, $\tilde{q} = 0.5$, and $b = 0.2$. (**A**) The interaction between two small particles indexed 1 and 2 (blue squares, the actual masses used in the simulation $m_1 = 0.44$ ng and $m_2 = 0.46$ ng), and two big particles indexed 4 and 5 (gray triangles, actual masses $m_4 = 1.43$ ng and $m_5 = 1.45$ ng). The solid lines with corresponding colors are fits to Eq. 4.3 with parameters $A = 97$ mm^3·s^{-2}, $\lambda = 0.48$ mm (f_{12}), and $A = 64$ mm^3·s^{-2}, $\lambda = 0.52$ mm (f_{45}). The dashed lines are the actual interaction reduced force used in the simulation. (**B**) The mass of all particles inferred from the drag coefficient (m_γ, green circles) and the mass inferred from the particle interactions (m_{int}, brown squares), versus their actual mass used in the simulation. The dashed line represents $m_{\text{int}} = m_\gamma = m_{\text{actual}}$. (**C**) Particle charges inferred from their interactions (q_{int}, brown circles), and their actual charges used in the simulation (q_{actual}, black squares), versus m_{int}. The dashed line is the optimal power-law fit to the inferred data with power $p = 0.31$.

the typical frequencies of small oscillations of the particles around their equilibrium positions. Experimentally, these can be measured from the 3D tracking data [81], and are given by ω_h in the horizontal direction, and ω_z in the vertical direction. Linearizing the force around $z = 0$, so that $f_z^{\text{env}} = 0$, $\omega_h^2 = -df_x^{\text{env}}/dx$, and $\omega_z^2 = -df_z^{\text{env}}/dz$, we arrive at the following relationships:

$$\chi_h = -\frac{\rho_p d_0^2 \omega_h^2}{12 V \epsilon_0}, \tag{4.28}$$

$$E_0 = \frac{\rho_p d_0^2 g}{12 V \epsilon_0}, \tag{4.29}$$

$$\chi_z = \frac{\rho_p d_0^2 (g - l_q \omega_v^2)}{12 l_q V \epsilon_0}. \tag{4.30}$$

This way a particle with diameter d_0 would have its equilibrium position at $z = 0$, and frequencies of small oscillations exactly equal to ω_h and ω_z. However, since particle sizes are drawn from a Gaussian distribution centered at d_0, the frequencies vary as well.

In addition to the environmental forces, the particles experienced a pairwise, non-reciprocal repulsive force. This force stems from basic Coulomb repulsion, but also from the wake of ions streaming past each particle. As done in Ref. [133], we parameterized this ion wake by an effective positive cloud of charge with magnitude $\tilde{q} q_i$ at a distance h beneath each particle. The force between particles was derived from the following potential:

$$\phi(\vec{r}) = \frac{q_i q_j}{4\pi\epsilon_0 \lambda_D} \left[\frac{e^{-r/\lambda_D}}{r/\lambda_D} - \tilde{q} \frac{e^{-r_w/\lambda_D}}{r_w/\lambda_D} \left(1 + b \frac{e^{-r_w/\lambda_D}}{r_w/\lambda_D} \right)^{-1} \right]. \tag{4.31}$$

Here, $\phi(\vec{r})$ is the potential of the ith particle in the field of the jth particle and its wake, and $f_{ij} = -\vec{\nabla}_i \phi$. The position vector between the particles is $\vec{r}$, $r_w = |\vec{r} - h\hat{z}|$ is the distance from particle i to the wake of particle j, $\hat{z}$ is the unit vector in the z direction, and λ_D is the Debye screening length in the plasma. Note that we

specifically denote λ_D, to differ from the general screening length λ used in the fitting (Eq. 4.3). Finally, b is dimensionless cutoff used to truncate the divergence of the wake interaction since the wake is not a point charge, but more of a cloud. With these environmental and interaction forces, the Newton's 2$^{\text{nd}}$ law was integrated forward in time using the 2$^{\text{nd}}$-order velocity Verlet method.

Without energy input, Epstein drag would drain the energy from the system and the particles would assume equilibrium positions. However, there are three mechanisms that drive kinetic and potential energy into the particles' motion. The first is the vortical force from ion drag, which is non-conservative. The second is the small amount of stochastic noise in the z-direction. The third is the non-reciprocal interaction force (also non-conservative) [69]. The resulting motion of the particles looks strikingly similar to the experiments , and can be easily analyzed by our ML model.

Prior to training the model, Gaussian-distributed measurement error with standard deviation 0.005 mm was added to each particle position to simulate experimental particle tracking error. In our simulation, we used $\lambda_D = 0.8$ mm (Eq. 4.31) for all particles. Figure 4.7A shows that at the same z-position, there is only a weak dependence of the fitted effective screening length (λ in Eq. 4.21) on different particle sizes since λ only varies from 0.48 - 0.52 mm for different particle pairs. This indicates that the particle-dependent effective screening length λ in experiments is real (Fig. 4.4A), rather than an artifact of the ML model. Moreover, the predicted interaction agrees with the exact interaction with less than 10% error (Fig. 4.7A). Even though the fit is very good, the presence of a virtual ion wake can systematically reduce the fitted values of the screening length ($\lambda = 0.52$ mm from the fit, and $\lambda_D = 0.80$ mm in Eq. 4.31). Figure 4.7B shows the inferred masses from the damping term, assuming Epstein drag (Eq. 4.2), and the mass inferred from the fitting procedure (Eq. 4.21 and following equations), versus the actual masses of particles used in the simulation. The agreement is remarkable and demonstrates that our model can accurately

infer each term in the equation of motion. Figure 4.7C shows the inferred charge on each particle versus the inferred mass. The fitted slope of $p = 0.31$ is close to the expected value from the simulation, $p = 1/3$, and reflects the fact that particles at the same vertical position will have the same floating potential, independent of their mass (Eq. 4.27). However, fitting to Eq. 4.3 results in a deviation of the prefactor $A = 89$ mm^3·s^{-2} from the actual $q_1 q_2 / 4\pi\epsilon_0 m_1 = 103$ mm^3·s^{-2}. This deviation of A can cause the inferred q to be systematically lower than the actual q by 5-10%.

Taken together, Fig. 4.7 suggests that the inference of interaction forces in simulated data is excellent, ion wake-mediated interactions can significantly reduce the effective screening length, and the inference of particle charge is very good (5-10% error).

Chapter 5

Conclusion and future directions

Before my research, the study of many-body behaviors in dusty plasma urgently needed information on the 3D motion of particles. In my research, I first constructed a tomography setup to track multiple particles' individual 3D trajectories. In the setup, the illuminating horizontal laser sheet oscillates up and down at a frequency of up to 200 Hz, which is about 100 times faster than the leading tomographic tracking of particles in dusty plasma. This tracking provides high-resolution information about the individual 3D trajectories of particles, enabling further inference of the physics governing their motion. Then, I developed machine learning (ML) algorithms to analyze these 3D trajectories. The first model analyzes the noise-driven motion of one and two particles around their equilibrium positions. The small amplitude of the motion offers the advantage of linearizing the forces on the particles, but it also presents the disadvantage that other small-amplitude artifacts (potentially non-Gaussian noise, environmental drift, etc.) may be significant. ML models, trained on simulations considering these artifacts, predicted the forces and their spatial differentials around particles' equilibrium positions. A mathematical formula is required to interpret particles' charge and Debye length from the models' predictions, which have increased accuracy by 50% over conventional methods like the Fourier spectrum.

The second model analyzes the large-amplitude motion of 10-20 particles. In this scenario, the linearization of the force is not valid anymore, and neural networks (NNs) are used as universal approximators for the interaction and environmental forces. Consequently, this model predicts the interaction and environmental forces for any particles at arbitrary positions, without a pre-assumed mathematical formula. Physical parameters such as particle charge and Debye length can be extracted by fitting the prediction to widely accepted formulas, and these predicted properties differ from conventional theories.

My research demonstrates the process of the ML-enabled discovery of new physics which deviates from conventional theories. The pursuit of new physics with machine learning inherently lacks a ground truth against which discoveries can be validated, as the phenomena under study are, by definition, new. This absence of a benchmark poses a unique challenge, particularly when the discovery process is mediated by the ostensibly opaque mechanisms of NNs. In such scenarios, creativity and critical thinking become paramount not only to drive innovation but also to validate these innovations in a meaningful way. One robust method to substantiate new findings involves making predictions about the same phenomenon in multiple, independent ways and observing consistency between these predictions. This approach underlines the importance of diverse validation strategies, as exemplified by the methodologies I have implemented in my research.

In overcoming the challenges of predicting physics in real experiments, especially when the phenomena are previously unexplored, I have employed a strategy that emphasizes validation through diverse methodologies. This approach is crucial when using neural networks, where the discovery process might not be transparent. For the one-particle model, the predicted 'spring constant' is validated through an independent perturbation experiment, demonstrating the model's capability to replicate physical behaviors through different experimental setups. In the many-particle model,

I have applied two distinct methods to consistently infer each particle's mass, thereby providing a robust check against the potential errors of a single method. Furthermore, the model consistently infers $E_z(s_i)$ at the particles' equilibrium positions and $E'_z(s_i)$, which connects the predicted $E_z(s_i)$. These consistent predictions across different methodologies help confirm the validity of the models.

With the inherent shortcomings of neural networks—their 'black box' nature and the reliance on empirical rather than strictly derived physical equations—effectively addressed by our robust validation methods, we harness their strengths as accurate universal approximators. Unlike methods that rely on a predefined library of functions, such as SINDy, neural networks can approximate arbitrary functions, leading to exceptionally high validation scores, with R^2 values reaching as high as 0.99. Our accurate model discovered new physics: a particle-dependent Debye length, and a deviation from the spherical capacitor theory. While not negating established theories, the superior accuracy of our neural network model over traditional theory's approximations (as discussed in Chap. 1.2.1) enables the discovery of these new physics.

Within the context of dusty plasma, many open questions await answers through my algorithm. For one example, in Sec. 1.2.2, the self-driven motion is explained, which relates to the delayed charge of the particle. In reference [76], the effective damping γ_{eff} of motion in the z direction is modeled as:

$$\gamma_{\text{eff}} = \gamma - \frac{q'_i(s_i)E_z(s_i)}{m_i\tau_{ch}} \tag{5.1}$$

Here, γ is the Epstein damping coefficient, and q'_i, E_z, and m_i can all be inferred from the model, and τ_{ch} is the charging time of a particle. A negative γ_{eff} indicates spontaneous oscillation.

In my Ph.D. work, we quantified q_i and E_z for any arbitrary particle i and any height z that this particle explores, as well as measured m_i and γ_i in-situ. However,

the characteristic charging time, τ_{ch}, remains unavailable from our current experiments, though numerical calculations estimate it to be the in the order of 1 ms [76].

The dynamics of charging and discharging particles after turning the plasma on and off is extensively studied [161–163]. Specifically, the discharging of a cloud of particles triggers lightning [164], where the air is ignited into a plasma. The measurement of the charging and discharging of particles in a plasma is usually conducted by applying an external electric field, which may alter the environment [165]. Measuring the charging and discharging *in situ* thus becomes very important. One direction of future experiment is to pulse the plasma or periodically turn the plasma on and off. The phase of this period, $\phi(t)$, would be an additional input to our neural networks g_{int}, $\vec{g}_{\text{env}}$, and g_γ. Repeating the same procedure as explained in Sec. 4.3, we have the potential to obtain the charge of particles as a function of ϕ, which tells us about the charging and discharging of the particle. With every parameters in eq. 5.1 measurable from a single experiment, our research would be the first to experimentally verify the mechanism of the dust particles' spontaneous oscillation.

Another open question is the field in a plasma sheath. As mentioned before, the interaction between dust particles inside a plasma is *environment-mediated*. A more detailed explanation is that the plasma environment can be described by a field, which involves n_e, n_r, T_e, T_r, etc. [31]. A particle's presence changes the local environment field, which then effectively exerts a force on another particle.

With a new high-speed camera installed, the camera recording frame rate can be up to 20000 Hz, allowing for a 500 Hz laser scanning rate and 40 frames per scan for better z resolution. Therefore, inferring force at z direction would be possible. The environmental force, if modeled as:

$$m_i \vec{f}_i^{\text{env}}(\vec{r}) = \vec{E}^{\text{env}}(\vec{r}) q_i(z) \tag{5.2}$$

tells the charge density field $\sigma = e(n_i - n_e)$ in the environment after $q_i(z)$ is extracted from particles' interactions:

$$\sigma = \nabla \cdot \vec{E}^{\text{env}}/\epsilon_0 \tag{5.3}$$

Since no change in magnet field is present in the experiment at the timescale of ms to s:

$$\frac{\partial \vec{B}}{\partial t} = 0 \tag{5.4}$$

The curl of the estimated electric field, $\nabla \times \vec{E}^{\text{env}}$, represents the residue caused by the presumption (eq. 5.2), which may be caused by the ion drag and second-order deviations from the pairwise model assumption.

Similarly, the local change of environmental σ caused by the presence of a particle i, is denoted $\sigma_i(\vec{r}; \vec{r}_i, q_i)$. σ_i is asymmetric in the z direction ($\sigma_i(x, y, z_i + \delta z; \vec{r}_i, q_i) \neq \sigma_i(x, y, z_i - \delta z; \vec{r}_i, q_i)$) due to ion flowing towards the electrode below, and is known as a particle's plasma wake that causes particles' interaction to be nonreciprocal (see fig.1.2). Researchers have experimentally discovered the non-reciprocal interaction and numerically simulated this effect [70–75], while our model has the potential to infer the plasma wake purely from experiment:

$$m_j \vec{f}_{ji} = \vec{E}_i(\vec{r}_j; \vec{r}_i, q_i) q_j(z_j) \tag{5.5}$$

where

$$\sigma_i(\vec{r}; \vec{r}_i, q_i) = \nabla_j \cdot \vec{E}_i(\vec{r}_j; \vec{r}_i, q_i) \tag{5.6}$$

Similar to $\vec{E}^{\text{env}}$, since no change in the $\vec{B}$ field exists, $\nabla_j \times \vec{E}_i(\vec{r}_j; \vec{r}_i, q_i)$ quantifies the uncertainty of this extraction of σ_i.

The aforementioned proposals of acquiring higher-resolution data and further investigating the model's predictions advance the idea of particles as probes in a plasma. This broadens the model's impact from a relatively small area of research (dusty

plasma) to a larger area of research, fundamental plasma physics, which is known as the 4th state of matter apart from solid, liquid, and gas. Particles as probes can accurately measure the properties of different plasma conditions, offering insights into more precise plasma research.

Finally, in the systems of thousands of particles, the charge density carried by particles is no longer negligible compared to the charge density carried by electrons and ions [48]. In this region, the linear combination of interactions ($\sum_j \vec{f}_{ij}$, pairwise assumptions) is no longer valid. In other words, the presence of a third particle k would affect two particles' charges (q_i, q_j), making f_{ij} dependent on positions of other particles than i, j. Graphical Neural Network (GNN) [166, 167] is one option to model this non-linear effect. GNN is a very newly-developed and popular tool to analyze high-dimensional data with dynamical connections, for example, stock market [168, 169] and pandemic propagation [170]. After I graduate, these new research ideas will be carried forward by new students in the lab, Zhicheng Shu and Wei-chih Li.

Outside dusty plasma, my approaches pave the way for applying ML to understand the physics in broader many-body systems, especially in biological systems, an emergent field of scientific study. Some 3D tracking algorithms for movies of cells have been developed [171, 172], while most experiments are conducted in 2D systems [173–175], demonstrating self-organized motion that breaks chiral symmetry. A pre-given formula of pairwise interaction in simulations can reproduce this chiral symmetry breaking [174, 176]. Akin to the 2D DP collective behaviors discovered before my arrival at the lab, these systems eagerly await the advent of advanced tracking algorithms capable of capturing three-dimensional nuances, coupled with machine learning architectures poised to unravel the mechanisms at play—mechanisms potentially unbound by preconceived formula.

Bibliography

[1] Indrajit Tah, Sean A Ridout, and Andrea J Liu. Fragility in glassy liquids: A structural approach based on machine learning. *The Journal of Chemical Physics*, 157(12):124501, 2022.

[2] Samuel S Schoenholz, Ekin D Cubuk, Daniel M Sussman, Efthimios Kaxiras, and Andrea J Liu. A structural approach to relaxation in glassy liquids. *Nature Physics*, 12(5):469–471, 2016.

[3] Jacob Page, Michael P Brenner, and Rich R Kerswell. Revealing the state space of turbulence using machine learning. *Physical Review Fluids*, 6(3):034402, 2021.

[4] Maziar Raissi, Alireza Yazdani, and George Em Karniadakis. Hidden fluid mechanics: Learning velocity and pressure fields from flow visualizations. *Science*, 367(6481):1026–1030, 2020.

[5] Jesús Pineda, Benjamin Midtvedt, Harshith Bachimanchi, Sergio Noé, Daniel Midtvedt, Giovanni Volpe, and Carlo Manzo. Geometric deep learning reveals the spatiotemporal features of microscopic motion. *Nature Machine Intelligence*, 5(1):71–82, 2023.

[6] John Toner and Yuhai Tu. Flocks, herds, and schools: A quantitative theory of flocking. *Physical review E*, 58(4):4828, 1998.

[7] Victor Bapst, Thomas Keck, A Grabska-Barwińska, Craig Donner, Ekin Dogus Cubuk, Samuel S Schoenholz, Annette Obika, Alexander WR Nelson, Trevor Back, Demis Hassabis, et al. Unveiling the predictive power of static structure in glassy systems. *Nature Physics*, 16(4):448–454, 2020.

[8] David B Brückner, Nicolas Arlt, Alexandra Fink, Pierre Ronceray, Joachim O Rädler, and Chase P Broedersz. Learning the dynamics of cell–cell interactions in confined cell migration. *Proceedings of the National Academy of Sciences*, 118(7):e2016602118, 2021.

[9] Jonathan Colen, Ming Han, Rui Zhang, Steven A Redford, Linnea M Lemma, Link Morgan, Paul V Ruijgrok, Raymond Adkins, Zev Bryant, Zvonimir Dogic, et al. Machine learning active-nematic hydrodynamics. *Proceedings of the National Academy of Sciences*, 118(10):e2016708118, 2021.

[10] Bryan C Daniels, William S Ryu, and Ilya Nemenman. Automated, predictive, and interpretable inference of caenorhabditis elegans escape dynamics. *Proceedings of the National Academy of Sciences*, 116(15):7226–7231, 2019.

[11] Chethan Pandarinath, Daniel J O'Shea, Jasmine Collins, Rafal Jozefowicz, Sergey D Stavisky, Jonathan C Kao, Eric M Trautmann, Matthew T Kaufman, Stephen I Ryu, Leigh R Hochberg, et al. Inferring single-trial neural population dynamics using sequential auto-encoders. *Nature methods*, 15(10): 805–815, 2018.

[12] Boyuan Chen, Kuang Huang, Sunand Raghupathi, Ishaan Chandratreya, Qiang Du, and Hod Lipson. Automated discovery of fundamental variables hidden in experimental data. *Nature Computational Science*, 2(7):433–442, 2022.

[13] Miguel Ruiz-Garcia, C Gutierrez, Lachlan C Alexander, Dirk GAL Aarts, Luca Ghiringhelli, and Chantal Valeriani. Discovering dynamic laws from

observations: the case of self-propelled, interacting colloids. *arXiv preprint arXiv:2203.14846*, 2022.

[14] Zhichao Han, David S Kammer, and Olga Fink. Learning physics-consistent particle interactions. *PNAS nexus*, 1(5):pgac264, 2022.

[15] Bryan C Daniels and Ilya Nemenman. Automated adaptive inference of phenomenological dynamical models. *Nature communications*, 6(1):8133, 2015.

[16] Steven L Brunton, Joshua L Proctor, and J Nathan Kutz. Discovering governing equations from data by sparse identification of nonlinear dynamical systems. *Proceedings of the national academy of sciences*, 113(15):3932–3937, 2016.

[17] Steven L Brunton, Joshua L Proctor, and J Nathan Kutz. Sparse identification of nonlinear dynamics with control (sindyc). *IFAC-PapersOnLine*, 49(18):710–715, 2016.

[18] Linan Zhang and Hayden Schaeffer. On the convergence of the sindy algorithm. *Multiscale Modeling & Simulation*, 17(3):948–972, 2019.

[19] Urban Fasel, Eurika Kaiser, J Nathan Kutz, Bingni W Brunton, and Steven L Brunton. Sindy with control: A tutorial. In *2021 60th IEEE Conference on Decision and Control (CDC)*, pages 16–21. IEEE, 2021.

[20] Urban Fasel, J Nathan Kutz, Bingni W Brunton, and Steven L Brunton. Ensemble-sindy: Robust sparse model discovery in the low-data, high-noise limit, with active learning and control. *Proceedings of the Royal Society A*, 478 (2260):20210904, 2022.

[21] Daniel A Messenger and David M Bortz. Weak sindy for partial differential equations. *Journal of Computational Physics*, 443:110525, 2021.

[22] Yu-Xin Jiang, Xiong Xiong, Shuo Zhang, Jia-Xiang Wang, Jia-Chun Li, and Lin Du. Modeling and prediction of the transmission dynamics of covid-19 based on the sindy-lm method. *Nonlinear Dynamics*, 105(3):2775–2794, 2021.

[23] Daniel E Shea, Steven L Brunton, and J Nathan Kutz. Sindy-bvp: Sparse identification of nonlinear dynamics for boundary value problems. *Physical Review Research*, 3(2):023255, 2021.

[24] Kathleen Champion, Bethany Lusch, J Nathan Kutz, and Steven L Brunton. Data-driven discovery of coordinates and governing equations. *Proceedings of the National Academy of Sciences*, 116(45):22445–22451, 2019.

[25] Anna Frishman and Pierre Ronceray. Learning force fields from stochastic trajectories. *Physical Review X*, 10(2):021009, 2020.

[26] Jaideep Pathak, Zhixin Lu, Brian R Hunt, Michelle Girvan, and Edward Ott. Using machine learning to replicate chaotic attractors and calculate lyapunov exponents from data. *Chaos: An Interdisciplinary Journal of Nonlinear Science*, 27(12), 2017.

[27] Nurnajmin Qasrina Ann, Dwi Pebrianti, Mohamad Fadhil Abas, and Luhur Bayuaji. Parameter estimation of lorenz attractor: A combined deep neural network and k-means clustering approach. In *Recent Trends in Mechatronics Towards Industry 4.0: Selected Articles from iM3F 2020, Malaysia*, pages 321–331. Springer, 2022.

[28] Kai Shun Lam. A saddle point finding method for lorenz attractor through business machine learning algorithm. *Available at SSRN 3837055*, 2021.

[29] Emmanuel Vincent, Shinji Watanabe, Aditya Arie Nugraha, Jon Barker, and Ricard Marxer. An analysis of environment, microphone and data simulation

mismatches in robust speech recognition. *Computer Speech & Language*, 46: 535–557, 2017.

[30] Juan Wang, Guan Gui, and Hikmet Sari. Generalized automatic modulation recognition method based on distributed learning in the presence of data mismatch problem. *Physical Communication*, 48:101428, 2021.

[31] André Melzer et al. *Physics of dusty plasmas*, volume 962. Springer, 2019.

[32] Rainer Hippler, Holger Kersten, Martin Schmidt, and Karl H Schoenbach. Low temperature plasmas. *Eds R Hippler et al, Berlin: Wiley*, 787, 2008.

[33] Manis Chaudhuri, Alexei V Ivlev, Sergey A Khrapak, Hubertus M Thomas, and Gregor E Morfill. Complex plasma—the plasma state of soft matter. *Soft Matter*, 7(4):1287–1298, 2011.

[34] Robert Merlino. Dusty plasmas: From saturn's rings to semiconductor processing devices. *Advances in Physics: X*, 6(1):1873859, 2021.

[35] CK Goertz. Dusty plasmas in the solar system. *Reviews of Geophysics*, 27(2): 271–292, 1989.

[36] J-E Wahlund, M André, AIE Eriksson, M Lundberg, MW Morooka, M Shafiq, TF Averkamp, DA Gurnett, GB Hospodarsky, WS Kurth, et al. Detection of dusty plasma near the e-ring of saturn. *Planetary and Space Science*, 57(14-15): 1795–1806, 2009.

[37] Padma K Shukla. *Dust Plasma Interaction in Space*. Nova Publishers, 2002.

[38] Uwe Kortshagen. Nonthermal plasma synthesis of semiconductor nanocrystals. *Journal of Physics D: Applied Physics*, 42(11):113001, 2009.

[39] Robert L Merlino and John A Goree. Dusty plasmas in the laboratory, industry, and space. *Physics Today*, 57(7):32–38, 2004.

[40] Job Beckers, Tijn van de Ven, Ruud van der Horst, Dmitry Astakhov, and Vadim Banine. Euv-induced plasma: A peculiar phenomenon of a modern lithographic technology. *Applied Sciences*, 9(14):2827, 2019.

[41] J Winter. Dust: A new challenge in nuclear fusion research? *Physics of Plasmas*, 7(10):3862–3866, 2000.

[42] VN Tsytovich, GE Morfill, VE Fortov, NG Gusein-Zade, BA Klumov, and SV Vladimirov. From plasma crystals and helical structures towards inorganic living matter. *New Journal of Physics*, 9(8):263, 2007.

[43] David Bohm and Eugene P Gross. Effects of plasma boundaries in plasma oscillations. *Physical Review*, 79(6):992, 1950.

[44] André Melzer and John Goree. Fundamentals of dusty plasmas. In R. Hippler, H. Kersten, M. Schmidt, and K. H. Schoenbach, editors, *Low temperature plasmas fundamentals, technologies, and techniques*, volume 1, pages 157–206. Wiley-VCH, 2 edition, 2008.

[45] JE Allen. Probe theory-the orbital motion approach. *Physica Scripta*, 45(5): 497, 1992.

[46] S Vidhya Lakshmi, R Bharuthram, and PK Shukla. Debye shielding in a dusty plasma. *Astrophysics and space science*, 209:213–219, 1993.

[47] Joshua Méndez Harper, Guram Gogia, Brady Wu, Zachary Laseter, and Justin C Burton. Origin of large-amplitude oscillations of dust particles in a plasma sheath. *Physical Review Research*, 2(3):033500, 2020.

[48] Andre Melzer, H Krüger, D Maier, and S Schütt. Physics of magnetized dusty plasmas. *Reviews of Modern Plasma Physics*, 5(1):11, 2021.

[49] Angela Douglass, Victor Land, Lorin Matthews, and Truell Hyde. Dust particle charge in plasma with ion flow and electron depletion near plasma boundaries. *Physics of Plasmas*, 18(8):083706, 2011.

[50] Jan Carstensen, Franko Greiner, and Alexander Piel. Determination of dust grain charge and screening lengths in the plasma sheath by means of a controlled cluster rotation. *Physics of Plasmas*, 17(8):083703, 2010.

[51] J Beckers, T Ockenga, M Wolter, WW Stoffels, J Van Dijk, H Kersten, and GMW Kroesen. Microparticles in a collisional rf plasma sheath under hypergravity conditions as probes for the electric field strength and the particle charge. *Physical review letters*, 106(11):115002, 2011.

[52] Angela Douglass, Victor Land, Ke Qiao, Lorin Matthews, and Truell Hyde. Determination of the levitation limits of dust particles within the sheath in complex plasma experiments. *Physics of Plasmas*, 19(1):013707, 2012.

[53] Noah Hershkowitz. Sheaths: More complicated than you think. *Physics of plasmas*, 12(5):055502, 2005.

[54] Federico Galli and Uwe R Kortshagen. Charging, coagulation, and heating model of nanoparticles in a low-pressure plasma accounting for ion–neutral collisions. *IEEE Transactions on Plasma Science*, 38(4):803–809, 2009.

[55] André Melzer, Thomas Trottenberg, and Alexander Piel. Experimental determination of the charge on dust particles forming coulomb lattices. *Physics Letters A*, 191(3-4):301–308, 1994.

[56] VE Fortov, AP Nefedov, VI Molotkov, MY Poustylnik, and VM Torchinsky. Dependence of the dust-particle charge on its size in a glow-discharge plasma. *Physical review letters*, 87(20):205002, 2001.

[57] Zhuanhao Zhang, Ke Qiao, Jie Kong, Lorin Matthews, and Truell Hyde. Simple method to measure the interaction potential of dielectric grains in a dusty plasma. *Physical Review E*, 82(3):036401, 2010.

[58] SK Sharma, Ranjan Kalita, Y Nakamura, and H Bailung. Dust charge measurement in a strongly coupled dusty plasma produced by an rf discharge. *Plasma Sources Science and Technology*, 21(4):045002, 2012.

[59] Tim Jacobus Adrianus Staps, Tim Jacobus Maria Donders, Bart Platier, and Job Beckers. In-situ measurement of dust charge density in nanodusty plasma. *Journal of Physics D: Applied Physics*, 55(8):08LT01, 2021.

[60] Chun-Shang Wong, J Goree, Zach Haralson, and Bin Liu. Strongly coupled plasmas obey the fluctuation theorem for entropy production. *Nature Physics*, 14(1):21, 2018.

[61] Zhiyue Ding, Ke Qiao, Nicholas Ernst, Jie Kong, Mudi Chen, Lorin S Matthews, and Truell W Hyde. Nonlinear mode coupling and internal resonance observed in a dusty plasma. *New Journal of Physics*, 21(10):103051, 2019.

[62] Carl M Bender and Steven A Orszag. *Advanced mathematical methods for scientists and engineers I: Asymptotic methods and perturbation theory*. Springer Science & Business Media, 2013.

[63] Charles Kittel et al. *Introduction to solid state physics*, volume 8. Wiley New York, 1976.

[64] Neil W Ashcroft. Nd mermin solid state physics. *Saunders College, Philadelphia*, 120, 1976.

[65] SHXWS Nunomura, J Goree, S Hu, X Wang, and Amitava Bhattacharjee.

Dispersion relations of longitudinal and transverse waves in two-dimensional screened coulomb crystals. *Physical Review E*, 65(6):066402, 2002.

[66] SK Zhdanov, AV Ivlev, and GE Morfill. Mode-coupling instability of two-dimensional plasma crystals. *Physics of Plasmas*, 16(8):083706, 2009.

[67] L Couëdel, V Nosenko, SK Zhdanov, AV Ivlev, HM Thomas, and GE Morfill. First direct measurement of optical phonons in 2d plasma crystals. *Physical review letters*, 103(21):215001, 2009.

[68] L Couëdel, V Nosenko, AV Ivlev, SK Zhdanov, HM Thomas, and GE Morfill. Direct observation of mode-coupling instability in two-dimensional plasma crystals. *Physical review letters*, 104(19):195001, 2010.

[69] AV Ivlev, J Bartnick, M Heinen, C-R Du, V Nosenko, and H Löwen. Statistical mechanics where newton's third law is broken. *Physical Review X*, 5(1):011035, 2015.

[70] Ke Qiao, Jie Kong, Lorin S Matthews, and Truell W Hyde. Mode couplings and resonance instabilities in finite dust chains. *Physical Review E*, 91(5):053101, 2015.

[71] PJ Adamson, CM Carmichael, GD Griffin, J Martinez Ortiz, LS Matthews, and TW Hyde. Torsion density related to electrode and crystal size. In *2022 IEEE International Conference on Plasma Science (ICOPS)*, pages 1–2. IEEE, 2022.

[72] A Mendoza, KS Ashrafi, LS Matthews, and TW Hyde. Determining forces on dust grains in a plasma with a position-dependent number density. In *2022 IEEE International Conference on Plasma Science (ICOPS)*, pages 1–1. IEEE, 2022.

[73] AV Zampetaki, H Huang, C-R Du, H Löwen, and AV Ivlev. Buckling of two-dimensional plasma crystals with nonreciprocal interactions. *Physical Review E*, 102(4):043204, 2020.

[74] MG Hariprasad, P Bandyopadhyay, VS Nikolaev, DA Kolotinskii, S Arumugam, G Arora, S Singh, A Sen, and AV Timofeev. Self-sustained non-equilibrium co-existence of fluid and solid states in a strongly coupled complex plasma system. *Scientific Reports*, 12(1):13882, 2022.

[75] EA Lisin, OF Petrov, EA Sametov, OS Vaulina, KB Statsenko, MM Vasiliev, J Carmona-Reyes, and TW Hyde. Experimental study of the nonreciprocal effective interactions between microparticles in an anisotropic plasma. *Scientific Reports*, 10(1):13653, 2020.

[76] AV Ivlev, U Konopka, and G Morfill. Influence of charge variation on particle oscillations in the plasma sheath. *Physical Review E*, 62(2):2739, 2000.

[77] Tim Bockwoldt, Oliver Arp, Kristoffer Ole Menzel, and Alexander Piel. On the origin of dust vortices in complex plasmas under microgravity conditions. *Physics of Plasmas*, 21(10):103703, 2014.

[78] GE Norman and AV Timofeev. Kinetic temperature of dust particle motion in gas-discharge plasma. *Physical Review E*, 84(5):056401, 2011.

[79] Guram Gogia and Justin C Burton. Emergent bistability and switching in a nonequilibrium crystal. *Physical Review Letters*, 119(17):178004, 2017.

[80] G. Gogia, W. Yu, and J. C. Burton. Intermittent turbulence in a many-body system. *Phys. Rev. Research*, 2:023250, 2020. doi: 10.1103/PhysRevResearch.2.023250.

[81] Wentao Yu and Justin C Burton. 3d tracking of particles in a dusty plasma by laser sheet tomography. *Physics of Plasmas*, 30(6), 2023.

[82] Wentao Yu, Jonathan Cho, and Justin C Burton. Extracting forces from noisy dynamics in dusty plasmas. *Physical Review E*, 106(3):035303, 2022.

[83] Gerrit E Elsinga, Fulvio Scarano, Bernhard Wieneke, and Bas W van Oudheusden. Tomographic particle image velocimetry. *Experiments in fluids*, 41(6): 933–947, 2006.

[84] Markus Raffel, Christian E Willert, Jürgen Kompenhans, Fulvio Scarano, Christian J Kähler, and Steve T. Wereley. *Particle image velocimetry: a practical guide*, volume 2. Springer, 1998.

[85] Jeremiah D Williams. Application of tomographic particle image velocimetry to studies of transport in complex (dusty) plasma. *Physics of Plasmas*, 18(5): 050702, 2011.

[86] Yan Feng, J Goree, and Bin Liu. Solid superheating observed in two-dimensional strongly coupled dusty plasma. *Physical review letters*, 100(20):205007, 2008.

[87] Yan Feng, J Goree, Zach Haralson, Chun-Shang Wong, A Kananovich, and Wei Li. Particle position and velocity measurement in dusty plasmas using particle tracking velocimetry. *Journal of Plasma Physics*, 82(3), 2016.

[88] Yue Zeng, Zhuang Ma, and Yan Feng. Determination of best particle tracking velocimetry method for two-dimensional dusty plasmas. *Review of Scientific Instruments*, 93(3):033507, 2022.

[89] Bin Liu, John Goree, VE Fortov, AM Lipaev, VI Molotkov, OF Petrov, GE Morfill, HM Thomas, H Rothermel, and AV Ivlev. Transverse oscillations

in a single-layer dusty plasma under microgravity. *Physics of plasmas*, 16(8): 083703, 2009.

[90] Michael Himpel, Birger Buttenschoen, and Andre Melzer. Three-view stereoscopy in dusty plasmas under microgravity: A calibration and reconstruction approach. *Review of Scientific Instruments*, 82(5):053706, 2011.

[91] Michael Himpel, Tim Bockwoldt, Carsten Killer, Kristoffer Ole Menzel, Alexander Piel, and André Melzer. Stereoscopy of dust density waves under microgravity: Velocity distributions and phase-resolved single-particle analysis. *Physics of Plasmas*, 21(3):033703, 2014.

[92] Daniel Schanz, Sebastian Gesemann, and Andreas Schröder. Shake-the-box: Lagrangian particle tracking at high particle image densities. *Experiments in fluids*, 57(5):1–27, 2016.

[93] Andreas Alpers, Peter Gritzmann, Dmitry Moseev, and Mirko Salewski. 3d particle tracking velocimetry using dynamic discrete tomography. *Computer Physics Communications*, 187:130–136, 2015.

[94] Michael Himpel and André Melzer. Fast 3d particle reconstruction using a convolutional neural network: application to dusty plasmas. *Machine Learning: Science and Technology*, 2(4):045019, 2021.

[95] Zhehui Wang, Jiayi Xu, Yao E Kovach, Bradley T Wolfe, Edward Thomas Jr, Hanqi Guo, John E Foster, and Han-Wei Shen. Microparticle cloud imaging and tracking for data-driven plasma science. *Physics of Plasmas*, 27(3):033703, 2020.

[96] Michael Himpel, Carsten Killer, Birger Buttenschön, and André Melzer. Three-dimensional single particle tracking in dense dust clouds by stereoscopy of fluorescent particles. *Physics of Plasmas*, 19(12):123704, 2012.

[97] AP Nefedov, OF Petrov, and SA Khrapak. Potential of electrostatic interaction in a thermal dusty plasma. *Plasma Physics Reports*, 24(12):1037–1040, 1998.

[98] V Yu Karasev, ES Dzlieva, A Yu Ivanov, AI Éĭkhval'd, and MV Golubev. Optical scanning of dusty 3d-structures formed in a glow discharge. *Optics and Spectroscopy*, 106:808–812, 2009.

[99] M Zuzic, AV Ivlev, J Goree, GE Morfill, HM Thomas, H Rothermel, U Konopka, R Sütterlin, and DD Goldbeck. Three-dimensional strongly coupled plasma crystal under gravity conditions. *Physical review letters*, 85(19):4064, 2000.

[100] H Thomas, GE Morfill, and VN Tsytovich. Complex plasmas: Iii. experiments on strong coupling and long-range correlations. *Plasma Physics Reports*, 29: 895–954, 2003.

[101] C Dietz, R Bergert, B Steinmüller, M Kretschmer, S Mitic, and MH Thoma. fcc-bcc phase transition in plasma crystals using time-resolved measurements. *Physical Review E*, 97(4):043203, 2018.

[102] D Samsonov, A Elsaesser, A Edwards, HM Thomas, and GE Morfill. High speed laser tomography system. *Review of Scientific Instruments*, 79(3):035102, 2008.

[103] Wen Wang, Hao-Wei Hu, and I Lin. Surface-induced layering of quenched 3d dusty plasma liquids: micromotion and structural rearrangement. *Physical Review Letters*, 124(16):165001, 2020.

[104] Daniel B. Allan, Thomas Caswell, Nathan C. Keim, Casper M. van der Wel, and Ruben W. Verweij. soft-matter/trackpy: Trackpy v0.5.0, 2021. URL `https://doi.org/10.5281/zenodo.4682814`.

[105] Yuval Yifat, Nishant Sule, Yihan Lin, and Norbert F Scherer. Analysis and

correction of errors in nanoscale particle tracking using the single-pixel interior filling function (spiff) algorithm. *Scientific reports*, 7(1):1–10, 2017.

[106] S Nunomura, T Misawa, N Ohno, and S Takamura. Instability of dust particles in a coulomb crystal due to delayed charging. *Physical review letters*, 83(10): 1970, 1999.

[107] D Samsonov and J Goree. Instabilities in a dusty plasma with ion drag and ionization. *Physical Review E*, 59(1):1047, 1999.

[108] M. Choudhary, R. Bergert, S. Mitic, and M. H. Thomas. Three-dimensional dusty plasma in a strong magnetic field: Observation of rotating dust tori. *Phys. Plasmas*, 27:063701, 2020. doi: 10.1063/5.0004842.

[109] Federico S Gnesotto, Grzegorz Gradziuk, Pierre Ronceray, and Chase P Broedersz. Learning the non-equilibrium dynamics of brownian movies. *Nature communications*, 11(1):5378, 2020.

[110] Samuel H Rudy, Steven L Brunton, Joshua L Proctor, and J Nathan Kutz. Data-driven discovery of partial differential equations. *Science advances*, 3(4): e1602614, 2017.

[111] Zhe Ding, Jingfeng Yao, Ying Wang, Chengxun Yuan, Zhongxiang Zhou, Anatoly Kudryavtsev, Ruilin Gao, and Jieshu Jia. Machine learning combined with langmuir probe measurements for diagnosis of dusty plasma of a positive column. *Plasma Sc. Technol.*, 2021.

[112] Zhe Ding, Qiuyu Guan, Chengxun Yuan, Zhongxiang Zhou, and Zhenshen Qu. A method of electron density of positive column diagnosis—combining machine learning and langmuir probe. *AIP Advances*, 11(4):045028, 2021.

[113] Jonathan Chalaturnyk and Richard Marchand. A first assessment of a regression-based interpretation of langmuir probe measurements. *Frontiers in Physics*, 7:63, 2019.

[114] Ayaz Hussain Bukhari, Muhammad Sulaiman, Muhammad Asif Zahoor Raja, Saeed Islam, Muhammad Shoaib, and Poom Kumam. Design of a hybrid nar-rbfs neural network for nonlinear dusty plasma system. *Alexandria Engineering Journal*, 59(5):3325–3345, 2020.

[115] He Huang, Mierk Schwabe, and Cheng-Ran Du. Identification of the interface in a binary complex plasma using machine learning. *Journal of Imaging*, 5(3): 36, 2019.

[116] Zhehui Wang, Jiayi Xu, Yao E. Kovach, Bradley T. Wolfe, Edward Thomas Jr., Hanqi Guo, John E. Foster, and Han-Wei Shen. Microparticle cloud imaging and tracking for data-driven plasma science. *Phys. Plasmas*, 27:033703, 2020.

[117] Zhiyue Ding, Lorin S Matthews, and Truell W Hyde. A machine learning based bayesian optimization solution to non-linear responses in dusty plasmas. *Machine Learning: Science and Technology*, 2(3):035017, 2021.

[118] A. K. Mukhopadhyay and J. Goree. Two-particle distribution and correlation function for a 1d dusty plasma experiment. *Phys. Rev. Lett.*, 109(16):165003, 2012.

[119] Y. Feng, J. Goree, and B. Liu. Accurate particle position measurement from images. *Rev. Sci. Instrum.*, 78:053704, 2007.

[120] Stanislav Burov, Patrick Figliozzi, Binhua Lin, Stuart A Rice, Norbert F Scherer, and Aaron R Dinner. Single-pixel interior filling function approach for detecting and correcting errors in particle tracking. *P. Natl. Acad. Sci. USA*, 114(2):221–226, 2017.

[121] K.-B. Chai and P. M. Bellan. Vortex motion of dust particles due to non-conservative ion drag force in a plasma. *Phys. Plasmas*, 23:023701, 2016. doi: 10.1063/1.4941973.

[122] V. Nosenko, F. Luoni, A. Kaouk, M. Rubin-Zuzic, and H. Thomas. Active janus particles in a complex plasma. *Phys. Rev. Research*, 2:033226, 2020. doi: 10.1103/PhysRevResearch.2.033226.

[123] U. Konopka, D. Samsonov, A. V. Ivlev, J. Goree, V. Steinberg, and G. E. Morfill. Rigid and differential plasma crystal rotation induced by magnetic fields. *Phys. Rev. E*, 61:1890, 2000. doi: 10.1103/PhysRevE.61.1890.

[124] Paul S Epstein. On the resistance experienced by spheres in their motion through gases. *Physical Review*, 23(6):710, 1924.

[125] David B. Brückner, Pierre Ronceray, and Chase P. Broedersz. Inferring the dynamics of underdamped stochastic systems. *Phys. Rev. Lett.*, 125:058103, 2020. doi: 10.1103/PhysRevLett.125.058103.

[126] F. Pedregosa, G. Varoquaux, A. Gramfort, V. Michel, B. Thirion, O. Grisel, M. Blondel, P. Prettenhofer, R. Weiss, V. Dubourg, J. Vanderplas, A. Passos, D. Cournapeau, M. Brucher, M. Perrot, and E. Duchesnay. Scikit-learn: Machine learning in Python. *J. Mach. Learn. Res.*, 12:2825–2830, 2011.

[127] Jie Kong, Ke Qiao, Lorin S. Matthews, and Truell W. Hyde. Temperature measurement of a dust particle in a rf plasma gec reference cell. *J. Plasma Phy.*, 82(5):905820505, 2016. doi: 10.1017/S0022377816000842.

[128] M. Himpel and A. Melzer. Configurational temperature in dusty plasmas. *Phys. Rev. E*, page 063203, 2019.

[129] Ke Qiao, Zhiyue Ding, Jie Kong, Mudi Chen, Lorin S Matthews, and Truell W Hyde. Determination of interaction between a dust particle pair in complex plasmas. *arXiv preprint arXiv:1705.01982*, 2017.

[130] Jie Kong, Ke Qiao, Lorin S Matthews, and Truell W Hyde. Interaction force in a vertical dust chain inside a glass box. *Phys. Rev. E*, 90(1):013107, 2014.

[131] T. E. Sheridan, M. R. Katschke, and K. D. Wells. Measurement of electric field and gradient in the plasma sheath using clusters of floating microspheres. *Rev. Sci. Instrum.*, 78:023502, 2007. doi: 10.1063/1.2437114.

[132] Osamu Ishihara and Sergey V. Vladimirov. Wake potential of a dust grain in a plasma with ion flow. *Phys. Plasmas*, 4:69–74, 1997.

[133] Nikita P Kryuchkov, Lukiya A Mistryukova, Andrei V Sapelkin, and Stanislav O Yurchenko. Strange attractors induced by melting in systems with nonreciprocal effective interactions. *Phys. Rev. E*, 101(6):063205, 2020.

[134] V. S. Nikolaev and A. V. Timofeev 2016 J. Phys.: Conf. Ser. 774 012172. Screening length in dusty plasma crystals. *J. Phys.: Conf. Ser.*, 774:012172, 2016. doi: 10.1088/1742-6596/774/1/012172.

[135] Harold M Mott-Smith and Irving Langmuir. The theory of collectors in gaseous discharges. *Phys. Rev.*, 28(4):727, 1926.

[136] Xian-Zhu Tang and Gian Luca Delzanno. Orbital-motion-limited theory of dust charging and plasma response. *Phys. Plasmas*, 21:123708, 1994.

[137] Y. Saitou. A simple method of dust charge estimation using an externally applied oscillating electric field. *Phys. Plasmas*, 25:073701, 2018. doi: 10.1063/1.5037020.

[138] S. A. Khrapak and G. E. Morfill. An interpolation formula for the ion flux to a small particle in collisional plasmas. *Phys. Plasmas*, 15:114503, 2008. doi: 10.1063/1.3035913.

[139] Wentao Yu, Eslam Abdelaleem, Ilya Nemenman, and Justin C Burton. Learning force laws in many-body systems. *arXiv preprint arXiv:2310.05273*, 2023.

[140] Federico Battiston, Enrico Amico, Alain Barrat, Ginestra Bianconi, Guilherme Ferraz de Arruda, Benedetta Franceschiello, Iacopo Iacopini, Sonia Kéfi, Vito Latora, Yamir Moreno, et al. The physics of higher-order interactions in complex systems. *Nature Physics*, 17(10):1093–1098, 2021.

[141] Giuseppe Carleo, Ignacio Cirac, Kyle Cranmer, Laurent Daudet, Maria Schuld, Naftali Tishby, Leslie Vogt-Maranto, and Lenka Zdeborová. Machine learning and the physical sciences. *Reviews of Modern Physics*, 91(4):045002, 2019.

[142] George Em Karniadakis, Ioannis G Kevrekidis, Lu Lu, Paris Perdikaris, Sifan Wang, and Liu Yang. Physics-informed machine learning. *Nature Reviews Physics*, 3(6):422–440, 2021.

[143] Frank Cichos, Kristian Gustavsson, Bernhard Mehlig, and Giovanni Volpe. Machine learning for active matter. *Nature Machine Intelligence*, 2(2):94–103, 2020.

[144] Martin J Falk, Vahid Alizadehyazdi, Heinrich Jaeger, and Arvind Murugan. Learning to control active matter. *Physical Review Research*, 3(3):033291, 2021.

[145] Lorin Swint Matthews, Dustin L Sanford, Evdokiya G Kostadinova, Khandaker Sharmin Ashrafi, Evelyn Guay, and Truell W Hyde. Dust charging in dynamic ion wakes. *Physics of Plasmas*, 27(2), 2020.

[146] E Thomas, RL Merlino, and M Rosenberg. Magnetized dusty plasmas: the next frontier for complex plasma research. *Plasma Physics and Controlled Fusion*, 54(12):124034, 2012.

[147] Andre Melzer, Harald Krueger, Stefan Schuett, and Matthias Mulsow. Finite dust clusters under strong magnetic fields. *Physics of Plasmas*, 26(9):093702, 2019.

[148] VS Nikolaev and AV Timofeev. Nonhomogeneity of phase state in a dusty plasma monolayer with nonreciprocal particle interactions. *Physics of Plasmas*, 28(3):033704, 2021.

[149] Daniil Aleksandrovich Kolotinskii, Vladislav Sergeevich Nikolaev, and Aleksei Vladimirovich Timofeev. Effect of structural inhomogeneity and nonreciprocal effects in the interaction of macroparticles on the dynamic properties of a dusty plasma monolayer. *JETP Letters*, 113(8):510–517, 2021.

[150] OS Vaulina, II Lisina, and EA Lisin. Energy exchange in systems of particles with nonreciprocal interaction. *Journal of Experimental and Theoretical Physics*, 121:717–726, 2015.

[151] U Konopka, GE Morfill, and L Ratke. Measurement of the interaction potential of microspheres in the sheath of a rf discharge. *Physical review letters*, 84(5): 891, 2000.

[152] Franko Greiner, Andrè Melzer, Benjamin Tadsen, Sebastian Groth, Carsten Killer, Florian Kirchschlager, Frank Wieben, Iris Pilch, Harald Krüger, Dietmar Block, et al. Diagnostics and characterization of nanodust and nanodusty plasmas. *The European Physical Journal D*, 72:1–12, 2018.

[153] Martin Lampe, Glenn Joyce, Gurudas Ganguli, and Valeriy Gavrishchaka. In-

teractions between dust grains in a dusty plasma. *Physics of Plasmas*, 7(10): 3851–3861, 2000.

[154] Ranganathan Gopalakrishnan and Christopher J Hogan Jr. Coulomb-influenced collisions in aerosols and dusty plasmas. *Physical Review E*, 85(2):026410, 2012.

[155] AM Ignatov. Interaction of grains in dusty plasmas. *Le Journal de Physique IV*, 7(C4):C4–215, 1997.

[156] J Goree. Charging of particles in a plasma. *Plasma Sources Science and Technology*, 3(3):400, 1994.

[157] Daniel R Gurevich, Patrick AK Reinbold, and Roman O Grigoriev. Robust and optimal sparse regression for nonlinear pde models. *Chaos: An Interdisciplinary Journal of Nonlinear Science*, 29(10):103113, 2019.

[158] Sergey V Vladimirov and Mitsuhiro Nambu. Attraction of charged particulates in plasmas with finite flows. *Physical Review E*, 52(3):R2172, 1995.

[159] Marco Gatti and Uwe Kortshagen. Analytical model of particle charging in plasmas over a wide range of collisionality. *Physical Review E*, 78(4):046402, 2008.

[160] Martín Abadi, Ashish Agarwal, Paul Barham, Eugene Brevdo, Zhifeng Chen, Craig Citro, Greg S. Corrado, Andy Davis, Jeffrey Dean, Matthieu Devin, Sanjay Ghemawat, Ian Goodfellow, Andrew Harp, Geoffrey Irving, Michael Isard, Yangqing Jia, Rafal Jozefowicz, Lukasz Kaiser, Manjunath Kudlur, Josh Levenberg, Dandelion Mané, Rajat Monga, Sherry Moore, Derek Murray, Chris Olah, Mike Schuster, Jonathon Shlens, Benoit Steiner, Ilya Sutskever, Kunal Talwar, Paul Tucker, Vincent Vanhoucke, Vijay Vasudevan, Fernanda Viégas, Oriol Vinyals, Pete Warden, Martin Wattenberg, Martin Wicke, Yuan Yu, and

Xiaoqiang Zheng. TensorFlow: Large-scale machine learning on heterogeneous systems, 2015. URL `https://www.tensorflow.org/`. Software available from tensorflow.org.

[161] Lénaïc Couëdel, Abdelaziz Mezeghrane, Alexander A Samarian, Maxime Mikikian, Yves Tessier, Marjorie Cavarroc, and Laifa Boufendi. Complex plasma afterglow. *Contributions to Plasma Physics*, 49(4-5):235–259, 2009.

[162] IB Denysenko, Maxime Mikikian, and NA Azarenkov. Dust dynamics during the plasma afterglow. *Journal of Physics D: Applied Physics*, 55(9):095201, 2021.

[163] NG Adams, MJ Church, and D Smith. An experimental and theoretical investigation of the dynamics of a flowing afterglow plasma. *Journal of Physics D: Applied Physics*, 8(12):1409, 1975.

[164] Martin A Uman. *The lightning discharge*. Courier Corporation, 2012.

[165] Lénaïc Couëdel. Temporal dusty plasma afterglow: A review. *Frontiers in Physics*, 10:1015603, 2022.

[166] Zhiyuan Liu and Jie Zhou. *Introduction to graph neural networks*. Springer Nature, 2022.

[167] Wei Jin, Yao Ma, Xiaorui Liu, Xianfeng Tang, Suhang Wang, and Jiliang Tang. Graph structure learning for robust graph neural networks. In *Proceedings of the 26th ACM SIGKDD international conference on knowledge discovery & data mining*, pages 66–74, 2020.

[168] Wenjun Zhang, Zhensong Chen, Jianyu Miao, and Xueyong Liu. Research on graph neural network in stock market. *Procedia Computer Science*, 214:786–792, 2022.

[169] Kialan Pillay and Deshendran Moodley. Exploring graph neural networks for stock market prediction on the jse. In *Southern African Conference for Artificial Intelligence Research*, pages 95–110. Springer, 2021.

[170] Zewen Liu, Guancheng Wan, B Aditya Prakash, Max SY Lau, and Wei Jin. A review of graph neural networks in epidemic modeling. In *Proceedings of the 30th ACM SIGKDD Conference on Knowledge Discovery and Data Mining*, pages 6577–6587, 2024.

[171] Jiranuwat Sapudom, Johannes Waschke, Katja Franke, Mario Hlawitschka, and Tilo Pompe. Quantitative label-free single cell tracking in 3d biomimetic matrices. *Scientific reports*, 7(1):14135, 2017.

[172] Ko Sugawara, Çağrı Çevrim, and Michalis Averof. Tracking cell lineages in 3d by incremental deep learning. *Elife*, 11:e69380, 2022.

[173] Jeremie Palacci, Stefano Sacanna, Asher Preska Steinberg, David J Pine, and Paul M Chaikin. Living crystals of light-activated colloidal surfers. *Science*, 339(6122):936–940, 2013.

[174] Tzer Han Tan, Alexander Mietke, Junang Li, Yuchao Chen, Hugh Higinbotham, Peter J Foster, Shreyas Gokhale, Jörn Dunkel, and Nikta Fakhri. Odd dynamics of living chiral crystals. *Nature*, 607(7918):287–293, 2022.

[175] Alexander P Petroff, Xiao-Lun Wu, and Albert Libchaber. Fast-moving bacteria self-organize into active two-dimensional crystals of rotating cells. *Physical review letters*, 114(15):158102, 2015.

[176] Haoran Xu and Yilin Wu. Self-enhanced mobility enables vortex pattern formation in living matter. *Nature*, pages 1–6, 2024.